A SPECTROPHOTOMETRIC STUDY OF SEYFERT NUCLEI

Thesis by

Kurt S. Anderson

In Partial Fulfillment of the Requirements

For the Degree of

Doctor of Philosophy

California Institute of Technology

Pasadena, California

1969

(Submitted 8 October, 1968)

ACKNOWLEDGEMENTS

I am greatly indebted to the many persons who, through instruction, advice, discussion, and encouragement, contributed much to the eventual completion of this thesis. To a number of individuals, particular appreciation should be expressed.

Dr. Maarten Schmidt originally suggested the Seyfert galaxies as objects worthy of detailed investigation and provided an introduction to their peculiar properties. In addition to discussion, Dr. O. C. Wilson supplied much of the spectroscopic data upon which the preliminary investigations were based.

In the operation of the Mount Wilson spectrographs, the instruction provided by Dr. G. Munch and Dr. R. P. Kraft proved invaluable, as did the advice of Mr. W. Miller in the obtaining and processing of the photographic material.

I am particularly grateful to my thesis advisor, Dr. J. B. Oke who, in addition to supplying some of the observational material, provided instruction in the operation of most of the equipment used in obtaining and reducing the observational material. Of particular value were the many hours of discussion with Dr. Oke which served to open new avenues of investigation, overcome some of the difficulties encountered in obtaining and interpreting the observations, and to provide much-needed encouragement in periods of uncertainty and doubt.

Assistance in the calibration and operation of the electronic apparatus was supplied by Dr. E. W. Dennison and the staff of the Astro-Electronics laboratory at Caltech.

Of no minor importance was the aid of the Mount Wilson staff of night-assistants, particularly Gene Hancock and Ray Jacques whose commentaries on the real world served to preserve some degree of wakefulness in the later hours of long winter nights.

In the preparation of the manuscript from hand written copy, the nimble fingers of Mrs. Margaret Hayden were essential. When disagreements over spelling arose, we took an average. The peculiar grammar is, however, my own.

Miss Marcia Prunty, now my wife, assisted in the proofreading and in the preparation of the figures and tables. Of greatest value, however, was the encouragement and understanding which she provided during the more trying periods in the writing of this manuscript.

Finally, I should like to thank the California Institute of Technology for the financial assistance provided via scholarships, fellowships, and assistantships during both my graduate and undergraduate careers at that institution.

ABSTRACT

Photoelectric and photographic spectrophotometry have been utilized to infer some of the properties of the nuclear regions of eight Seyfert galaxies and two additional objects displaying somewhat more normal spectra. The observations were principally made during 1966 and 1967 and cover much of the region between 3300Å and 10,000Å. For each of the objects, absolute continuous energy distributions are obtained. In addition, the relative and absolute emission-line intensities and profiles were derived from the observational data. It is found that the emission-line profiles, and the profiles of the Balmer line cores can be consistently interpreted in terms of mass-motions and/or turbulence within the emitting regions. The wings of the Balmer lines are difficult to interpret in this fashion and evidence is presented which indicates that the relevant broadening mechanism is electron scattering. This process requires that the emission nuclei possess significant optical depth in the Balmer lines. The anomalously steep Balmer decrements which are observed, as well as the presence of the Balmer wings, may also be consistent with such optical depth. Absorption lines seem to be extremely weak, or absent, in the nuclear spectra and the continuous energy distributions bear little resemblance to those of

normal nuclei. The presence of a relatively flat non-thermal component to the observed spectrum is indicated. Approximate forms for these non-thermal spectra are derived from the observational data and auxiliary calculations. It is found that this non-thermal flux constitutes a large part of the blue and ultraviolet fluxes observed in the Seyfert nuclei. It is this component which is responsible for the unusually blue colors of these objects and for the weakness of the absorption lines. This non-thermal component may also be responsible for the observed wide ranges of ionization. Rough calculations indicate that sufficient ionizing flux will result from an extrapolation of the optical non-thermal spectrum to the far ultraviolet.

It is concluded that the Seyfert nuclei are objects characterized by large internal velocity dispersions, a sizeable non-thermal component, and significant optical thickness in the Balmer lines. The levels of ionization are quite mixed in the line-emitting regions and the source of this ionization is either synchrotron photons or the conversion of the kinetic energy of cloud motions into ionization energy by means of cloud interactions. Of the two, the former seems the more likely. Finally, the sources of the excitation are considered, but no clear distinction between the various mechanisms is possible on the basis of the available data.

TABLE OF CONTENTS

I. INTRODUCTION

A. General Properties of Seyfert Galaxies

The spectra of many galaxies show one or more emission features in addition to the usual absorption spectrum. The most commonly encountered of such emission features is the λ 3727 doublet of [OII] . Approximately half of the spiral galaxies observed by Mayall (1939) showed such emission in the nucleus or the spiral arms. Page (1952) has noted that those galaxies in which he observed this [OII] emission also showed H_α in emission. Galaxies possessing strong and rich emission spectra are, however, rare. In this latter group are to be found such objects as the N-type galaxies, some of the compact galaxies described by Zwicky (1964, 1966), the emission-line Haro galaxies (Haro 1956, DuPuy 1968), and the Seyfert galaxies. Some of the quasi-stellar sources may also belong to the group of emission-line galaxies.

The Seyfert galaxies derive their name from the work of Carl K. Seyfert (1943) in which the nuclear emission in six spiral galaxies, NGC1068, NGC1275, NGC3516, NGC4051, NGC4151, and NGC7469, was investigated. The common characteristics of these objects noted by Seyfert were (1) the presence of a rich emission spectrum composed of high excitation lines such as are found in the spectra of

planetary nebulae, (2) the great widths of these emission lines which, when expressed as Doppler widths, are in excess of about 1000 km/sec., and (3) the presence of a stellar, or semi-stellar nucleus contributing a significant portion of the total optical luminosity of the galaxy. It should be emphasized that these "Seyfert nuclei" are distinct features located in the centers of the galactic nuclei. In general, the nuclear regions of the Seyfert galaxies appear normal aside from the presence of this separate feature. The present observations indicate that the greater portion of the observed line emission rises from this Seyfert nucleus.

To the above trio of characteristics should be added a fourth: The Seyfert galaxies are spirals, usually with fairly normal-appearing spiral structure. NGC1275 was classified as an elliptical in Seyfert's study and has since been variously classified as an elliptical, irregular, or peculiar galaxy. However, Minkowski (1968) has pointed out that spectra of the regions external to the Seyfert nucleus of NGC1275 show an A-type absorption spectrum, hardly characteristic of elliptical galaxies. Furthermore, short-exposure direct photographs of this object show definite indications of spiral structure. NGC1275 should therefore be regarded as a spiral galaxy of somewhat peculiar nature. A number of objects have

since been added to the Seyfert category by various authors. To the extent that classifications are available for these objects, all seem to possess spiral structure.

Six additional objects, NGC2782, NGC3077, NGC3227, NGC4258, NGC5548, and NGC6814, were listed by Seyfert as probable Seyfert galaxies but were not investigated in detail. More recent work (Burbidge, Burbidge, and Prendergast 1963, Burbidge 1968) has indicated that NGC2782, NGC3077, NGC4258, and probably NGC6814, deviate in one or more respects from the characteristics listed by Seyfert. In the cases of NGC4258 and NGC6814, the present work confirms this "rejection" on somewhat different grounds. The remaining pair of objects, NGC3227 and NGC5548, are found to satisfy the Seyfert criteria and may be regarded as Seyfert galaxies.

Many of the features characteristic of the spectra of the Seyfert galaxies were noted at an early date. Fath (1908) noted the presence of five emission lines in the spectrum of NGC1068 and Slipher (1917) indicated the great width of these lines in observing that they appeared as "discs" rather than as monochromatic images of the slit on the spectrogram. Campbell and Moore (1918a,b) also noted the presence of emission lines "fully 30 Ångstroms wide" in spectra of NGC1068. The latter authors observed emission lines of several Ångstroms width in NGC4151 as well. Hubble

(1926) reported planetary-like emission lines in the spectra of NGC4051 as well as in spectra of NGC1068 and NGC4151. Detailed descriptions of the emission spectra of NGC1275 and NGC4151 were published by Humason (1932) and Mayall (1934), respectively. Mayall also observed broad Balmer-line emission in NGC3516 and NGC7469 (Seyfert 1943).

Following the work of Seyfert, these objects were largely ignored for over a decade. Interest was renewed when problems arising from the discovery of the extra-galactic radio sources directed attention to the occurrence of energetic events within galaxies (Minkowski 1957). Further impetus was provided by the appearance of the enigmatic quasi-stellar sources. The spectra of these objects often showed broad emission lines. This factor, together with the stellar appearance of the quasi-stellar sources, prompted suggestions by Burbidge, Burbidge, and Sandage (1963) and by Shklovski (1965) of a possible relationship between the Seyfert nuclei and the quasi-stellar sources.

Most of the attention directed toward the Seyfert galaxies has been concerned primarily with the interpretation of the emission-line spectra. Woltjer (1959) attempted to explain the observed line widths by rotation, hypothesizing the presence of a massive nuclear condensation. Burbidge, Burbidge, and Prendergast (1959, 1963) examined the rotational properties of NGC1068 and NGC7469

and placed rather stringent limitations upon the massiveness of a nuclear condensation such as that postulated by Woltjer. As an alternative, it was suggested that the line widths were a manifestation of the ejection of material from the nuclear regions, probably as a consequence of the occurrence of violent events in the nuclei. The basis for this suggestion was the observation that the velocities indicated by the line widths were in excess of the estimated velocities-of-escape for the systems.

One of the difficulties encountered with either of the above interpretations is the failure to account for differences in the line widths or profiles. The differences are most notable in comparing the profiles of the forbidden lines to those of the Balmer lines, the latter generally possessing an extensive winglike structure absent from the forbidden line profiles. (This phenomenon is observed in all of the Seyfert galaxies with the exceptions of NGC1068 and NGC3516.) An explanation of these profile differences based upon electron scattering was suggested by Field (1959). Dibai and Pronik (1968) indicated that stratification of the line-emission regions might account for the differences in profile.

That the kinematical structure of at least some Seyfert nuclei is complex is indicated by the work of Walker (1968a, 1968b) in which detailed spectrographic studies of the nuclei of NGC1068 and NGC4151 show the

presence of a system of two or more discrete clouds with differing line-of-sight motions and differing emission properties. Somewhat earlier, spectroscopic studies of NGC1275 indicated a system of streams, or "jets", of material being ejected from the nuclear regions (Burbidge and Burbidge 1965).

The line-emission spectra of the Seyfert nuclei are rather difficult to interpret. One of the problems is the presence of emission lines arising from ions of a wide range of ionization potential. The most extreme instance encountered is the spectrum of NGC4151 which shows emission lines of [FeXIV] λ5303 (Ionization Potential 355 eV.) and of [OI] (Oke and Sargent, 1968). The presence of such disparate ions lends weight to suggestions of stratification, and further suggests the occurrence of shock phenomena such as encountered in the solar corona. The latter may be a consequence of collisions occurring between high velocity clouds. Calculations of relative line intensities based upon such shock-models show some promise of being applicable to Seyfert nuclei (cf. Williams and Weymann 1968).

Detailed considerations of the excitation and ionization mechanisms responsible for the observed emission spectra have been made by Osterbrock and Parker (1965) and by Dibai and Pronik (1968). The latter authors, as mentioned, interpreted the relative line

intensities, and differences in the emission profiles, in terms of models in which two or three distinct regions were responsible for the observed emission. These regions were distinguished by differences in density, temperature, and internal turbulent velocity. The importance of electron scattering in forming the wings of the Balmer lines has been discussed by Oke and Sargent (1968) but certain difficulties remain in this regard.

One of the largely neglected peculiarities of the Seyfert emission spectra is the presence of rather steeper Balmer decrements than those predicted by theory. The intensity ratio H_α / H_β is particularly anomalous. Osterbrock and Parker (1965) reported an H_α / H_β ratio of about 12.5 in the spectrum of NGC1068. For the other Seyfert nuclei, H_α / H_β ratios ranging from about 3.5 (in NGC5548) to about 17 (in NGC3227) are found from the data of the present study. In comparison, the theoretical values for Baker-Menzel Cases A and B are somewhat less than 3 for the temperatures of interest.

At present, the primary sources of ionization and excitation have not been clearly ascertained. Various mechanisms including direct thermal excitation by collisions, excitation by collisions with high energy particles, and direct radiative excitation as a consequence of large fluxes beyond the Lyman limit, have been investigated. Individually, each hypothesized mechanism suffers either

from discrepancies between observed and predicted behavior or, more frequently, from the absence of the relevant observational data. With regard to the fundamental energy sources, a number of possibilities have been considered including cloud collisions (Osterbrock and Parker, 1965), acceleration of particles by a magnetic field (Schatzman, 1968), and the occurrence of supernova within the nuclei (Colgate, 1968). The possibility of stellar collisions has also been considered as a primary mechanism.

Detailed studies of the continuum properties of the Seyfert spectra are rather scarce. Broad-band photoelectric observations have indicated that the Seyfert nuclei, in comparison to the nuclei of normal spirals, show an excess of radiation in the ultraviolet (Osterbrock and Parker 1965, Walker 1968a). Recent infrared observations by Pacholczyk and Wisniewski (1967), Pacholczyk and Weymann (1968a) and by Low and Kleinmann (1968) indicate a similar excess exists at these longer wavelengths. The presence of optical polarization in the light of the nuclear regions has been noted for a number of Seyfert galaxies (Dibai and Shakhovski 1966, Hagen-Thorn and Dombrovski 1967, Visvanathan 1968). This polarized component arises from the Seyfert nucleus and is found to decrease in importance with increasing wavelength over the region spanned by the usual UBVR filters

(Oke and Visvanathan, 1968). The suggestion that the source of the polarized component is identical to the source of the ultraviolet and infrared excesses is a natural one. Such a suggestion would be considerably strengthened by the observation of infrared polarization.

Of the galaxies in Seyfert's list, only NGC1068 (=3C71) and NGC1275 (=3C84) are moderately strong radio sources. Although it is one of the nearest and brightest of the Seyfert galaxies, NGC4151 is only a very weak source in the radio region (Heeschen and Wade, 1964). The remaining Seyfert galaxies possess little or no observable radio emission although some relatively strong radio sources, such as 3C120, have more recently been added to the Seyfert category.

The moderately strong radio spectrum of NGC1275 is rather complex and possesses a time-varying component (Dent 1965, Kellermann and Pliny-Toth 1968). 3C120 has a flat radio spectrum which displays rather extensive radio variations (Kellermann and Pliny-Toth, 1968). Such behavior has prompted a search for optical variations. NGC1068 has been reported to show variations of possibly one magnitude in a period of about a day (Pacholczyk and Weymann, 1968a) and the same authors (1968b) have reported smaller optical variations in NGC4151. Optical variations have also been reported in some objects which have tentatively been classified as Seyfert galaxies. Included in

this latter group is 3C120 (Kinman 1968).
Variations in the appearance of the spectra of NGC4151 and NGC3516 have been reported by Smith, Weedman, and Morgan (1968) and by Andrillat (1968), respectively. In the case of NGC4151, the variations can be interpreted as a change in the continuum level only, the relative emission-line intensities remaining unchanged. For NGC3516, however, the reported variations over a twenty-four year interval are in the appearance of H_β relative to the forbidden lines. This latter variation is confirmed by the present study and some evidence for a continuum variation is also presented. When compared to Seyfert's (1943) observational material, the data of the present study indicated little evidence for emission-line variations in NGC1068, NGC1275, NGC4051, NGC4151, and NGC7469.

A natural consequence of the renewed interest in the Seyfert galaxies has been the discovery of a number of objects which have been tentatively classified as Seyfert galaxies. NGC1566, a southern spiral described by Sersic (1957) possesses the characteristic Seyfert properties (deVaucouleurs and deVaucouleurs, 1968). Two Zwicky objects, IIZw-14 (3C120) and IIIZw-2 also display these properties (Sargent 1967, 1968; Arp 196). Khachikian (1968) has classified two Markarian objects, numbers 9 and 10, as Seyfert galaxies (see also: Arp, Khachikian, Lynds, and Weedman, 1968). Finally, VV150, of the Voronsov-Vel'yaminov

catalogue, may also be a Seyfert galaxy (Sargent, 1968). The classification of some of these objects as Seyfert galaxies should be regarded as tentative, pending a more detailed examination of their properties and, of equal importance, a more precise specification of what is meant by a Seyfert galaxy. The difficulties encountered in the classification of emission-line galaxies, particularly in regard to the latter factor, are discussed below.

B. The Problems of Classification

There exists some disagreement concerning the subclassification of galaxies with rich emission-line spectra. The observational distinctions between objects variously classified as Seyfert, N-type, or compact galaxies are, in many instances, unclear. Individual objects have been given various designations, by various authors, on the basis of differing observational approaches, techniques, or classification criteria. Ideally, the assignment of a given object to a given category should be a function only of the intrinsic properties of that object and independent of such extraneous factors as the distance of the object, the instrumental resolution, or the techniques of the observation. In the present context, this ideal has clearly not been realized.

To illustrate, and hopefully to illuminate, some of the difficulties involved in the classification of

emission-line galaxies, we shall first consider those properties commonly attributed to Seyfert galaxies: Seyfert (1943) noted that each of the six objects contained in his study was a spiral galaxy possessing "...an exceedingly luminous stellar or semi-stellar nucleus which contains a relatively large percentage of the total light of the system." This nucleus appears as a separate feature located within a more normal-appearing nuclear region. For this group of six, estimates of the fraction of the total light arising from this nucleus ranged from about 6 percent for NGC1068 to approximately 48 percent for NGC4151. This description should be compared to that of the N-type galaxies which, according to Matthews, Morgan, and Schmidt (1964) have "...brilliant starlike nuclei containing most of the luminosity of the system. A faint nebulous envelope of small visible extent is observed." Although quite similar, two apparent distinctions appear between this pair of definitions. First, the latter definition, or description, seems to imply that the fraction of the total luminosity arising from the nucleus is greater for an N-galaxy than for a Seyfert galaxy. Considering the range of this parameter encountered among the Seyfert galaxies, as well as the difficulty encountered in estimating the brightness of a small (and often unresolved) feature which is imbedded in a nuclear region of varying brightness, it does not seem that this criterion clearly differentiates

these two types of object. Furthermore, the number of objects classified as Seyfert or N-galaxies is rather small (about a dozen Seyfert galaxies and about twice that number of N-galaxies) with the consequence that even a statistical distinction on this basis would be, at best, only of marginal significance. The second apparent difference in the above descriptions concerns the nature and brightness of the "envelope" surrounding the nucleus. For the Seyfert galaxies contained in the present study, these "envelopes" are clearly not nebulous. Each galaxy, with the exception of NGC1275, displays fairly well-defined spiral arms. The extent of this spiral structure does not seem atypical for spiral galaxies of similar morphological type. However, considered as a group, the N-galaxies are at somewhat greater distances than are the Seyfert galaxies. The question then arises as to the affect of distance upon the classification assigned to such objects. Morgan (1968) has investigated this problem with the conclusion that, of the objects listed by Seyfert, NGC3077, NGC6814, NGC4151, and possibly NGC4051, would be classified as N-galaxies at greater distance. The last two, possibly three, objects are generally classified as Seyfert galaxies. For these objects, the relatively bright Seyfert nuclei, and surrounding nuclear regions, will be visible at greater distances than the spiral structure and the latter may well appear as a "faint nebulous envelope of small visible extent." This

conclusion suggests that some of those objects classified presently as of N-type (or, perhaps, compact galaxies), are so classified as a consequence of their distances only and would, if nearer, have been classified as Seyfert galaxies. The fact that some of the Seyfert galaxies would not be classified as N-galaxies at large distances indicates either that the N and Seyfert type galaxies comprise two morphologically distinct classes of object, or that we are dealing with a single type of object with a wide range of properties. To further obfuscate this aspect of the problem, it is noted that some of the emission-line Haro galaxies (Haro 1956) also show bright concentrated nuclei with a faint surrounding envelope. The latter is generally nebulous but irregularities in structure are sometimes apparent (DuPuy 1968).

A more definite distinction might be made on the basis of the physical dimensions of the nuclei found in each category. The Seyfert nuclei seem to have diameters of less than about 100 parsecs; the N and blue galaxies have diameters in the vicinity of 1000 parsecs. In both categories, however, the variations are large and there exist objects whose diameters are unresolved at their distances. In comparison, the quasi-stellar sources have diameters ranging from about 10^5 parsecs to dimensions unresolved at diameters of 100 parsecs (Minkowski, 1968). It would seem, therefore, that a clear distinction on this

basis is not possible.

Inclusion of spectroscopic classification criteria simplifies the problem only slightly. The emission-line Haro galaxies, for example, seem to have emission lines which, although similar in strength and type, are considerably narrower than those encountered in the Seyfert galaxies (cf. DuPuy, 1968, figure 1.) Some of the N and compact galaxies do, however, have the broad emission characteristic of the Seyfert nuclei, even to the relatively greater widths of the Balmer lines (cf. Lynds, 1968, figure 1e). At least one of the "N-galaxies", 3C177, shows no evidence of any emission lines (Lynds, 1968). It has been suggested by Arp (1968) that the contrast of the emission lines, relative to the continuum, is weaker in the N-galaxies than in the Seyfert galaxies, and yet weaker in the quasi-stellar sources. Part of this conclusion is based upon the classification of 3C120 as a compact or radio-N galaxy. Other authors (e.g. Sargent 1967, Kinman 1968) have classified this object as a Seyfert galaxy. Aside from this difficulty, and the presence of N-galaxies and quasi-stellar sources showing no line emission, it seems clear that the effects of distance or angular resolution can strongly affect this contrast: The emission-line spectrum of a Seyfert galaxy arises almost entirely within the Seyfert nucleus. The adjacent nuclear regions contribute little, if any line emission but do con-

tribute continuum radiation. Consequently, the greater the degree of widening of the spectrum, the larger the aperture used in photometry, or, equivalently, the greater the distance of the object, the greater will be the "contamination" of the nuclear spectrum with continuum radiation from adjacent regions. For a given Seyfert galaxy, the contrast of the emission lines will decrease as the angular resolution decreases or the distance increases. Such an effect is particularly noticeable in the case of an object like NGC1068 which has a very bright central region. Considered as a group, the Seyfert galaxies are nearer than the typical N-galaxy which is, in turn, nearer than the typical quasi-stellar source. The dependence of observed line-contrast on object type, as suggested by Arp, does not preclude the possibility that the intrinsic contrast is the same for all types of object. It should be noted, in this regard, that an angular resolution limit of about one second of arc is set by the seeing conditions. The angular diameters of most of the emission-line regions of these objects are comparable to, or smaller than, this seeing limit.

A similar difficulty arises in connection with the suggestion by Morgan (1968) that the presence of an underlying G-type absorption spectrum is a characteristic of the Seyfert galaxies. The indications are that this absorption spectrum is not a characteristic of the Seyfert

nuclei but, rather, is another manifestation of "contamination" from the surrounding nuclear regions. Oke and Sargent (1968) observed that unwidened spectra of the Seyfert nuclei of NGC1068 and NGC4151 obtained under conditions of good seeing, showed no evidence of absorption features. The present study indicates that this observation is applicable to six additional Seyfert galaxies. (NGC3227 is a possible exception: The spectra obtained were exposed under very poor seeing condition. Very weak H and K lines and G-band absorption are present on the spectra.) The prominence of this absorption spectrum will therefore vary in a manner opposite to the emission line contrast: As the resolution decreases, due to distance, seeing, or widening, the absorption spectrum will increase in strength. In this connection, the H and K lines of CaII and the G-band appear in the spectra of the emission-line Haro galaxies and some N-type galaxies (DuPuy 1968, Lynds 1968) and may be somewhat more prominent than in correspondingly widened Seyfert spectra.

Burbidge (1968) has pointed out that the $\lambda 3727$ doublet of [OII] is quite strong in the Seyfert nuclei but weak or absent from the emission spectra of the quasi-stellar sources. Since the relative strengths of the other emission lines are comparable, this can probably be interpreted as a difference in the electron densities occurring within these two groups. On the basis of such spectroscopic

evidence as is available for the N-galaxies (Lynds, 1968) there seems to be no difference in the strength of this [OII] emission between the N-type and Seyfert galaxies. The emission-line Haro galaxies also show [OII] emission of comparable strength. Markarian 9, tentatively classified as a Seyfert galaxy by Arp, Khachikian, Lynds, and Weedman (1968), shows little or no emission at λ3727.

A second distinction between Seyfert nuclei and quasi-stellar sources appears in connection with the absorption spectra. The absorption features appearing in widened Seyfert spectra often include resonance lines found also in the quasi-stellar sources. These lines are usually quite broad, being usually somewhat narrower than the forbidden emission lines. In the quasi-stellar sources, on the other hand, these lines tend to be quite sharp (Burbidge, 1968). The corresponding widths of the rather weak absorption lines in the N-galaxies are not known.

Broad-band photometry has proved useful in classifying galaxies as well as stars. For the emission line galaxies presently under discussion, this approach suffers from several drawbacks. It has been pointed out by Minkowski (1968) that the integrated colors of the Seyfert galaxy NGC4151 are barely abnormal although the nuclear colors are quite anomalous, being unusually blue. Consequently, the distance-resolution difficulties are

still present as the colors obtained for an object such as NGC4151 will depend upon the photometer aperture and the distance. Furthermore, the strengths of the emission lines relative to the continuum and to each other vary considerably among the Seyfert galaxies. To the extent that these emission lines contribute significantly to the observed flux within a given filter-bandpass, they may affect the colors significantly. Generally, such photometry will contain information both about line emission and the continuous energy distribution, but the two cannot be separated without additional data of high resolution. The same arguments also apply to polarimetric observations. Some tendency has been noted for the quasi-stellar objects, N-galaxies, and Seyfert nuclei to separate in the conventional two-color diagram (Sandage 1967, Westerlund and Wall, 1968). This distinction is not a strong one, particularly between the N- and Seyfert galaxies, insofar as there is considerable overlapping of the regions occupied by the various types of object.

Perhaps some improvement in the classification problem will result from the fairly recent observations in the infrared. The observations of Low and Kleinmann (1968) showing excesses in the infrared brightness of Seyfert nuclei, as compared to normal galaxies, may prove to be a distinguishing characteristic of these objects. Such observations should be made of the N- and compact galaxies

to ascertain the nature of such a distinction. Similarly, polarization observations of these objects might provide grounds for differentation from the Seyfert objects in which optical polarization is observed in some intances.

Optical and/or radio variability as a classification criterion would seem to be inadequate. Both radio and optical variations have been observed in Seyfert galaxies. Some of these objects, however, show no such variation. Among the radio-N galaxies and the radio-quiet compact galaxies are found objects which are optical or radio-variables and objects which are neither. There is, at present, insufficient evidence to conclude that the objects are intrinsically different in this regard.

The quasi-stellar sources are the most luminous objects known (assuming the red-shifts are cosmological) having total luminosities ranging from roughly 10^{45} to 10^{48} erg/sec (Low and Kleinmann, 1968). The Seyfert galaxies are generally less energetic, with luminosities ranging from about 10^{44} to 10^{46} erg/sec, and the compact and N-galaxies seem to be intermediate in luminosity. "Normal" galaxies have luminosities ranging from about 10^{43} to 10^{45} erg/sec. On the basis of luminosity alone, only rather crude group properties can be distinguished. There is a good deal of overlapping between the luminosity ranges of the various types of object. In many intermediate cases no classification on the basis of luminosity

alone is possible: For example, Seyfert galaxies such as NGC1275 and 3C120 are more luminous than some quasi-stellar sources while others, such as NGC1068 and NGC4151, are comparable in total luminosity to the more luminous normal galaxies.

In view of the above difficulties, it is not clear that the emission-line galaxies can be arranged into a truly discrete classification system. That is, the observational evidence does not preclude the existence of a continuum of objects connecting the most energetic quasi-stellar sources to the normal galaxies. If the latter is the case, the existing classification scheme serves only to indicate the approximate location of a given object in this continuum. The evidence for such a continuum of properties is particularly strong in relation to the compact, N, and Seyfert galaxies. If we strictly apply Seyfert's original three criteria, we will find that some of the N- and compact galaxies, and perhaps some of the quasi-stellar objects, will fit the Seyfert category. Adding the requirement that the object be a spiral galaxy omits only those objects in which spiral structure is not observed, and which have distances such that this structure would be observable if present. These distances should, of course, be based upon the observed radial velocities rather than upon luminosity criteria. Continuum properties such as, say, the relative importance

of thermal and non-thermal radiation sources, or the total luminous energy might serve as continuous classification indicators. These objects might be further divided into objects arranged according to the properties of their radio emission. It should be clear, in any case, that the present classification system imparts relatively little information about the nature and significant properties of the objects to which it is applied.

C. The Purposes and Scope of the Present Study

The principal aim of the present study is to investigate those properties of the Seyfert galaxies which might provide information as to the physical conditions occurring within the Seyfert nuclei. Because of the uncertainties of classification, the present work is concerned with objects generally regarded as members of the Seyfert group. The six objects originally investigated by Seyfert (1943), NGC1068, NGC1275, NGC3516, NGC4051, NGC4151, and NGC7469, were included. Of the six additional objects listed by Seyfert, two additional galaxies, NGC3227 and NGC5548, generally considered to be Seyfert galaxies, were included. Finally, the continuous energy distributions of NGC4258 and NGC6814 were obtained. Those two objects had been rejected as Seyfert galaxies by other authors but were included in the present study in order to ascertain whether their continuum properties differed significantly from those

of the Seyfert galaxies.

Emphasis was placed upon the properties of the nuclear continua. For this reason, photoelectric "scanner" observations were made during 1965-1967 covering most of the wavelength region between 3000Å and 10000Å. From these observations, the absolute continuous flux distributions were derived. These observations are discussed in Section II.

During the same period, photographic spectra of the Seyfert nuclei were also obtained. These spectra provided greater wavelength resolution than did the photoelectric observations. When calibrated by the photoelectric data, these spectra were utilized to obtain relative and absolute emission line intensities, and relative intensity profiles for a representative sample of the emission lines. The photographic observations are discussed in Section III.

Section IV is concerned with the interpretation of the emission-line spectra. Kinematical properties were estimated from the line profile information. The conditions of temperature and electron density within the Seyfert nuclei are inferred from the forbidden line intensities. The possibility of significant stratification within the emitting regions is briefly discussed in the context of the line intensities and profiles observed. A number of possible causes for the anomalous behavior of the Balmer decrements are considered as are the mechanisms responsible

for the presence of broad wings in the hydrogen lines.

From an examination of the continuous energy distributions, it soon became apparent that these distributions could not be interpreted as a reasonably normal stellar component plus a Balmer recombination continuum. In addition to such stellar and gaseous components, it was found necessary to postulate a third, presumably non-thermal, component in order to explain the observations. An attempt is made to specify the properties and relative importance of each of these three components. This decomposition of the optical continuum is discussed in Section V.

Section VI is primarily concerned with the problems of ionization and excitation. Various mechanisms for providing the observed ionization levels and emission-line behavior are considered in light of the conclusions of the previous sections. The energy sources of the Seyfert nuclei are investigated and hypotheses regarding the primary, or fundamental, energy sources are considered. Finally, this section summarizes the conclusions obtained from consideration of the observational material in regard to the processes and properties of the Seyfert nuclei.

II. PHOTOELECTRIC SPECTROPHOTOMETRY

A. Instrumentation and Instrumental Calibrations

Photoelectric observations of the nuclear regions of the Seyfert galaxies were made at the f/16 foci of the Mount Wilson 60- and 100-inch telescopes using the Cassegrain photoelectric spectrophotometer ("scanner"). The scanner optical system is of the Ebert-Fastie type (Fastie 1952, Code and Liller 1962) with collimator and camera focal lengths of approximately 32 inches. The 600 lines per millimeter grating is blazed at 3500Å in the second order producing a second-order dispersion of 10Å/mm at the exit slit. The exit slit is adjustable permitting the bandpass to be set to any value between 1Å and 70Å in the second order. For the present study, the instrument was used in slitless form, the usual entrance slit being replaced by a slide containing six circular apertures with diameters ranging from approximately 1 mm. to 13 mm. These apertures were covered by a thin glass plate which reflected a small portion of the incident light to an auxilliary guiding and centering eyepiece. An off-axis guiding eyepiece, to be used in conjunction with a suitable field star, is also provided.

Scanning in wavelength is accomplished by rotating the grating. A counter coupled to the stepping

motor which drives the grating reads the second-order wavelength centered on the exit slit directly in second-order Ångstroms. This scale is readable to an accuracy of about ±0.5Å and calibration procedures indicate that the wavelength can be set with an accuracy of ±1Å, or better, over the range of interest.

For observations in the "blue" region (λ3300-λ6055) the scanner was operated in the second order with a yellow filter inserted for wavelengths above about 4700Å to eliminate the third order violet spectrum. In the "red" region (λ4785-λ10,000), the first order spectrum was scanned, an amber filter being used at λ6370 and above to eliminate the contribution of the second-order spectrum.

The detectors employed consisted of an RCA 1P21 (S-4) photomultiplier operating at 775 volts in the "blue" region and an ITT Fw-130 (S-20) photomultiplier, operating at 1700 volts, for "red" region observations out to about λ8400. Some additional observations were made between 7000Å and 10,000Å using an RCA 7102 (S1) photomultiplier operating at 1500 volts. These photomultipliers were mounted in "cold boxes" at the exit slit of the scanner and were operated at dry-ice temperature.

The output of these detectors was recorded by one of two data systems. For some of the earlier "blue" region observations made at the 60-inch telescope, a direct-current system was employed. The output current

of the photomultiplier was directed to a General Radio Electrometer-Amplifier which was, in turn, connected to a Brown recording milliammeter. The amplifier provides switch-selected decade steps in gain. An auxilliary resistance box provided five additional half-magnitude gain increments. With this system the observational material consisted of a series of deflections on a continuous chart with associated gain settings, wavelength settings, and times of observation entered on the chart manually. Other necessary data such as object identification and the bandpass employed were similarly recorded.

For the majority of the observations, pulse-counting techniques were employed. The pre-amplified output of the photomultipler was sent, via coaxial cable, to a remote station. The incoming pulses were there amplified and subjected to pulse-height discrimination. Pulses of amplitude greater than a specified threshold level then generated fixed amplitude pulses which were counted by standard techniques. A preset integration interval was clocked by an accurate internal oscillator. At the end of the preset integration period, the total count of pulses detected within that interval was recorded. With the 60-inch pulse counting system, the bandpass, wavelength, integration interval and time of observation were recorded manually. The 100-inch data system recorded these quantities both on printed paper

tape and on IBM cards.

The advantages of the pulse-counting approach are particularly apparent at the Mount Wilson Observatory where the ambient radio-frequency flux, due to the neighboring radio and television complex, is quite large and seems to elude the most elaborate attempts at shielding. These shielding attempts included the generous use of aluminum foil and the covering of the 60-inch dome opening with "chicken wire". The latter did not eliminate the r.f. interference but the hexagonal mesh did produce interesting optical diffraction patterns. With pulse counting techniques, much of the "interference count" can be eliminated by judicious choice of amplifier and discriminator-threshold levels.

It was necessary to perform a number of instrumental adjustments and calibrations before observations were made. The optical adjustments consisted, first, of a check of the scanner-telescope collimation which is rather sensitive to the positioning of a feed-prism. Insofar as the collimation axes of the 60 and 100-inch telescopes, relative to the scanner mounting ring are slightly different, this prism had to be readjusted every time the telescope was changed. The prism is also subject to misalignment incurred in moving the scanner from dome to dome. The scanner wavelength scale is subject to a long-term zero drift and was reset and cali-

brated at the beginning of each run of observations by means of a source producing emission lines of known wavelength. This zero-point determination was somewhat complicated by the fact that the circular entrance apertures are not exactly concentric with the optical axis of the system. The zero-point correction, and hence the wavelength setting could vary by up to 5Å (second order) depending upon the choice of entrance aperture. This difficulty was largely circumvented by selecting an aperture on the basis of the previous night's seeing and then performing the calibration. If it became necessary or desirable to change the entrance aperture in the course of an evening's observations, the scale calibration, requiring only about 10 minutes, was reperformed. In practice, most observations were made with an entrance aperture of angular diameter eight seconds of arc which was sufficiently large for all but the very worst seeing conditions. The final optical calibration performed was that of the exit slit: It was found that the relationship between slit setting and effective bandpass was slightly non-linear, particularly below $\Delta\lambda \sim 5$Å (second order). Consequently, a calibration of the slit setting was performed and rechecked occasionally. With this calibration, the exit slit could be set to an accuracy of about ± 0.1Å for second-order bandpasses in excess of 1Å. In practice, the smallest bandpass employed was 2.5Å, most being in

excess of 5Å.

In using the direct-current system, the only calibrations required other than a zero-point setting were of the input resistances which determine the amplifier gain. The decade-step resistances were calibrated at the beginning, middle, and end of each night's observations using an internal reference cell. The more stable resistances for the half-magnitude steps were calibrated less frequently using an auxilliary reference cell. The zero settings of amplifier and recorder were checked approximately ten times per night.

Calibrations of the pulse-counting apparatus were more numerous and more complex. First, the optimal combination of tube voltage, amplifier gain, and threshold level had to be determined. This was accomplished by providing a stable light source incident upon the photomultiplier. For each tube voltage, the amplifier gain and threshold levels, whose quotient defines a discrimination level, were varied and the resulting count-rates recorded. A discrimination level was then selected which suppressed the internal noise and gave a counting level which was relatively insensitive to slight changes in amplifier gain or threshold level or both. The voltage level was then selected which gave the best signal-to-noise ratio for the anticipated counting rates. It was found that, for a given detector-electronics combination, the optimal voltage,

amplifier, and threshold levels were quite stable over quite long intervals of time and with large changes in conditions of temperature and humidity.

Of greater consequence, and complexity, was the determination of the coincidence correction. The detection systems employed are characterized by a finite "dead time" between the detection of an incoming pulse and the relaxation of the system to a state wherein the next pulse can be detected. That is, only the first of a group of pulses arriving within this interval is detected. Obviously, the greater the true pulse rate, the greater will be the correction required to obtain the true rate from the measured counting rate. To permit the simple determination of this coincidence correction at the telescope, various schemes were attempted. The degree of success in such attempts was variable, but generally poor. Essentially, the problem is to provide a series of light intensities, of known ratio, to the photomultiplier, determine the correction required to obtain the known ratios from the corresponding count-ratios as a function of counting rate. Use of the entrance apertures to define the intensity levels proved unsatisfactory because of collimation and uniformity of illumination difficulties. Neutral density filters were employed satisfactorily in a laboratory situation but

were cumbersome and produced defocussing and surface-reflection problems at the telescope. The procedure finally adopted consisted of finding a wavelength region of about 50Å extent over which the response of the system to a continuous source was constant or varied slowly and linearly with wavelength setting. The exit slit was centered on this region and used to specify the relative intensities incident upon the photomultiplier. This procedure seemed quite satisfactory and the resulting coincidence corrections agreed quite well with those determined with the more elaborate laboratory procedures.

It was found that the coincidence corrections can depend critically upon the photomultiplier voltage (i.e. the mean pulse amplitude) and seems also to vary with other factors such as temperature and humidity. Roughly, the coincidence corrections to 10^5 counts per second were about 15 percent for the tubes and voltages employed. This correction could vary by several percent (i.e. from 12 percent to 18 percent) with time for a given tube, voltage, amplifier gain, and threshold level. To avoid the difficulties produced by these variations and the uncertainties in the derived coincidence corrections, the counting rates were kept below a maximum of about 4×10^4 sec^{-1} at which the correction (quite accurately proportional to rate) would be in the vicinity of 6 percent, with uncertainties less than about

one percent. This was accomplished by using smaller bandpasses in observing the brighter objects. For the Seyfert nuclei, the observed counting rates were such as to render the coincidence correction negligible. The extinction determination, however, is based upon a system of relatively bright standard stars which produce quite large counting rates. In practice , the coincidence correction was determined at about a dozen points below 10^5 sec^{-1}, the percentage correction varying quite linearly with counting rate (indicating that only 2-pulse coincidences are significant). Such a determination was made at least once during each run of observations.

B. Observational Procedures and Techniques

While continuous scanning in wavelength, at preset rates, is provided by the scanner system, this feature was not utilized for the present observations. Instead, a set of wavelength points was selected and the signal integrated at a time interval at each. When the aperture and bandpass had been set, the object of interest was centered upon the entrance aperture and, for the galaxies, a field star was centered in the off-axis guiding system. The first of the wavelength points was selected and the grating set accordingly. The counts were then recorded for the desired interval, or the direct-current signal recorded for a similar interval.

The telescope was then moved to an adjacent "empty" region of sky and the sky-plus-dark count, or deflection, recorded for the same interval, the difference between these two counts or deflections presumably being the contribution from the object alone. The next wavelength point was then selected and the process repeated.

Insofar as the signal from the standard stars was, in general, very much larger than that due to the sky or dark counts, the sky-plus-dark measurements for the standards were made only near the limits of wavelength sensitivity of the system where the dark counts, typically 2-5 sec^{-1}, become a significant portion of the total signal.

Normally a standard sequence of wavelength points, corresponding to the points of the standard-star calibration, were observed for both standard stars and galaxies. For the galaxies, an additional set of wavelength points was included. These were chosen to isolate selected emission features or regions of continuum. A "scan" consisted of one observation of each wavelength point in increasing or decreasing wavelength order. A complete observation of an object consisted of one scan in ascending order of wavelength and a second in decreasing order, immediately following the first. Comparison of the counting rates at a given wavelength on the first and second scans was used to estimate the quality of the

observations. The bandpass and integration time remained constant during such an observation.

The wavelengths of the standard sequence were selected by Oke (1964) to fall in regions in which the spectra of the standard stars are relatively free of absorption lines. The original calibration of the standards used is referred to a 50Å bandpass but it is possible to use bandpasses of less than about 5Å without significant change in the mean monochromatic flux within the bandpass. Consequently, the choice of bandpass for the observation of the standards was, within the above limits, dependent only upon the range of counting rate desired. (which also depends upon the brightness of the standard and the telescope employed). The bandpasses used were sufficiently small to keep the counting rates below the level where the coincidence correction becomes important; that is, sufficiently small so that the maximum count rate was less than about 4×10^4 sec^{-1}. The integration interval for the standard star observations was typically 5 to 10 seconds at each wavelength point.

For the Seyfert nuclei, a 50Å bandpass was employed for virtually all observations. This choice provided sufficient resolution to isolate some selected spectral features and, usually, was large enough to produce an adequate counting rate. The integration interval was usually 60 seconds. For some of the objects, a longer

integration interval would have been desirable but was not employed because variations in sky brightness over somewhat longer intervals become significant. In this connection, such variations usually are of importance only over intervals of 5 to 10 minutes and are particularly noticeable at Mount Wilson when the brightly illuminated Los Angeles basin is partially covered by shifting masses of fog or low clouds. The variation of atmospheric extinction over similar intervals is generally negligible. The presence of an object/sky "chopper" would have considerably improved the efficiency of data gathering by eliminating the problem of sky brightness and the necessity of moving the telescope every minute or so to obtain the sky-plus-dark signal.

Observations followed a fairly fixed routine. Generally, a night's observations began with the observation of one or two standard stars. Thereafter, each observation of a galaxy was followed by another one or two standard star observations. An attempt was made to observe the standards at a relatively wide range of positions on the sky, but as close to the galaxies observed as was feasible. Such a range provided means for checking the assumptions made regarding atmospheric extinction in the reduction program (see below). No standard stars were observed below a zenith distance corresponding to sec $z = 2.5$. The galaxies were observed as close to the

meridian as was possible and under no circumstances below a zenith distance of $\sim 60^\circ$ (sec z = 2). It was required that the sky be of photometric quality at the time of observation (i.e. cloud free). The observational data for a few marginal nights were discarded when a check of the extinction curves for the individual standards displayed anomalous behavior, indicating that the assumptions made in the reduction procedures were not, in fact, valid.

C. Reduction of the Observations

In reducing the observations, the principal problem is to relate the observed counting rate or current deflection to the true flux at the surface of the terrestrial atmosphere ("sec z = 0"). This requires the determination of the atmospheric extinction and the instrumental response function, the latter including losses at the optical surfaces and the response function of the detector. The most practical approach to this determination is to employ a system of standard stars of known energy distribution. In the present study, use was made of the set of standards calibrated by Oke (1960, 1964). This calibration ultimately rests upon fitting the energy distribution of the primary standard, Vega, to a model atmosphere calculation (log g = 4, $\Theta_e = 0.525$). In accordance with the findings of Mihalas (1966), a correction of $0^m.06$ has been applied shortward of the Balmer jump, increasing the Balmer jump adopted in the

standard calibration. This calibration is given in the form: $m(\mu) = \text{Const.} - 2.5 \log F_\nu$, where F_ν is the monochromatic flux at $\nu = c\mu$ where μ is expressed in inverse microns (i.e. $\mu = 2.0$ corresponds to $\lambda = 5000\text{Å}$). Because of the choice of the standard wavelengths, F_ν can be replaced by the average flux within a bandpass $5\text{Å} \leq \Delta\lambda \leq 50\text{Å}$ centered on the standard wavelength. The constant is chosen so that $m(\mu)$ is approximately equal to the apparent visual magnitude at $\mu = 1.80 (\lambda 5556)$ which is near the effective inverse wavelength of the visual bandpass of the usual UBV system. Aside from a zero-point factor, common to all standards, $m(\mu)$ is the absolute flux, in magnitude units, of the standard reduced to zero atmosphere. Once this scale is specified, the absolute flux distributions, in the usual units, are determined.

For each observation, a wavelength λ, a bandpass $\Delta\lambda$, and a value of the zenith distance, z, computed from the object coordinates and the sidereal time of the observation are specified. For the pulse counting observations, a total count N is obtained in an integration interval Δt. For the direct-current observations, a deflection D and two gain settings, G_{10} and $G_{1/2}$ are recorded. The deflections, or counts, are here taken to be the excess over the sky-plus-dark levels. An observed "flux" is then defined by:

$$f(\mu) = \frac{DG_{10}G_{1/2}}{\Delta\lambda} \quad \text{(Direct-current observations)}$$

or: $$f(\mu) = \frac{NK}{\Delta t \Delta \lambda} \quad \text{(Pulse-counting observations)}$$

where K is the coincidence correction for the observed counting rate, expressed as the ratio of the true rate to the observed rate. Roughly $K = (1 + \epsilon \frac{N}{\Delta t})$ where $\epsilon \sim 10^{-6}$ sec.

A table of mean atmospheric extinction coefficients, $A(\lambda)$, given by Oke (1965a) was provided. Values of $A(\lambda)$ were interpolated in this table and a magnitude was computed at each observed wavelength point for each object according to:

$$m_o(\mu) = C - 2.5 \log f(\mu) - A(\mu) \sec z$$

The constant C was set equal to 25 and 18.5 for the direct current and pluse-count observations, respectively, in order that $m_o(\mu)$ should be a relatively small positive number. If the adopted extinction coefficients are identical with the true extinction coefficients, $m_o(\mu)$ is the relative flux distribution, reduced to zero atmosphere, times the instrumental response function. Accordingly, we define for the standard stars

$$\delta(\mu) = m_o(\mu) - m(\mu)$$

where $m(\mu)$ is the standard calibration. Thus, $\delta(\mu)$ is, aside from a scale factor, the instrumental response

function, in magnitude units. If the adopted extinction coefficients are correct, $\delta(\mu)$ will be independent of position or choice of standard star. If we let $\langle \delta(\mu) \rangle$ be the average value of $\delta(\mu)$ over all standards observed on a given night, the absolute fluxes, $m(\mu)$, of the non-standard objects will be given by:

$$m(\mu) = m_o(\mu) + \langle \delta(\mu) \rangle$$

Subject to the validity of the assumptions regarding the use of the mean extinction coefficients, $m(\mu)$ is the relative energy distribution of the object reduced to zero-atmosphere, in the same units, and subject to the same absolute calibration zero-point as the system of standard stars.

The use of the mean extinction coefficients $A(\lambda)$ for narrow band spectrophotometry has been discussed by Oke (1965a) who concluded the procedure yields colors (relative fluxes) of satisfactory accuracy but that the resultant distributions are subject to small grey terms. That is, the distributions so obtained are subject to zero-point variations in the distribution of $m(\mu)$. This conclusion can be directly examined on the basis of the present observational data: If the true $A(\lambda)$ correspond exactly to the mean values used, $\delta(\mu)$ will be independent of sec z or, equivalently choice of standard and time. In particular,

$\delta(\mu) = \langle\delta(\mu)\rangle$ for any standard. For each night of observation, the function $\delta(\mu)$ was plotted for each standard observed. With the exception of two discarded nights, which were considered marginal on other grounds, the present data supports the above finding of Oke. That is, within the observational uncertainties, the individual $\delta(\mu)$ differ from the average $\langle\delta(\mu)\rangle$ only by small wavelength-independent terms.

These grey terms could arise from a variety of sources. First, setting errors of the exit slit would produce just such grey deviations. However, the grey terms are generally larger than the uncertainties in the slit calibration and, furthermore, are not correlated with slit setting. A second possibility is that there exist grey errors in the calibrations of the standard stars. Since the magnitude of the correction, or grey difference, is not correlated with the choice of standard, this possibility can be similarly discarded. The third possibility, that of grey departures of the extinction coefficients from the adopted mean values is, on the other hand, supported by the behavior of the observational material. For observations closely spaced in time (i.e. made on the same night) the deviation of individual response curves $\delta(\mu)$ from the mean curve $\langle\delta(\mu)\rangle$ is proportionally greater for objects at lower elevation. A variation with time becomes significant

usually over longer time intervals (i.e. days) but may, on occasion, become significant in the course of a single night's observations. The true value, $A'(\lambda)$, of the extinction coefficients can be adequately related to the adopted mean values, $A(\lambda)$, by an expression of the form

$$A'(\lambda) = A(\lambda) + B(t)$$

where the absorption is expressed in logarithmic or magnitude units and $B(t)$, a slowly varying function of time, is small in comparison to $A(\lambda)$.

In consequence of the above, grey corrections were applied to the observational material. It was assumed that the $\langle \delta(\mu) \rangle$ for each night when averaged over all nights on which observations were made represented the true instrumental response function. (By "all nights" is meant all nights on which a given telescope and detector were employed.) It was further assumed that the true extinction coefficients, averaged over all nights, equaled the adopted mean values, i.e. that $\langle B(t) \rangle = 0$. The corrections were applied in two ways: First, the observations were reduced using the mean extinction coefficients. For each object, a grey correction was obtained by interpolating the deviations $\delta(\mu) - \langle \delta(\mu) \rangle$ for standards nearest the object in zenith distance to obtain the corresponding deviation for the object. Usually the standards employed were also close to the observation of

the unknown in time. This deviation, in magnitude units, was linearly interpolated in sec z. Applying this correction to each object, including the standards, serves to refer all objects observed to the mean "response" curve $\langle \delta(\mu) \rangle$ for the night. The $\langle \delta(\mu) \rangle$ curves were then averaged over all nights. A second correction was applied to all objects observed on a given night equal to the deviation of $\langle \delta(\mu) \rangle$ for that night from the mean of all nights. The above correction procedure could have been performed in a single step by interpolating the deviations of $\delta(\mu)$ from the mean of the $\langle \delta(\mu) \rangle$ of all nights directly. However, obtaining the deviations in two steps allows a check to be made on the possibility of a change in the response function of the system due to deterioration of the optical surfaces, etc. That the latter was not very significant over the time interval spanned by the observations is indicated by the fact that the $\langle \delta(\mu) \rangle$ for the various nights differ signficantly only in grey terms suggesting that extinction rather than instrumental, variations are most significant.

It must be emphasized that the above corrections do not, of course, affect the relative fluxes, or colors, of the objects observed, but only the zero point of the log F_ν scale. Uncertainties in "color" arise only as a consequence of uncertainties in the observed "fluxes" $f(\mu)$, or the uncertainties in the calibration of the

standard stars. (Strictly speaking, a color error will arise if B(t) varies significantly over the interval of observation. In reduction of the observations, the values of log F_ν obtained from the ascending and descending scans were averaged. To the extent that B(t) varies linearly over the interval between the beginning of the ascending scan and the end of the descending scan, this averaging results in zero-color error and fluxes referred to the true extinction coefficients at t_o, the time midway between the beginning and end of the scan observations. In practice, B(t) usually had negligible variation in the course of a single night in comparison with other sources of uncertainty.) The uncertainties in the $f(\mu)$ appear largely as "noise" on the tracing for the direct-current observations. For the pulse-counting observations, the photon arrivals can be considered independent events, Poisson statistics applied, and the standard deviation of N counts is $\sqrt{N}$. We have, therefore, two uncertainties to consider. First there is the uncertainty in the zero point of the log F_ν energy distribution obtained for each object, which does not affect the relative fluxes but does apply to the absolute fluxes and to the absolute emission line intensities. This zero-point uncertainty is expressed as the standard deviation of the interpolated $\delta(\mu)$ curves for each night upon which an object was observed from the mean of the $\langle \delta(\mu) \rangle$ curves for all nights. These standard deviations

are tabulated for each object, in each of the two wavelength regions, in Table 2 below, and are expressed as the standard deviation of the zero-point of the log F_ν scale. The second uncertainty is color-dependent and, to a first approximation, represents the counting statistics. This uncertainty will be reflected in the relative line intensities. Expressed as the standard deviations of log F_ν , at each wavelength point, this uncertainty is obtained from the scatter of the individual log F_ν , with the above grey corrections applied, about their mean and is given in the final column of Table 3. In practice, the principal source of error in the relative emission-line intensities are not those due to the photoelectric observations, but rather those arising from the photographic photometry alone.

An estimate of the validity of the grey-correction procedures described above can be obtained by examining the differences in the fluxes of the "blue" and "red" regions. These two regions were reduced and grey-corrected separately but there exist a number of overlapping wavelength points in the region λ4785-λ6055. The differences between the grey corrected "red" and "blue" region observations at these points are comparable to the color uncertainties of the individual points and much smaller than the grey, or zero-point, uncertainties. This indicates that the above correction procedure is satisfactory and suggests that the grey uncertainties tabulated (Table 2) may be larger than the true uncertainties.

D. Absolute Calibration of the Flux Distributions

The quantity obtained from the reduction of the scanner observations and the appropriate grey corrections is, within the errors, the mean flux averaged over the bandpass. Since the constant relating $m(\mu)$ and $-2.5 \log F_\nu$ is the same for both standards and unknowns, the absolute fluxes can be determined for all objects at all μ if the absolute flux F_ν is known at one wavelength for one of the standards.

We base our absolute calibration upon Code's (1960) adopted calibration for an AOV star with V = 0.00. For such an object $F_\lambda = 3.8 \times 10^{-9}$ erg cm^{-2} sec^{-2} Å^{-1} or $F_\nu = 3.9 \times 10^{-20}$ erg cm^{-2} sec^{-1}(c/s)$^{-1}$ at about $\lambda = 5560$Å or $\mu = 1.80$. This is essentially the flux at the effective wavelength of the V-bandpass. The standards of Oke are scaled so that $m(\mu) \approx V$ at $\mu = 1.80$. In particular, Vega, the primary standard, is an AOV star with V = +0.03. Consequently, we expect that the λ5560 flux from Vega should be about 3.8×10^{-20} erg cm^{-2} sec^{-1} (c/s)$^{-1}$. Since the calibration adopts M(1.8) = 0.035 we can solve for C in the expression

$$m(\mu) = C - 2.5 \log F_\nu$$

We obtain C = -48.509, hence

$$m(\mu) = -48.51 - 2.5 \log F_\nu$$

or:

$$\log F_\nu = -19.404 - 0.4\ m(\mu)$$

The above calibration was applied to the relative fluxes observed. Table 3 gives, in the first column λ ; μ is given in the second, and the third column gives $-\log F_\nu$ where F_ν is the average flux in a 50Å bandpass centered at λ. The absolute fluxes, or energy distributions, for each object observed are plotted in Figures 1. For comparison purposes, Table 4 gives the relative energy distribution of the nucleus of a normal spiral, or normal elliptical. Specifically, this is the energy distribution of the nuclear regions of NGC224 (M31) as observed by Oke (1967). The corresponding energy distribution is plotted in Figure 2. In addition to the grey or zero-point uncertainties arising from the reduction procedures, an uncertainty of about 10 percent must be added to the zero point because of the uncertainty in the adopted absolute calibration of Vega. Unless otherwise specified, all fluxes and energy distributions, as well as line intensities, refer to the flux arising within a region defined by a circular aperture of eight seconds of arc diameter, centered on the Seyfert nucleus.

E. Reddening and Radial-Velocity Corrections

The observed energy distributions for the objects

studied will differ from the true energy distributions because of the presence of obscuring material between the source and the observer. This material can be expected to produce a diminution of light of all wavelengths with the attenuation increasing toward the blue. For the wavelength region presently under consideration, the effect upon the energy distributions of the Seyfert nuclei is to steepen the true distribution. Absolute and relative emission line intensities will be similarly altered.

If the Seyfert nuclei are surrounded by obscuring material, some correction should be made for the effects of reddening occurring within the Seyfert galaxy. Since we have no direct evidence as to the amount or nature of such reddening, such corrections would be, at best, hazardous and, in the present study, no such correction has been applied.

For our own galaxy, however, such information is available. To correct for the effects of reddening within our own galaxy, the amount and wavelength dependence of the absorption must be specified for each object. It is probably safe to assume that the wavelength dependence of the galactic absorption is similar to that in the plane near the sun. Consequently, we have assumed that the reddening curve, derived photoelectrically by Whitford (1958) adequately represents the wavelength dependence of the total galactic absorption. This reddening curve can

be adequately represented for computational purposes by a pair of linear segments. From Whitford's curve, we have obtained the following expressions:

$$\Delta m_1(\mu) = 0.422\mu - 0.008 \qquad 3.00 \geqslant \mu \geqslant 2.24 \qquad 1a$$

$$\Delta m_1(\mu) = 0.723\mu - 0.683 \qquad 2.24 \geqslant \mu \geqslant 1.00 \qquad 1b$$

where $\Delta m_1(\mu)$ is the absorption, in magnitudes, at μ. An extrapolation of Whitford's curve to $\mu = 0$ approaches $\Delta m_1(0) \cong -0.378$. On theoretical grounds, it is believed that the absorption should tend toward zero as μ tends to zero (probably as μ^4). Consequently, $\Delta m_1(0)$ must be subtracted from these expressions, and we obtain:

$$m_2(\mu) = 0.422\mu + 0.370 \qquad 3.00 \geqslant \mu \geqslant 2.24 \qquad 2a$$

$$m_2(\mu) = 0.723\mu - 0.305 \qquad 2.24 \geqslant \mu \geqslant 1.00 \qquad 2b$$

The principal uncertainty in these expressions lies in the assumption that $\Delta m(\mu) \to 0$ as $\mu \to 0$ and in the extrapolation of $\Delta m_1(\mu)$ to $\mu = 0$.

Before proceeding further, we note that $\Delta m(\mu) \propto \tau(\mu)$ where $\tau(\mu)$ is the optical depth of the obscuring material at μ. Expressions 2 are, therefore, valid only for an unspecified thickness of obscuring material. (It is implicitly assumed in deriving the above that the distribution of obscuring material in the plane is uniform

to the distances attained and that $\tau(\mu)$ is proportional to path length.)

Using expressions 2 as they stand, we can calculate the absorption in magnitude units at any wavelength for the unspecified path-length for which equations 2 are valid. It will be convenient to calculate the absorption values for the B, V, and R points of the usual multicolor system, the absorption in photographic magnitudes and the color excesses for the path lengths of equation 2. The effective inverse wavelengths for the B, V, and R points are (Johnson 1966) $\mu_B = 2.275$, $\mu_V = 1.820$, and $\mu_R = 1.430$. For the effective μ of the photographic bandpass, we note that the continua of the objects studied lie between the black-body curves for T = 4000° and T = 10,000° for which $\mu_{pg} = 2.27$ and $\mu_{pg} = 2.35$, respectively (Allen 1963). To adequate accuracy we adopt $\mu_{pg} = 2.30$. From equation 2 we obtain:

$$\Delta m_{pg} = 1.341 \ , \ E_{B-V} = \Delta m_B - \Delta m_V = 0.319 \ , \ R_{BV} = \frac{\Delta m_V}{E_{B-V}} = 3.167$$

$$\Delta m_B = 1.330 \ , \ E_{V-R} = \Delta m_V - \Delta m_R = 0.282 \ , \ R_{VR} = \frac{\Delta m_V}{E_{V-R}} = 3.585$$

$$\Delta m_V = 1.011 \ , \quad CI = \Delta m_{pg} - \Delta m_V = 0.340$$

$$\Delta m_R = 0.729$$

Since at no point do we know the intrinsic fluxes

of the Seyfert nuclei, it is not possible to scale the above reddening law for each object on this basis. We can, however, make the assumption that the reddening material within our galaxy is distributed in layers of uniform density parallel to the galactic plane, the density being a function only of distance from the plane. Assuming the composition of the obscuring matter to be everywhere the same as in the solar neighborhood, the extinction will possess the wavelength dependence of the local material. The amount of absorption, in magnitudes, at fixed μ will be proportional to csc$b$, where b is the galactic latitude of the extra-galactic object. If these assumptions are valid, we need only know the absorption at some μ and b in order to specify the absorption for all μ and b.

On the basis of counts of galaxies per unit angular area as a function of magnitude and b, Hubble (1934) showed that the extinction $\Delta m_{pg} = 0^m.25$. More recent work of a similar nature by Shane et. al. (1959) resulted in a value $\Delta m_{pg} = 0^m.46$ at the poles. The difference between these values arises largely as a consequence of the corrections applied by the latter authors to allow for the effects of red-shift on the counts of fainter galaxies. If we adopt the Shane et. al. value, we must multiply equations 2 by 0.46/1.34 = 0.343 to obtain the polar reddening law. Hubble's value suggests that 0.25/1.34 = 0.187 is the appropriate multiplicative factor. Alternatively, we can

consider the values of color excess. Arp (1962) has summarized the available data on color excesses derived from a variety of methods. The mean value adopted is $E_{B-V} = 0^m.058$ at the pole, suggesting that we should multiply equations 2 by 0.058/0.319 = 0.182. For various assumed values of Δm_{pg} at the poles, we have:

Δm_{pg}	0.100	0.150	0.200	0.250	0.350	0.460
Δm_B	0.099	0.149	0.198	0.248	0.347	0.456
Δm_V	0.075	0.113	0.151	0.188	0.264	0.347
Δm_R	0.054	0.082	0.109	0.136	0.190	0.250
E_{B-V}	0.024	0.036	0.048	0.059	0.083	0.110
E_{V-R}	0.021	0.032	0.042	0.053	0.074	0.097
CI	0.025	0.038	0.051	0.063	0.089	0.117

Perhaps the best determined quantity is E_{B-V}. The values listed by Arp (1962) have a mean of 0.058 $\pm$0.004 If one value of 0.050 is ignored, we have 0.060 $\pm$0.001. These values suggest that the extinction at the poles is about $0^m.25$, insofar as $\Delta m_{pg} = 0^m.46$ yields $E_{B-V} = 0.11$. The determination by Holmberg (1957) gives $\Delta m_{pg} = 0^m.26$ (and CI = 0.062) at the pole. More recent work by Peterson (1968) yields values of $\Delta m_{pg} = 0.15 \pm 0.05$ and $E_{V-R} = 0.023 \pm 0.006$, both values being about 75 percent of the true values based upon Peterson's estimation of selection effects due to the cloud model assumed. His E_{V-R} value seems to indicate either a lower value of Δm_{pg} or that the assumed reddening law is incorrect.

For the correction of the observational material, we shall adopt $\Delta m_{pg} = 0^m.25$ at the poles and the Whitford reddening curve. The extinction law is then,

$$\Delta m(\mu, b) = [0.078\overline{7}\mu + 0.069\overline{0}] \csc b \qquad 3.00 \geq \mu \geq 2.24 \qquad 3a$$

$$\Delta m(\mu, b) = [0.134\overline{8}\mu - 0.056\overline{9}] \csc b \qquad 2.24 \geq \mu \geq 1.00 \qquad 3b$$

or:

$$-\Delta \log F_\nu(b) = [0.0315\mu + 0.0276] \csc b \qquad 3.00 \geq \mu \geq 2.24 \qquad 4a$$

$$-\Delta \log F_\nu(b) = [0.0539\mu - 0.0227] \csc b \qquad 2.24 \geq \mu \geq 1.00 \qquad 4b$$

where b is the galactic latitude.

The error introduced by a mischoice of Δm_{pg} at the poles is easily estimated. The coefficients in the above relation are proportional to Δm_{pg}: Hence the color difference, expressed as the difference in Δm between 3300Å and 10,000Å is similar to $0.9\,\Delta m_{pg}$. That is, if the adopted Δm_{pg} is in error by $0^m.10$, the corrected fluxes will be in error by a similar amount and the color error between $\mu = 3$ and $\mu = 1$ will be about $0^m.09$. The errors will grow proportionally greater as csc b increases.

When the observed fluxes have been corrected for reddening, a small additional correction due to the radial velocity may be applied. If $f(\nu)d\nu$ is the flux emitted at ν in $d\nu$ in the rest frame of the object, and $f'(\nu')d\nu'$ is the flux received by the observer at ν' in $d\nu'$,

corrected for reddening, then we have, via the usual Doppler relation:

$$\nu' = \nu (1-\beta) \qquad 5$$

where $\beta = \frac{V_r}{C}$. V_r is the radial velocity of the source. Thus the flux emitted at ν in $d\nu$ will appear at the lower frequency (for V_r positive) ν' within the smaller bandpass $d\nu'$. That is:

$$f'(\nu')d\nu' = f(\nu)d\nu \qquad 6$$

or

$$f(\nu)d\nu = f'\left[(1-\beta)\nu\right] \quad (1-\beta)d\nu \qquad 7$$

Thus, to obtain the rest-frame distribution of flux, we must multiply the observed flux by $(1-\beta)$ and change the ν'-scale caption from μ' to $(1-\beta)\mu'$. Insofar as the largest β encountered is about 0.02 (NGC1275, NGC7469), the flux is changed by only 2 percent and the principal effect is a shifting of the μ -scale. In Tables 3, the fourth and fifth columns give the rest-frame λ and μ values corresponding to the observer-frame values of the first two columns. The fifth column gives $-\log F_\nu$ in the object's rest frame, the effects of reddening and redshift having been removed. The radial velocities are from Humason, Mayall, and Sandage (1956).

III. PHOTOGRAPHIC SPECTROSCOPY

A. Instrumentation and Techniques

The principal shortcoming of the photoelectric scan data is the lack of wavelength resolution. Since a relatively large bandpass, usually 50Å, was employed in order to obtain a useful signal level, many spectral features of interest were not resolved. For this reason, photographic spectra covering much of the wavelength region of interest were obtained. When properly calibrated by means of the photoelectric observations, these spectra were used to determine relative emission line intensities and profiles. The spectra were obtained over approximately the same time period as the photoelectric observations.

The spectra were obtained at the f/5 Newtonian foci of the 60- and 100-inch telescopes using the Mount Wilson nebular spectrograph ("B" Spectrograph). Virtually all of the spectra were obtained using the 3-inch Schmidt camera. Some spectra were obtained with the 1.5 inch camera but were not used in the present study. For the blue spectral regions, to about 5000Å, the 43B grating (300 lines/mm, blazed at about 4000Å in the second order) was employed yielding a dispersion of approximately 170Å/mm. Some red region spectra, extending to the vicinity of H_α, were obtained at a dispersion of about 120Å/mm with

the 83A grating (300 lines/mm, blazed at third order H_α).

Two principal emulsion types were employed: For wavelengths below about 5000Å, baked IIa-O emulsion was used, all such plates being taken from a single box of this emulsion. Redward, a single box of baked IIa-D plates was used.

While some spectra were not widened, or, rather, widened only by seeing and guiding errors, others were widened by trailing the object along the spectrograph entrance slit which was always oriented in an east-west direction. Such widening was usually over an angular range of from 10 to 30 seconds of arc. The entrance slit width corresponded to approximately one second of arc, indicating that a significant portion of the light of the Seyfert nuclei entered the spectrograph.

Wavelength calibration of the object-spectra was provided by an emission line source, usually a helium lamp, with the comparison spectra being placed on either side of the object spectrum. This comparison spectrum was exposed in two intervals, one preceding and one following the exposure of the object spectrum. This provided a check on slippage of the grating or plate during the exposure.

The intensity calibration of the emulsion was provided by an auxiliary wedge spectrum. These were

obtained using the wedge spectrograph which produces an incident intensity on the emulsion which is proportional to distance perpendicular to the dispersion. The wavelength calibration for these wedge spectra was provided by a helium lamp. In each case, the appropriate wedge plate was cut from the same 4" x 10" plate as the object plate. The wedge spectra were exposed for a time approximately equal to the effective exposure time of the corresponding object spectra, allowance being made for the effects of trailing or widening the latter. Both the object and wedge spectra were developed together in D-76 for 15 minutes at 20°C. Thus the object spectrum and the corresponding wedge spectrum underwent nearly identical exposure and processing. In some instances, more than one wedge spectrum was exposed.

B. Reduction of the Photographic Data

The spectra so obtained were traced with the Caltech microphotometer. From the tracing of the calibration wedge, perpendicular to the dispersion, at fixed wavelength, a set of sixteen parameters defining the relation between incident intensity and the transmission of the emulsion was obtained. (To quite good accuracy, the H and D curves defined by these parameters are relatively independent of wavelength for a given wedge spectrum.) These parameters were used to program an

electronic-analogue device, incorporated in the microphotometer, which converts the measured transmission directly to relative incident intensity units at a given wavelength. That is, this device removes effects due to the non-linear relation between exposure and emulsion density characteristic of the photographic process. The deflection, at each wavelength, on the resultant tracing is then directly proportional to the incident intensity, the constant of proportionality being a wavelength-dependent function representing the instrumental response, emulsion response, and atmospheric transmission. This function is then determined by using the photoelectric scan data to calibrate the spectra (see below).

In tracing the spectra, a knife edge was placed across the object and comparison spectra, oriented approximately perpendicular to the dispersion. This knife-edge produced a reference point, or fiducial deflection, on the tracing of the spectrum. By tracing the comparison spectra at equal distances above and below the point where the object spectrum was traced, and measuring the positions of the known-wavelength comparison lines on the tracing in relation to the knife-edge deflection, a wavelength scale could be placed upon the tracing of the object spectrum. This procedure minimizes the effects of periodic errors in the microphotometer carriage drive screw. Some difficulties were encountered due to irregularities in the

chart drive rate, but were essentially eliminated by a change of recorder. Various trials indicate that the wavelength scales so obtained are accurate to about ±1Å, most of this uncertainty being in the zero point of the scale.

The tracings of the spectra were then calibrated by the scan data. Each bandpass for which a photoelectric flux was available was marked on the tracing and the area between the tracing deflection and the zero-level within this bandpass was determined by planimetry. For reasons discussed below, the area under the continuum was measured for those bandpasses containing emission lines. The function relating these areas to the observed continuum fluxes was tabulated and plotted as a function of wavelength. By interpolation in the resulting tables, (one for each spectrogram), the deflection at a given wavelength on the tracing could be converted directly to monochromatic flux units, the emulsion and instrumental responses, as well as the atmospheric extinction being removed through this procedure. (The resulting response or conversion function should be smooth, and this criterion was used to set the continuum level in regions where extensive line wings, etc. made the estimation of continuum level difficult.)

In the above determination of the response function, the continuum levels were used in order to minimize the consequences of different degrees of widening

of the spectra and the differences between the effective areas of the nuclei observed spectroscopically and photoelectrically. As was mentioned earlier, the relative intensities of the emission lines to the adjacent continuum depend rather critically on the degree of widening of the spectrum or, equivalently, the surface area of the galaxy included in the observations. This is best illustrated in the "worst case" of NGC1068. Figure 3 shows the observed flux distributions obtained with scanner apertures of diameter 8", 14", and 30". The flux in a given emission line remains essentially constant with increase in aperture size, indicating that the line emission arises largely in a region smaller than the smallest aperture used. The continuum fluxes, on the other hand, increase rapidly with increasing aperture sizes. Thus, the flux within a bandpass will increase with aperture. However, to a first approximation, the shape of the continuum does not change significantly with aperture, especially for smaller apertures. Consequently, using the continuum levels to calibrate the spectra should be safe as long as the effective apertures of the photoelectric and spectrophotographic observations are not vastly different. (To the extent that the Seyfert nuclear continuum dominates over the range of effective apertures considered, this approach is strengthened.) The tracings, when so converted to "absolute fluxes" do have a large zero-point uncertainty in the

distribution of log F_λ , but the relative fluxes should be quite good. In any case, the photographic observations were used only to obtain relative fluxes and line intensities.

C. The Determination of Line Intensities and Profiles

The relative line intensities were obtained by planimetry of the microphotometer tracings as corrected by the appropriate response function. For a selected sample of the stronger emission lines, relative intensity profiles were also obtained. The emission line intensities are normalized to an H_β intensity of 10.0 and are listed in Table 5. The absolute flux in a given line is specified by knowledge of the absolute flux in H_β . In Table 5, the relative intensities in parentheses, again normalized to 10.0 for H_β , are those obtained when the assumed reddening law is applied and the galactic extinction removed. The accuracy of these intensities can be estimated from the scatter of measurements obtained from two or more plates. For the stronger lines, the uncertainty is estimated at about 10 percent and the very weakest lines may be uncertain by up to about 50 percent. Lines of particularly large uncertainty, either due to the scatter in measurements or uncertainties in the calibration are indicated by a colon (:) following the intensity. Lack of a relative intensity should not be taken to imply the absence of the line. This is particularly the case in the region between

5000Å and 6000Å and redward of H_α where adequate spectroscopic data were not available in all cases. (The λ5755 line of [NII] and the [OII] lines at λ7319-30 were, in some instances only measured photoelectrically.) To the uncertainties in the relative line intensities must, of course, be added the uncertainties in the photoelectrically derived relative energy distributions. The latter, however, are generally smaller than the photographic uncertainties.

Table 6 gives the observed absolute fluxes in H_β derived in two somewhat different ways: First, the equivalent width of H_β is determined from the spectra and the observed continuum flux level obtained from the photoelectric data is then used to determine the total flux in H_β. In carrying out this calculation, allowance must be made for the differences between the effective areas of integration of the photographic and photoelectric data. That is, the equivalent width will generally decrease and the continuum flux increase as the aperture size, or degree of widening, increases. The two effects do not cancel. The second approach consists of measuring the flux in a 50Å bandpass centered at redshifted H_β, interpolating the continuum contribution from the scan data, and determining the H_β flux. In this instance, the photographic data were used only to determine the fraction of the H_β profile falling outside this 50Å interval. In case of NGC3516, H_β was found to be too weak and ill-defined

to permit an accurate determination by either approach. In this case, the lines of [OIII] at λ4959 and λ5007 (principally the latter) were used as the basis of the absolute line intensity calibration. This was also done for the other objects as a check on the H_β determination.

The "corrected" H_β intensities listed in Table 6 are obtained by correcting the observed values for interstellar reddening, using the assumed reddening law, and multiplying the resultant by $4\pi d^2$, d being the distance, to obtain the total emission at the source. The equivalent widths and H_β fluxes obtained by other authors are listed for comparison purposes. In the particular case of NGC1068, the scatter among the latter is truly remarkable, considering the relatively great strength of H_β and the brightness of the galaxy (the numbers given should be multiplied by the same power of 10 as the adopted value). It is suspected that some of this scatter is due to the aperture effect discussed above.

Relative line profiles, normalized to unit central intensity were also derived. The profiles for some of the brighter emission lines are shown in Figures 4. The estimated uncertainties of the intensity, at half central intensity, are indicated by the vertical arm of the "cross" in each figure. The horizontal arm of this "cross" indicates the estimated velocity resolution, essentially determined by the spectrograph properties, principally the

slit width, and to a lesser extent, by changes in focus quality. This resolution was estimated from the intensity profiles of the intrinsically sharper comparison lines on each plate. The zero of the velocity scale was, in most cases, taken at the intensity maximum. Within the uncertainties, $c\Delta\lambda/\lambda_o$ at the intensity maxima agrees quite well with the published radial velocities.

In determining line intensities and profiles, it was often necessary to separate a composite profile into individual lines. Because of the uncertainties of this separation, the profiles were not always determined to equal distances on either side of the center of the line. While in most instances it would be safe to assume the form of the line profiles in order to affect this separation (e.g. in separating H_γ and [OIII] λ4363, it might be assumed that the H_γ profile was similar to that of H_β, and that of λ4363 similar to those of [OIII] λ4959, λ5007), it was not felt that the quality of the available low-dispersion data justified such a detailed approach. Consequently, the relative contributions of overlapping lines were estimated directly from the tracings, and this procedure usually has little effect on the derived relative intensities. The principal exception to this conclusion is the λ6543 line of [NII] which lies close to broad-winged H_α. The separation, in this case, was affected by assuming that the profile of λ6543 was identical to

that of [NII] λ6583. Insofar as both lines represent transitions between the same levels ($^3P_1$ - $^1D_2$ and $^3P_2$ - $^1D_2$, respectively) this assumption seems reasonable. The observed ratios I(λ6583)/(λ6543) approximate closely the theoretical value of 2.9, indicating that this procedure is probably adequate. Because of this approximation and the quality of the spectra near H_α, detailed profiles for these lines are not given in Figures 4. Generally, the H_α profiles are similar to the H_β profiles, and the profiles of [NII] similar to those of the other forbidden lines.

Representative examples of the spectra of the Seyfert nuclei are reproduced in Figure 5.

IV. THE INTERPRETATION OF THE EMISSION LINE SPECTRA

A. The Emission Line Profiles

The spectra of the Seyfert nuclei reproduced in Figure 5 show the extensive line emission which is characteristic of this group of objects. There is a considerable variation in the number and the relative intensities of these emission lines from object to object. For all but one of these objects, the exception being NGC1068, the emission lines of hydrogen are considerably more extended than are the forbidden lines. The latter feature is more clearly illustrated by the emission-line profiles shown in Figures 4. These emission lines vary somewhat in width from object to object, the variation in the extent of the Balmer profiles being greater than the corresponding variation of the forbidden line widths. Two general properties of the Seyfert spectra should be noted: First, some of the "nuclear" spectra shown in Figure 5 display weak absorption lines, principally CaII H and K. These spectra are all somewhat widened, if only by the "seeing" conditions at the time of observation, and the presence of the absorption lines seems to be a consequence of this widening. If a sequence of spectra are taken of a given object under similar conditions but with differing degrees of widening, the strength of such absorption features as

are present will increase as the amount of widening increases. Spectra taken under conditions of good "seeing" and which are not widened show little or no evidence for absorption lines in the nuclear spectrum, despite the fact that most of the nuclei are not resolved from the surrounding regions even under very good conditions. A second property of the Seyfert spectra is that essentially all of the line emission arises from the Seyfert nucleus, the latter being defined by the presence of the nuclear continuum. In terms of the flux in the continuum, the transition from the "normal" nuclear regions to the Seyfert nucleus is usually quite abrupt.

Some of the emission lines, notably [OII] λ3727 and H_α, occasionally show emission components arising in the "extra-nuclear" region - the region of the nucleus immediately external to the Seyfert nucleus. When present, these components are very much weaker than the nuclear component, generally representing a few percent, or less, of the total emission within a given line. Aside from relative strength, these extra-nuclear components differ from their nuclear counterparts in extent, being considerably narrower, and probably unresolved at the present dispersion. On unwidened spectra, the nuclear line emission generally appears somewhat lens-shaped. The extra-nuclear component, when present, appears as a sharp line superimposed upon the broader nuclear emission.

In these instances, the positions of the sharp components are approximately coincident with the intensity maxima of the nuclear components: The velocity difference is, in any case, much smaller than the velocity dispersion indicated by the profiles of the nuclear emission lines.

The profiles shown in Figures 4 are derived from the measurement of spectra which were widened for photometric purposes. The presence of an extra-nuclear component to a line will, therefore, tend to make the derived profile somewhat sharper in appearance than the "true" nuclear emission profile. However, the relative weakness of the extra-nuclear emission is such that this effect will be negligible in most cases. A partial check on this conclusion was made by comparing the profiles appearing on widened and unwidened spectra. Within the "noise" level set by the emulsion in the latter instance, the importance of the extra-nuclear component is negligible. The profiles of the emission lines given in Figures 4 are, therefore, essentially the nuclear profiles.

Another relatively minor factor affecting the derived intensity profiles is the inclination of the emission lines in some objects. Higher dispersion coudé spectra of NGC1068 and NGC4151 were kindly provided by Dr. J. B. Oke and Dr. O. C. Wilson. These unwidened spectra have higher angular resolution than do those of the present study. Examination of these spectra reveals

that the "lenses" of the emission lines are slightly inclined to the dispersion, this inclination being small in comparison to the extent of the profile and but marginally measureable. Insofar as NGC1068 and NGC4151 are viewed nearly "face on", it seems unlikely that this inclination is due to the rotation of these galaxies. The presence of such inclination will tend to make the derived profiles somewhat broader than the profiles corresponding to the exact centers of the Seyfert nuclei. In practice, however, the effect is utterly negligible in comparison to other sources of error. The presence of this inclination does, however, indicate that the Seyfert nuclei are resolved on these spectra: In the case of NGC4151, the indicated nuclear diameter is very nearly 1" (corresponding to 50 pc.), and, for NGC1068, the diameter is between 1" and 2" with the higher diameter (about 100 pc.) probably being the more accurate.

Within the uncertainties of their determinations, several conclusions may be drawn from the observed emission line profiles. When, as in Figures 4, the intensities are normalized to unit central intensity and the profiles are plotted as Doppler profiles, wavelength being expressed as a velocity with respect to the line center, the profiles of the <u>forbidden</u> emission lines observed in the spectrum of a given object are the same. The profiles shown in Figure 4 represent a fairly wide range of central wavelength

and, consequently, can be interpreted as a velocity dispersion of the emitting gas within the Seyfert nuclei. The line-of-sight velocity distribution, integrated over the emitting volume will then be similar to the line intensity profiles in form. Because of the moderately low wavelength resolution of the present observational material, the relative importance of turbulence and larger-scale mass motions cannot be established. The relative smoothness of the forbidden line profiles in most instances tends to indicate that the velocity dispersion of any larger-scale motions is smaller than that due to turbulence. At the present resolution, only the emission lines of NGC1068 show structure. (The "hump" in the positive-velocity wing of the NGC3227 H_β profile is almost certainly not real.) In this instance, all of the emission lines, including the hydrogen and helium lines, show two distinct maxima separated by approximately 500 km/sec. This indicates the presence of at least two emitting regions with a relative velocity of at least 500 km/sec. The estimated internal velocity dispersions of the two components observed are roughly comparable and somewhat in excess of their relative line-of-sight velocity. Physical conditions within the two "clouds" are somewhat different as is indicated by the variations in the relative intensities of the two maxima from line to line.

In their analysis of the kinematic structure of NGC1275, Burbidge and Burbidge (1965) noted that some of the emission lines, notably H_α , appeared doubled with the two components being rather widely separated and the redder component being the fainter and much narrower of the two. The present data do not clearly show this weaker feature. Partly, the [NII] λ6543 emission and the low resolution are responsible. The spectra of Burbidge and Burbidge were also much more strongly exposed than are those of the present study: The spectra showing the doubled H_α emission also show the extra-nuclear components of H_α and [NII] quite clearly, whereas the present spectra do not. More detailed kinematic studies of some of the Seyfert nuclei have been made by Walker (1968a, 1968b). These spectroscopic studies reveal the presence of three or four discrete clouds within 5" of the center of the nucleus of NGC1068 and of at least two such clouds within about 2" of the center of the nucleus of NGC4151. The dimensions indicated are somewhat larger than those found above. The relative velocity dispersion of these clouds along the line of sight are smaller than the velocity dispersions within the individual components. Reversals in some of the emission lines of NGC7469, observable at higher dispersions, indicate somewhat similar motions. It would seem, therefore, that the Seyfert nuclei can be pictured as being composed of one or more

clouds with large internal velocities or turbulence. The smoothness of the forbidden line profiles indicates that these internal turbulent velocities are at least comparable to the relative velocities of the clouds. The similarities of the Doppler profiles of the forbidden lines indicate that these profiles are the consequence of such mass motions and/or turbulence.

Dibai and Pronik (1968) have noted a tendency for the [OIII] and [NeIII] line profiles to show a faint winglike structure of small extent which is absent from the profiles of the [OII] and [SII] lines. This structure, or "base", contains less than a few percent of the total flux of the [OIII] and [NeIII] lines in most of the objects examined. Three objects show such a structure of considerably greater strength. At the present level of accuracy, the extent of this "base" is rather poorly defined, especially when this feature is weak, largely as a consequence of the uncertainties involved in defining the continuum level on the tracings of the spectra. This is particularly the case for the [OIII] λ4959 and λ5007 emission for which the profiles were largely determined from spectra on IIa-O emulsion in which the response is changing rapidly in this wavelength region.

The nuclear emission of NGC1068 is exceptional in that the Balmer and forbidden line profiles are similar. In the other Seyfert nuclei examined, the hydrogen lines

are much more extended than are the forbidden lines. With the exception of NGC3516 (and NGC1068), the Balmer lines are composed of a relatively sharp core plus extensive and featureless "wings" which may extend from 2500 km/sec to over 5000 km/sec from the line center. The profiles of the cores of these hydrogen lines are essentially identical to the profiles of the forbidden lines. In addition, a "base" which is present in the [OIII] and [NeIII] lines will also be found in the Balmer line profiles. Because of continuum-level uncertainties and the presence of nearby emission lines, the extent of the Balmer wings cannot be determined to very high accuracy. However, these wings usually contain most of the total Balmer line flux. Within the uncertainties of the determination, the profiles of these wings are symmetrical about the line center and approximately the same for all Balmer lines observed. Unfortunately, the uncertainties are quite large, most of the hydrogen lines having neighboring emission lines of considerable strength. Only H_β is in a region relatively free of emission lines: H_α is straddled by the [NII] emission and H_γ is immediately adjacent to [OIII] λ4363. The higher series members are considerably fainter and well-defined profiles, particularly in the wings, could usually not be obtained. Since the separation of composite profiles introduces additional uncertainties, the Balmer profile of greatest accuracy is

that of H_β .

The only permitted lines observed, other than the Balmer lines of hydrogen, were λ4686 of HeII, λ5876 of HeI and, possibly, λ3444 of OIII. Generally, only λ4686 was of sufficient strength to permit an estimation of the profile. Unfortunately, this line is rather poorly located for these purposes, the real or suspected presence of [FeIII] λ4659 and [ArIV] λ4711, λ4740 making a separation of the composite profile rather difficult. Furthermore, the curvature of the emulsion response in this region makes the continuum level rather uncertain. Consequently, this profile was not measured in any case except that of NGC1068. In this instance, the profile was similar to the Balmer and forbidden-line profiles. For the other objects in which HeIIλ4686 was observed, the width of the profile was estimated and found to be somewhat broader than the forbidden lines, but narrower than the Balmer lines. A wing structure rather similar to that present in the Balmer lines, but of lesser extent and relative intensity, seems to be present.

The group properties of the emission lines found in each object are summarized in Table 7. The approximate maximum widths ΔV_C , ΔV_B , and ΔV_W of the core, base, and wings, respectively, are expressed in velocity units about the line center. The quantities f_C , f_B , and f_W are the approximate fractions of the total line flux within each

of the components. The values given in this table should be regarded as approximate.

The Balmer profiles of NGC3516 do not show a core similar in profile to that of the forbidden lines as is the case in the other objects. The profile of H_β, in particular, appears quite featureless. Andrillat (1968) has noted differences in the appearance of H_β in comparing spectra obtained in 1967 with the tracing of H_β published by Seyfert (1943). The reported variation consists of a decrease in the central intensity of H_β relative to the central intensities of the nearby [OIII] lines over this time interval. Because of the unknown effects of aperture or widening variations discussed earlier, and since no clear plate level was indicated for the tracing given by Seyfert, the original spectra of NGC3516 were secured from the Mount Wilson plate files and retraced. Comparison of the 1943 spectra with the current data indicates that the reported variation of H_β is almost certainly real. However, the relative intensities of the forbidden lines and their profiles do not seem to have changed significantly over this 25 year interval. It is further noted that on neither the 1943 spectra nor on the 1966-67 spectra does the H_β profile show a core resembling the forbidden lines in profile. Because H_β is extremely weak relative to the continua of all spectra examined, particularly on the more recent

plates, the measured equivalent width, central intensity, and the derived profile, are all extremely sensitive to the continuum level adopted. With these uncertainties present, the derived H_β data, particularly the line profile, should be regarded as rather approximate. The uncertainties in the corresponding data for the higher series members are significantly higher. In Figure 4e, the rather large uncertainties in the H_β profile are indicated by the error bar. The corresponding errors or uncertainties for the H_γ and H_δ profiles are larger by factors of about two, and the rather good agreement among these Balmer profiles should be regarded as completely fortuitous. It is of interest that the H_α profile shows some indication of a core, although this core and [NII] λ6543 are barely resolved and the former is comparable in intensity to the noise level on the plates. In any case, such a core probably contains less than 15 percent of the Balmer line flux. For most of the Seyfert nuclei, the cores of the hydrogen lines contain about 20 percent of the total flux of the line. Because of the weakness of H_β relative to the continuum in the spectra of NGC3516, the "absence" of a core might well be a consequence of the quality of the observations only: It is estimated that a core possessing the profile of the forbidden lines and containing 15 percent of the H_β flux is essentially at the limit of detectability on the presently available spectra. The limit of detect-

ability on the 1943 spectra is somewhat lower because of the greater central intensity of H_β but uncertainties in the calibration for these earlier spectra are present (see below). Hence, the presence of a core containing 15 percent, or less, of the flux cannot be disproved by the present data. Some indication of a core is present in the rather crude H_α profile. The presence of [NII] λ6543, however, makes this indication rather uncertain.

Within the rather large uncertainties, the appearances of the 1943 and 1966-1967 H_β profiles for NGC3516 are quite similar. However, the more recent profile seems to be some 2000 km/sec greater in extent. This apparent increase in width largely compensates for the decrease in central intensity with the result that the equivalent width of H_β relative to the equivalent widths of the [OIII] lines cannot be said to have changed significantly over this 25 year interval. There is also some rather weak evidence that the continuum level has changed over this period of time: Seyfert (1943) estimated that approximately 5 percent of the nuclear light of NGC3516 was present in the emission lines, whereas the present data indicates a figure of about 1 percent or less. The relative contrast of lines to continuum on similarly widened plates does seem to have declined somewhat. While this change is consistent with an increase of the continuum radiation since 1943, the

difficulties involved in comparing observations made under rather disparate conditions would make such a conclusion rather speculative. For instance, the 1943 and 1966-67 observations were made using different spectrographs and the spectra were widened to slightly different degrees. The latter differences are, however, rather small and tracings of the sharper comparison lines on the spectra indicate that the spectrograph resolutions were approximately the same in both instances. Another complicating factor is the unknown effect of 25 years of aging on Seyfert's spectra. This is probably rather small since retracings of the original plates resemble, fairly closely, the tracings shown by Seyfert (1943, Figure 1). In considering these sources of uncertainty, it is felt that a detailed specification of the nature of the variation of the H_β profile is virtually impossible. It can, however, be stated that H_β has decreased in central intensity relative to the [OIII] lines, that the relative strengths and profiles of the forbidden lines have not changed significantly, and that the relative equivalent widths of the emission lines, including H_β, have probably not altered. There are rather weak indications of a variation in continuum intensity.

The profiles of the forbidden lines can be most consistently interpreted in terms of macroscopic mass

motions and/or turbulence occurring within the Seyfert nuclei. The structure observed in the emission lines of NGC1068, together with the results of the more detailed kinematical studies of NGC1068 and NGC4151 by Walker (1968a, 1968b) and of NGC1275 by Burbidge and Burbidge (1965), provides strong additional evidence for such an interpretation. Only in the instance of NGC1068, however, can the kinematical properties indicated by the forbidden line profiles be used to explain the observed hydrogen and helium line profiles. In the spectrum of NGC1068, the permitted and forbidden lines have essentially identical profiles (cf. Figure 4a) and display the same structure. This indicates that the forbidden and permitted lines are formed in the same regions. For the remaining seven Seyfert nuclei under consideration, only the cores of the recombination line profiles can be interpreted in this manner. The similarity between the profiles of these cores and those of the forbidden lines implies that at least part of the hydrogen and helium line emission arises in the regions producing the forbidden line spectrum. (We are assuming the presence of such cores in the Balmer profiles of NGC3516. For the reasons discussed above, we make no assumptions regarding the relative strength of these cores other than noting that they represent less than about 20 percent of the Balmer-line flux.) The principal problem, then, is to provide an interpretation

or explanation for the presence of extensive wings in the profiles of the Balmer lines and HeIIλ4686.

Since a kinematical interpretation seems quite satisfactory in explaining the profiles of the forbidden lines and those of the cores of the recombination lines, a similar interpretation of the wing-profiles might be attempted. However, if we postulate that the wing emission arises from a region distinct from the forbidden-line region and characterized by larger turbulent velocities and/or mass motions, some means must be found of suppressing the forbidden line emission. Since the forbidden line profiles in no instance show extensive wings, the forbidden line emission arising from this high-turbulence region must be essentially non-existent. Woltjer (1959), in interpreting Seyfert's observational material, postulated such a turbulent region in which the temperature was sufficiently lower than that of the forbidden line region to account for the absence of the forbidden line wings. The high frequency radiation field was also assumed to be diluted, or weaker, in this region. The temperature difference required between the "hot" and "cold" regions is not extremely large as can be seen from the following approximate consideration: For the typical Seyfert nucleus, the ratio of the flux in the core of the Balmer lines to that in the wings is approximately 1:4. The intensity of H_β arising from a volume

V characterized by proton density n_+, electron density n_e and electron temperature $t = 10^{-4}T_e$ is proportional to $n_e n_+ \cdot V\, Q(t)$, where $Q(t)$ is tabulated by Pengelly (1964). Designating parameters of the cooler, more turbulent region by primed symbols and those of the hotter regions producing the observed forbidden line emission by unprimed quantities, we can write

$$\frac{n_e' \, n_+' \, V'}{n_e \, n_+ \, V} = \frac{I_\beta'}{I_\beta} \frac{Q(t)}{Q(t')} \approx \frac{1}{4} \frac{Q(t)}{Q(t')} \qquad \text{(Case B)}$$

where I_β and I_β' are the total fluxes of H_β in each component. In the limit of low densities, the population of the initial level of a forbidden line transition to the ground-level is proportional to $n_o n_e t^{-1/2} \exp(-\frac{\chi}{kt})$ where n_o is the population of the ground level, $\chi = 10^{-4} h\nu/k$, and ν is the frequency of the emitted line. The intensity of the forbidden line emission in the cooler, more turbulent, region, I', will be related to the intensity, I, of the forbidden line "core" by the relation

$$\frac{I'}{I} \approx \frac{1}{4} \frac{Q(t)}{Q(t')} \left(\frac{t}{t'}\right)^{1/2} \exp.\chi \left(\frac{1}{t} - \frac{1}{t'}\right) \qquad \text{(low density)}$$

Typically, the forbidden line intensities indicate $t \approx 2$. If we assume $t' \approx 1$ we have, approximately:

$$\frac{I'}{I} \approx 0.2 \exp\left(-\frac{\chi}{2}\right)$$

For the forbidden lines observed $\chi \approx 2$ to 4. Consequently, forbidden line transitions to the ground state will be weaker by at least an order of magnitude in the 10,000°K region in comparison to the emission in the 20,000°K region and, since the emission from the cooler region is distributed over a much broader profile, it can be presumed undetectable. The assumption of low density in the forbidden line region is fairly adequate as is indicated by the temperatures and densities derived in the following section. The assumption that $n'_o/n'_+ \approx n_o/n_+$ is fairly valid for the ions NII (I.P. = 14.6eV), SII (10.3eV), OII (13.6eV). The major difficulty with this approach is the presence of wings on the HeIIλ4686 profile. Since the ionization potential of Helium I is about 24.5eV, we would expect the relative abundance of HeII with respect to HI to be considerably lower in the cooler region than in the forbidden-line region, with the absence of λ4686 wings a consequence. While these wings may be weaker than the Balmer wings, they are not significantly so. Consequently, some other means must be found to suppress the forbidden-line emission in the postulated region of higher velocity dispersion.

Oke and Sargent (1968) have pointed out that a very high electron density will effectively suppress the forbidden line emission by collisional deexcitation. In the limit of high density, the relative populations of the levels approach their equilibrium values: In the high velocity region we would have an initial-level population proportional to $n_o' \exp(-\chi/t')$ instead of $n_o' n_e' t'^{-1/2} \exp(-\chi/t')$. The relative forbidden-line emission from the two regions will then be proportional to $t^{1/2}/n_e'$ if the temperatures are similar. The constant of proportionality depends upon the relevant atomic parameters, such as the "collision strengths" and spontaneous transition probabilities. For $t \approx 2$, the electron density required to adequately suppress the forbidden emission for the strongest lines observed is $n_e' \gtrsim 10^7$. This should be compared to the densities found in the forbidden line region which are typically $n_e \sim 10^4$ cm^{-3}.

If the source of the emission in the wings of the hydrogen and helium lines is, in fact, a distinct region characterized by a large internal velocity distribution, the observed spectra should display certain characteristic features. Most obvious is that relative Doppler profile of the emission wings, obtained by dividing the intensity profile by the total flux for each wing system, should be the same for all of the hydrogen and helium lines.

Examination of the profiles of Figures 4 suggests that this might be the case. However, the wing profiles of most of the hydrogen lines are rather uncertain because of the presence of neighboring emission lines and/or the uncertainties present in the determination of the continuum levels on tracings of the spectra. It has been noted that HeIIλ4686 seems narrower than the profile of H_β in most cases but this indication is a rather weak one for the reasons discussed above. On the basis of the presently available spectra, in any case, the Doppler profiles of the Balmer line wings show differences which are generally smaller than the estimated uncertainties of their determination. The present data are, then, consistent with a kinematical model for the wing emission insofar as the profiles are concerned. If such a region is made up of a fairly small number of discrete clouds, possessing internal velocity dispersions comparable to those indicated by the forbidden line profiles, we might expect to see structure in the emission wings. Since such structure is not apparent from the present data, and since the wing profiles are smooth and essentially symmetrical, the number of such clouds must be large. A simpler interpretation is that the wings are formed in a single region characterized by a high internal velocity distribution resulting from turbulence. If the kinematical model is applicable to the wing emitting

region, some instances might be found in which the Balmer wings are systematically shifted in velocity from the emission cores. Such an instance is not indicated by the present data, however.

The relative smoothness of the wing profiles, their symmetry, and the absence of any clear instances of a velocity shift between core and wing might also be taken as rather circumstantial evidence against the kinematical origin of the Balmer wings. The suggestion that the HeII profiles are systematically less extended than the Balmer lines might also be so taken. A source of line broadening which is also consistent with some of the observed properties of the profiles is electron scattering. Oke and Sargent (1968) have suggested such a mechanism for the Balmer and HeII wings in their analysis of the spectrum of NGC4151. The advantage of electron scattering in this context is that it obviates the need to postulate the existence of a separate region for the wing-emission, the presence of very large velocity dispersions, and physical conditions (e.g. high n_e or low T_e) which are markedly different from those which apply in the regions producing the observed forbidden line emission. Such an interpretation will also be consistent with the observed smoothness and relative symmetry of the wing profiles. The problem of the forbidden line "wings" is still present, but in a somewhat different form. The

optical depth for electron scattering is given by:

$$\tau_e = n_e \sigma_e S$$

where $\sigma_e = 6.65 \times 10^{-25} cm^2$ is the Thomson scattering cross-section, and $n_e S = \int n_e dS$ where the integration is along the geometrical path of the photons of interest. As a first approximation, we can take S to be the effective diameter of the emitting region as defined by the recombination and forbidden spectra. In the following chapter (cf. IV-B), the quantity $\mathcal{E} = n_e^2 V$ is obtained either from the intensity of $H\beta$, the amplitude of the Balmer jump in emission, or both (cf. Table 10). From the forbidden line intensity data, the electron density n_e can be roughly estimated (cf. IV-B and Figures 6). We then have:

$$(n_e S)_{eff} \approx (2 n_e \mathcal{E})^{1/3}$$

for which values ranging from $1 \times 10^{23} cm^{-2}$ to $8 \times 10^{23} cm^{-2}$ are obtained. We can then compute τ_e. The derived values for τ_e cover the interval 0.05 to 0.55, with the mean for eight Seyfert nuclei being about $\overline{\tau}_e \approx 0.25$. Considering the uncertainties in the values of $\mathcal{E}$ and n_e, particularly the latter, and the assumptions implicit in writing the above equation for $(n_e S)_{eff}$, the possibility of significant optical depth due to electron scattering cannot be eliminated. However, a factor of 100 error, or

uncertainty, in n_e will result in an uncertainty less than a factor of five in τ_e, so this optical depth is almost certainly less than 3 or 4, and probably less than unity.

Münch (1948) has computed the profile of scattered radiation $\Delta(\tau_1,\alpha)$ for incident monochromatic light of frequency ν_o in terms of the parameters $\tau_1 = \tau_e$ and $\alpha = \left(\frac{mc^2}{4kT_e}\right)^{1/2} \frac{\nu - \nu_o}{\nu_o}$. The emergent profile has an intensity distribution of the form:

$$I(\alpha) = I_o(\alpha) e^{-\tau_1\sqrt{3}} + \int_{-\infty}^{+\infty} I_o(\alpha') \Delta(\tau_1, \alpha - \alpha') d\alpha'$$

where $I_o(\alpha)$ is the initial profile. If it is assumed that the initial profile $I_o(\alpha)$ had the form of the forbidden-line and Balmer core profiles, we can integrate this expression over all α. The term on the left will become W_t, the total flux in the line. On the right, the first term will be W_c, the flux in the core, and the second term will be the flux in the wings, W_w. If there are no losses from the radiation within a given line, we will have:

$$W_t = \int I_o(\alpha) d\alpha$$

hence

$$W_c/W_t = \exp(-\tau_1\sqrt{3})$$

Since the wing and core components of the Balmer lines in the Seyfert nuclei contain flux in the ratio of approximately 4:1, we find that $\tau_1 \approx 0.9$ for the Balmer lines is required to produce the observed partitioning of flux. This is roughly comparable to the above estimate of τ_e. For the stronger forbidden lines to show no wings, the optical depth due to scattering must be considerably smaller. If we say the line wings are "absent" if they contain less than 10 percent of the line flux, we must have $W_c/W_t > 0.9$ or $\tau_1 < 0.06$ which is also not greatly in conflict with the τ_e estimated above. It is of interest to note that the "bases" observed in some of the forbidden line profiles contain only a few percent of the total line flux in most instances and, furthermore, are usually detectable only for the stronger lines, suggesting that electron scattering may be responsible. The present data are not of sufficient accuracy to investigate this question more carefully.

Rather rough calculations of the scattering profiles expected for $T_e = 2 \times 10^4 °K$ and $\tau_1 = 0.9$ have been performed assuming the initial profile is the Doppler profile shown by the forbidden emission lines. The quantities $\Delta(\tau_1, \alpha)$ were obtained from the table given by Münch (1948). Comparison of those observed profiles for which $f_w/f_c \approx 4$ with the computed profiles reveals no discrepancies of significance. The uncertainties in

the observed wing profiles, however, become rather significant for large v and, consequently, this agreement should not be taken to indicate that electron scattering is the only possible broadening mechanism.

The principal difficulty, as in the kinematical model, is the suppression of the forbidden line wings. As is indicated by the above considerations, $\tau_1 \approx 1$ is required to explain the partitioning of flux between core and wing in the Balmer lines, whereas $\tau_1 < 0.06$ is required in order that similar wings do not appear in the forbidden line profiles. The only way in which both of these conditions can be satisfied is to require that the geometrical distance traversed by the Balmer line quanta be 20 or more times greater than that of the forbidden line quanta. The cause for such a difference could be atomic scattering, which would increase the Balmer line effective path length but have essentially no effect on the forbidden line photons. The possibility of significant optical depth in the Balmer lines is discussed in the final section of this chapter (cf. IV-C).

If electron scattering is the relevant mechanism for forming the Balmer wings, we can make the following approximate consideration: If the diffusion of Balmer quanta out of the emitting region can be treated as a "random walk" process, and if we neglect the effect of electron scattering as a first approximation, the effective

path length S_{n2}, and therefore the optical depth for electron scattering τ_{n2}, will be proportional to $Q_{n2}^{1/2}$ for a Balmer photon of frequency ν_{n2}. The quantity Q_{n2} is the number of scatterings undergone by the quanta ν_{n2} before escape. Since Q_{n2} will be inversely proportional to the photon's mean-free-path, it will be directly proportional to the oscillator strength f_{n2}. We will have, therefore $\tau_{n2} \propto S_{n2} \propto Q_{n2}^{1/2} \propto f_{n2}^{1/2}$. Consider, then, a case in which the effective optical depth in $H\beta$, τ_{n4}, due to electron scattering is unity. We will then obtain $\tau_{n2} = 2.32$, 1.00, 0.61, and 0.43 for $n = 3$, 4, 5, and 6, respectively, if we use the f_{n2} values given by Aller (1963, p.166). Oke and Sargent (1968), in their analysis of NGC4151, found that the cores of the Balmer lines contained about 9.5 percent, 18 percent, 27 percent, and 72 percent of the total line fluxes of $H\alpha$, $H\beta$, $H\gamma$, and $H\delta$, respectively. The corresponding optical depths are $\tau_{n2} = 1.36$, 0.99, 0.76, and 0.19 for $n = 3$, 4, 5, and 6. The discrepancies are probably not significant in that we have neglected the effect of scatterings by electrons which shift the photon out of the line: Since the optical depth τ_{n2} decreases with n, the lower energy quanta will be more frequently scattered out of the line by the free electrons. The result will be to significantly decrease τ_{32} while having relatively little effect on the depths for higher n.

We have also ignored losses in the higher series, e.g. we have assumed that an absorbed H_β quantum will be simply scattered although a certain fraction will be emitted as Paschen α (plus $H\alpha$), the Paschen quanta escaping from the emission region. At least the direction of the τ_{n2} dependence is the same as in the "observed" case.

In view of the smooth profiles observed, the electron scattering model is somewhat more attractive in that no separate, high-velocity and high-density region need be postulated. The electron scattering model is also, perhaps, indicated by the symmetry of the Balmer wings about the Balmer core. If no evidences of systematic velocity shifts between core and wing, or of structure in the Doppler profiles of the latter, are observed, it is suggested that the electron scattering mechanism is more appropriate. An observational determination of the validity of this electron scattering model can be made for objects in which structure is present in the forbidden line cores: If the Balmer wings are extensive, and are formed by electron scattering of an initial profile which has the form of the forbidden line profiles, the structure in the core of the Balmer lines will be "washed out" or absent. Insofar as only the lines of NGC1068 show such structure on the available spectra, this question cannot be more closely examined.

B. Physical Conditions in the Seyfert Nuclei

The emission lines found in the Seyfert nuclei are quite similar in type and relative intensity to those observed in the spectra of planetary nebulae, the principal difference being the much greater line widths encountered in the former. In terms of line strengths, the major difference is the much steeper Balmer decrements found in some of the Seyfert spectra. Insofar as the relative intensities of the forbidden lines are similar, we expect the conditions of electron temperature and density in the Seyfert nuclei to be roughly comparable to those in planetary nebulae. That is, to a first approximation we have $T_e \sim 10^4 °K$, $n_e \sim 10^4 cm^{-3}$ for the Seyfert nuclei. This assumes that the forbidden lines are excited by electron impact as in planetary nebulae and that the electron energy distribution can be characterized by T_e. Under these circumstances, we can relate the relative intensities of certain lines arising from a given ion to n_e and T_e in the usual fashion if the relevant atomic parameters are known. The atomic parameters consist of the spontaneous transition probabilities Aij and the "collision strengths" Ωij for the levels and transitions of interest. In deriving the relations below, we have used the values of Aij and Ωij as summarized by Boyarchuk, et. al. (1963). In the usual notation, we let $t = 10^{-4} T_e$ and $X = 10^{-4} n_e t^{-1/2}$ and the relations

obtained are:

for OIII :

$$\frac{I(\lambda 4959)+I(\lambda 5007)}{I(\lambda 4363)} = \frac{7.1}{\epsilon}\,\frac{1+0.12\epsilon+4.1\times10^{-4}(1.0.11\epsilon)X}{1+3.8\times10^{-2}(1+0.10\epsilon)X}$$

where $\epsilon = \exp(-3.30/t)$,

For NII :

$$\frac{I(\lambda 6548)+I(\lambda 6584)}{I(\lambda 5755)} = \frac{6.3}{\epsilon}\,\frac{1+0.14\epsilon+6.3\times10^{-4}(1+0.88\epsilon)X}{1+0.24(1+0.88\ )X}$$

where $\epsilon = \exp(-2.50/t)$,

For OII :

$$\frac{I(\lambda 3727)+I(\lambda 3729)}{I(\lambda 7320)+I(\lambda 7330)} = \frac{5.5}{\epsilon}\,\frac{1+0.36\epsilon+5.3(1+0.82\epsilon+0.16\epsilon^2)X}{1+13.8(1+0.38\epsilon)X+38.4(1+0.78\epsilon+0.15\epsilon^2)X^2}$$

where $\epsilon = \exp(-1.96/t)$,

and for SII :

$$\frac{I(\lambda 6717)+I(\lambda 6730)}{I(\lambda 4068)+I(\lambda 4076)} = \frac{13.4}{\epsilon}\,\frac{1+0.14\epsilon+0.17(1+6.79\epsilon+0.05\epsilon^2)X}{1+7.30(1+0.33\epsilon)X+0.98(1+6.47\epsilon+1.15\epsilon^2)X^2}$$

where $\epsilon = \exp(-1.39/t)$.

The relative intensities of the pairs of lines appearing in the numerators and denominators of the above expressions, e.g. $I(\lambda 3727)/I(\lambda 3729)$, could have been related

to n_e and T_e in order to obtain additional useful expressions. This has not been done in the present instance for one of two reasons: Either the dependence of the ratio on n_e and T_e is extremely insensitive to variations in these quantities, for the range of conditions of interest (e.g. I(λ6548)/I(λ6584)), or the temperature-density dependence is significant but the relevant lines, because of their proximity and the widths of their profiles, are not well resolved at the present dispersion (e.g. I(λ7320)/I(λ7330)).

The relations given for the [SII] and [OII] intensities should be regarded as approximate and applied with caution. In the cases of [OIII] and [NII] we have assumed that the fine-structure levels ^3P_J, J = 0, 1, 2, of the ground state are populated according to the ratios of their respective statistical weights; i.e. in proportion to $g_J = 2J + 1$. For the temperature-intensity range of interest, this is a fairly good approximation, and OIII and NII can be treated adequately as three-level systems in deriving the [OIII] and [NII] intensity relations. This approximation will not, in general, be suitable for the levels of OII and SII: These ions have been treated as five-level systems. While the above approximation is fairly adequate when applied to the $^2P_{1/2}$ and $^2P_{3/2}$ upper level, it is considerably in error when applied to the $^2D_{5/2}$ and $^2D_{3/2}$ levels. The spontaneous transition

probabilities for transitions from the upper and lower ^2D levels differ by about an order of magnitude for both OII and SII. Hence the sum of the intensities of the two lines resulting from these transitions (λ3726, λ3729 of [OII] , λ6717, λ6730 of [SII] , respectively) will depend critically on the relative populations of the initial levels. The level populations are determined essentially by the equilibrium between radiative and collisionally induced transitions. The $^2D_{5/2}$ and $^2D_{3/2}$ populations, in particular, are a rather critical function of the collision strength $\Omega(^2D_{5/2} - {}^2D_{3/2})$ which is not known. The collision strengths between fine structure levels of <u>different</u> terms are known. Seaton and Osterbrock (1957) have assumed $\Omega(^2D_{5/2} - {}^2D_{3/2})$ can be approximated by $\Omega(^2D_{5/2} - {}^2P_{3/2})$, and $\Omega(^2P_{3/2} - {}^2P_{1/2})$ by $\Omega(^2D_{3/2} - {}^2P_{1/2})$. This approximation is based upon the fact that the collision strengths between fine structure levels of <u>two given terms</u> are proportional to the product of the statistical weights of the initial and final levels, and consists of the assumption that the same "constant" of proportionality can be applied to transitions between fine structure levels of a <u>single given term</u>. This assumption does not seem to have a clear justification (<u>cf</u>. Naqvi and Talwar, 1967). It is of interest to note that if this approximation is applied to the SII collision strengths, the resultant relation predicts electron densities several orders of magnitude

higher than does the [OII] relation when used with the observed line-intensity data. Because of this problem, together with the uncertainties in the "known" Ω_{ij} for SII , $\Omega(^2D_{5/2} - ^2D_{3/2})$ and $\Omega(^2P_{3/2} - ^2P_{1/2})$ have been assumed zero in deriving the [SII] relation. Little weight should be given to the $n_e(T_e)$ relations derived using this expression. The [OII] relation was derived using the "approximate" values for the collision strengths, and, for the reasons cited above, should also be regarded as approximate. This situation is particularly unfortunate in that the [OII] and [SII] lines are the best density indicators available in the present observations.

For each object the ratios, R, of the relevant line intensities are obtained. Using the above relations, we can solve for the electron density-temperature relations for each ion, i.e. $n_e = n_e(T_e, R)$. The results of this procedure are shown in Figures 6. The low-weight [SII] relations are shown as dashed curves. In many instances, only an upper limit could be placed upon part of the line intensity data. This was most frequently the case for the [NII] relation: λ5755 was rather frequently too weak to be detected. In these instances, an upper limit for the $n_e(T_e)$ relation was obtained. The true values of n_e and T_e will lie at lower n_e and/or T_e than those values defined by the dashed curve in these cases. The intensity

ratios were formed using the reddening corrected relative line intensities given in Table 5. Little difference results from using the observed intensities, the differences in the intensity ratios being comparable to, or smaller than, the uncertainties in the line intensity data.

The values of n_e and T_e obtained by application of the intensity relations to the observed intensities are weighted means of n_e and T_e in the emitting regions. Since the Seyfert nuclei will be optically thin in the forbidden lines, the true intensity ratios will be the integral of the right-hand sides of the intensity relations over the emitting volume. If n_e and T_e vary significantly throughout this volume, the effective values of n_e and T_e obtained from the observations will be different for different ions. That is, the $n_e(T_e)$ relations for all ions will have a common (n_e,T_e) solution only if n_e and T_e are quite uniform throughout the region. Since it is anticipated that this will not be the case, it can only be hoped that the variations will be relatively small.

An examination of the $n_e(T_e)$ relations shown in Figures 6 suggests that the assumption of uniformity is probably a poor one. In particular, it is noted that the observed [OIII] and [NII] intensity ratios yield a common (n_e,T_e) solution in only one instance. (Solutions at negative n_e and/or T_e being ignored.) The [NII] data generally define a curve lying at lower (n_e,T_e) than does

the [OIII] data. This implies that the [NII] lines are formed in a region which is systematically cooler, less dense, or both. A second possibility is that the atomic data for either NII or OIII are in error, or that the observations are systematically in error. Indirect evidence that the atomic data are not grossly incorrect is provided by the generally good agreement between the (n_e, T_e) defined by the [NII] intensities and the values obtained from the [OIII] , [OI] and [OII] intensities in planetary nebulae (cf. Seaton 1960). The uncertainties in the line intensities, on the other hand, are too small to account for the discrepancies. A possible source of observational error does exist for the [SII] and [OII] lines. The blue lines were measured on spectra calibrated by the photoelectric data but the red lines were measured only photoelectrically and the intensities may be not strictly comparable. However, it is believed that the discrepancies between the [OII] data and the [SII] data arise largely in consequence of the uncertainties in the collision strengths and the approximations discussed above.

The forbidden-line intensities are generally insufficient to specify accurate values of electron density and temperature, partly because of lack of sufficient observational information. An approximate method of obtaining $n_e(T_e)$ relations from the intensities of single forbidden lines relative to H_β has been discussed by Boyarchuk,

et. al. (1963) . This method requires several additional assumptions in its application which were not felt justifiable in the present instance. The greatest uncertainty is in the electron density determination in the present instance,although the likelihood of stratification of the emitting region introduces temperature uncertainties as well. The adopted mean (n_e,T_e) values are indicated in Figures 6. Additional temperature-density information can be obtained from the Balmer recombination spectra. This is discussed in a later section (cf. V-B).

C. The Balmer Decrement

A rather characteristic feature of the spectra of the Seyfert nuclei is the rather steep Balmer decrement. The relative intensities of the Balmer lines, normalized to an H_β intensity of unity, are given in Table 8. These relative intensities have been corrected for reddening using the adopted reddening law. For most of the objects of the present study, the effect of this correction on the relative intensities is rather small as can be seen by comparing the corrected intensities to the observed relative intensities: The latter are the quantities within parentheses in Table 8. For comparison purposes, the theoretical Balmer decrements computed by Seaton (1960) for the Baker-Menzel Cases A and B are also tabulated: The parenthesized values for Cases A and B are those obtained with allowance being

made for orbital (l) degeneracy. In Figure 7 are plotted the decrements for the Seyfert nuclei and for Cases A and B. The latter are the values for an assumed temperature of 2×10^4°K. For clarity, the relative intensities have been re-normalized to unit intensity for H_α in this figure.

Consideration of Table 8 or Figure 7 reveals that the greatest discrepancies between the observed and theoretical values occur in the H_α/H_β ratios, in the sense that the theoretical computations yield too low a value for this ratio. The intensities, relative to H_β, of the higher series members are in considerably better agreement with the theoretical values, although significant discrepancies are present.

The sense of deviations, particularly in the H_α/H_β ratio, suggests that differential extinction be considered as a possible cause. That is, that there exists significant reddening within the nuclear regions of the Seyfert galaxies and/or the assumed reddening law for our own galaxy is incorrect. In considering the latter possibility, two factors are of importance; the form of the reddening law, which we have taken to be that determined by the observations of Whitford (1958), and the positional dependence of the scaling factor, which we have assumed to obey a csc b law scaled to the Hubble (1934) value of $\Delta m_{pg} = 0^m.25$ at the galactic poles. Hubble's observations

indicate that a csc b dependence for Δm_{pg} is adequate to quite low galactic latitudes. If we assume that the wavelength dependence of the extinction has the same form, not necessarily the adopted form, everywhere within the relevant regions of our galaxy, we should expect to find a correlation between, say, the $H\alpha/H\beta$ ratio and galactic latitude. Such a correlation does not seem to exist: NGC1275, at quite low latitude (csc b $\approx$ 4.4) has a relatively low $H\alpha/H\beta$ ratio whereas the two objects with the highest ratios, NGC3227 and NGC1068, are at relatively high latitudes (csc b $\approx$ 1.2 and 1.3, respectively). Furthermore, there is strong reason to believe that the form of the reddening law is not dissimilar to the Whitford relation insofar as we expect most of the reddening to occur in the vicinity of the galactic plane (by virtue of the greater density of obscuring material at lower z-distances), and the form in the vicinity of the plane is that determined observationally by Whitford. If, despite the conclusion of Hubble, we adopt the Whitford form for the extinction law but discard the assumption of a more-or-less smooth csc b dependence of the extinction, we encounter further difficulties. If the normal form of the extinction curve is scaled for each object so as to bring the observed and theoretical $H\alpha/H\beta$ ratios into agreement, the relative intensities of the higher series members, i.e. $H\gamma/H\beta$ and $H\delta/H\beta$, become much greater than the theoretical ratio. In Figure 8 are

plotted the values of log H_α/H_β and log H_β/H_γ obtained using the assumed extinction law. The solid curve in the lower part of the figure represents the reddening curve for the Whitford relation. Addition of obscuring material, obeying the Whitford form for wavelength dependence, will cause the observed points to move rightward and downward, paralleling the reddening curve, relative to their "true" positions. As can be seen from this figure, no such parallel motion will bring the observations into agreement with the theoretical values (with the possible exception of points D and F corresponding to NGC1275 and NGC3516). That is, forcing the agreement of the observed and theoretical H_α/H_β ratios by scaling the adopted form of the reddening law will yield agreement between the corrected and theoretical log H_β/H_γ ratios in only one instance, will yield too high a ratio in six instances, and too low a value in one instance. In view of the above, it seems implausible that the observed Balmer decrements are manifestations of the extinction occurring within our own galaxy.

The possibility of reddening within the environs of the Seyfert nuclei is somewhat more difficult to absolve from responsibility. To the extent that the Seyfert galaxies, aside from their nuclei, seem to have normal structure and stellar composition, one might, as a first approximation, assume that the obscuring material is

similar in nature to that within our own galaxy. Under such an assumption, the same difficulty encountered above in explaining both the H_α/H_β and the H_β/H_γ ratios will again be met. Insofar as the conditions in the nuclear regions of the Seyfert galaxies are decidedly different from those in the solar neighborhood, the assumption of a similar reddening law will be difficult to justify. If it is assumed that the Balmer decrements of the source of line-emission are identical to the theoretical values, the form of the internal reddening curve can be computed. Such curves will be quite unusual in form, being relatively flat from the bluest observed Balmer line through H_β but dropping abruptly in absorption in the region between H_β and H_α. For objects such as NGC1068 or NGC3227, this decline in absorption must amount to 1.5 to 2 magnitudes.

Under ideal conditions, there are means whereby the internal reddening of these objects could be determined. If we assume that the effects of reddening within our own galaxy can be adequately removed either by using the assumed extinction law or by other means (such as the observation of more normal objects within the same cluster of galaxies, as could be done in the case of the low-latitude Perseus cluster for NGC1275), and if the electron density and temperature is fairly uniform throughout the emitting region, the forbidden lines can be used to specify the reddening occurring within the object. To the extent

that the relevant atomic parameters, particularly the collision strengths, are well known, the ratios of the intensities of the forbidden lines arising from a given ion can be used to specify a relation $f(n_e,T_e) = 0$. If a number of such ratios are available, and if no differential reddening is present, all such relations should have a single solution. If such is not the case, an amount of differential reddening between the lines forming the relevant ratios can be specified so as to bring the $f(n_e,T_e) = 0$ into agreement at a single (n_e,T_e) point. By an iterative procedure, and by requiring the extinction law to be a monotonic function of frequency, the extinction law could be specified. This procedure has two shortcomings: First, the assumption of uniformity of n_e and T_e is required. This does not seem justified, particularly for those objects in which there are indications of differences among the forbidden line profiles. The second difficulty is the lack of atomic data, particularly the Ω_{ij}, and the absence of sufficient well-determined line intensity ratios to adequately carry out the above procedures. Until further observational data are available for these objects, particularly in the infrared and ultraviolet, the possibility of internal reddening being the cause of the observed anomalous Balmer decrement cannot be rejected. However the peculiar forms required to produce such an effect, and the rather large variations from object to object suggests that such

reddening is probably not the principal cause. If the region can be assumed optically thin in the Balmer line radiation arising from the transition $n \rightarrow 2$, and if the corresponding Paschen line $n \rightarrow 3$, is observed the differential reddening between these two wavelengths, λ_{n2} and λ_{n3}, respectively, can be determined since $I(\lambda_{n2})/I(\lambda_{n3}) = \lambda_{n3}A_{n2}/\lambda_{n2}A_{n3}$, independent of the true nature of the decrement or the mechanism by which the n = 2 level is populated. Deviation of the observed ratio of intensities from this calculated ratio can be interpreted directly as a consequence of reddening if it can be shown that the assumption regarding the optical depth in the Balmer lines is correct. The present observations, however, do not include the Paschen lines.

If reddening is rejected as an important factor, we are forced to conclude that the Balmer decrements are intrinsically very steep and that the conditions in the emitting regions are such as to render the idealized Baker-Menzel cases inapplicable. It should be pointed out that anomalous Balmer decrements are not unique to Seyfert nuclei: In a diagram such as Figure 8, many planetary nebulae would lie to the left and above the points corresponding to cases A andB while others would be found in various other parts of the figure (cf. Osterbrock, 1964, Fig. 1,and Aller and Liller, 1968, Fig. 3). When corrected for reddening, however, most planetary nebulae have H_α / H_β

ratios in fair agreement with the theoretical (Case B) values for the appropriate temperature. Large intrinsic H_α/H_β ratios are, however, found in the spectra of some novae. For example, a ratio of 5 or 6 was observed in the spectrum of Nova Lacertae 1936 and a value of ten or twelve observed in RS Ophiuchi 1933 (Ambartsumian, 1958). For these objects the phenomenon can be interpreted as a manifestation of significant optical thickness of the Balmer Series (as well as of the Lyman lines) in the expanding shell, which is presumably transparent in higher series. As is observed, the n = 2 population should decrease as the shell expands and the excitation decreases, resulting in smaller depth in the Balmer lines and a consequent tendency for the decrement to drop to more "reasonable" values. In planetary nebulae, on the other hand, the optical depth in the Balmer lines is generally less than unity (cf. Seaton 1960). The physical conditions in the Seyfert nuclei are, in some respects, quite similar to those in planetary nebulae; i.e. $T \sim 10^4 °K$, $n_e \sim 10^4 cm^{-3}$. However, the diameters of planetary nebulae are generally of the order of 10^{17}cm whereas the effective diameters of the Seyfert nuclei are typically 10^{19}cm. Although these dimensions are quite uncertain, the observed Balmer decrements suggest that the possibility of significant optical depth in the Balmer lines be investigated.

Obviously, if the region is optically thick to

Balmer quanta, all such quanta will be degraded to $H\alpha$ which will be essentially the only line observed. At the other extreme, a region thin in the Balmer lines should produce a decrement approximating the appropriate Case B values (It is assumed, in both cases, that the region is optically thick to Lyman quanta.). For an intermediate case in which the trapping of $Ly\alpha$ quanta is adequate to populate the n = 2 level to the point where the optical depth in $H\beta$ is approximately unity, there will be appreciable degradation of $H\beta$ quanta to $H\alpha$. Insofar as the absorption cross-sections decrease very rapidly with increasing quantum number, n, the higher Balmer lines will be relatively unaffected. The principal consequences, then, will be an increase in $H\alpha$, and a decrease in the $H\beta$ intensity.

An estimate of the optical depths in the Balmer lines can be made following the procedure of Osterbrock (1964). We shall assume a temperature of $T_e = 2 \times 10^4 °K$. First, the populations of the n = 2 level, designated n(2s) and n(2p) must be estimated. The 2s level is populated by captures, including captures to higher levels which are followed by radiative transitions eventually ending at the 2s-level, and is depopulated by collisionally-induced transitions to the 2p-level and by two-photon transitions to the 1s ground level. If we let $\alpha(2s)$ designate the effective recombination coefficient to the

2s level, we can write the steady-state equation:

$$n_e n_+ \alpha(2s) \cong n(2s) \left[A_{2s1s} + n_+ W_p(2s \rightarrow 2p) + n_e W_e(2s \rightarrow 2p) \right]$$

where n_+ and n_e are, respectively, the ion (proton) and electron densities, A_{2s1s} is the two-photon transition probability with value 8.227 sec^{-1} (Spitzer and Greenstein, 1951), and W_p and W_e are the collisional deexcitation coefficients for proton and electron collisions respectively. The latter quantities are tabulated by Seaton (1955a).

The 2p-level is populated by captures and collisionally-induced transitions from the 2s-level. Depopulation is by emission of Ly α quanta. Only those Ly α quanta which escape from the nebular region produce a net decrease in the 2p-population. If the average Ly α quantum is scattered Q times before such escape, the rate of depopulation of 2p is $n(2p)A_{2p1s}/Q$ where $A_{2p1s} = 6.25 \times 10^8$ sec^{-1} (Bethe and Salpeter 1957, Capriotti 1964). In the steady-state:

$$n_e n_+ \alpha(2p) + n(2s) \left[n_+ W_p(2s \rightarrow 2p) + n_e W_e(2s \rightarrow 2p) \right] = n(2p) A_{2p1s}/Q$$

Typically $n_+ \approx 0.85 n_e$ for Seyfert nuclei (see the discussion of the recombination continuum: V-B). So, to adequate accuracy, we can write:

$$n_+ W_p(2s\rightarrow 2p) + n_e W_e(2s\rightarrow 2p) = n_e W^*(2s\rightarrow 2p)$$

where

$$W^* = W_e + 0.85\ W_p \text{ at } T_e = 2\times10^4 {}^\circ K \ ,$$

we have, from Seaton's (1955a) tables,

$$W^*(2s\rightarrow 2p) = 4.07 \times 10^{-4} cm^3\ sec^{-1} \ .$$

From Seaton's (1960) Table 4, we find that $\alpha(2p) \approx 0.63\ \alpha_B$ and $\alpha(2s) \approx 0.37\ \alpha_B$ where $\alpha_B = 1.43 \times 10^{-13}\ cm^3\ sec^{-1}$ is the total effective recombination coefficient for the n = 2 level. Inserting known quantities in the above expressions, and solving for the level populations yields:

$$n(2s) \approx 5.5 \times 10^{-15}\ n_e^2\ (1 + 5\times10^{-5}\ n_e)^{-1}$$

$$\approx 3.7 \times 10^{-15}\ n_e^2 \quad , \quad \text{for } n_e \sim 10^4$$

and

$$n(2p) \approx 1.2 \times 10^{-22}\ n_e^2 \left[1+2.9\times10^{-5} n_e (1+5\times10^{-5} n_e)^{-1}\right] Q$$

$$\approx 1.5 \times 10^{-22}\ n_e^2\ Q \ , \quad \text{for } n_e \sim 10^4 \ .$$

For present purposes, the approximations for $n_e \sim 10^4$ are of adequate accuracy. The optical depth in H_β is given by:

$$\tau_\beta = \tau(2,4) = \tau(2p,4s)+\tau(2p,4d)+\tau(2s,4p)$$

$$= n(2p)\left[K_o(2p,4s)+ K_o(2p,4d)\right] S + n(2s) K_o(2s,4p) S$$

where S is the geometrical thickness (cm) of the emitting region and the K_o are the central line absorption coefficients. From Osterbrock (1964) we have $K_o(2s,4p) = 5.8 \times 10^{-12} T_e^{-1/2}$ and $K_o(2p,4s) + K_o(2p,4d) = 7.0 \times 10^{-12} T_e^{-1/2}$. If we use these values, we obtain

$$\tau_\beta \approx 1.5 \times 10^{-28} [\, 1+5\times10^{-8} Q] \, n_e^2 S$$

The central line absorption coefficients used are obtained by assuming the absorption profile is defined by the velocity distribution of the hydrogen atoms. This, in turn, is determined by the temperature. For $T = 2 \times 10^4 °K$ the "half-width" (i.e. the <u>total</u> width at half central intensity) in velocity units is about 30 km/sec. The emission lines of the Seyfert nuclei, however, have half-widths of approximately 600 km/sec. Assuming, as seems reasonable, that the neutral hydrogen atoms have the same velocity distribution as the protons giving rise to the emission spectrum, we have overestimated the K_o by a factor of approximately twenty. With this correction, we have:

$$\tau_\beta \approx 7.5 \times 10^{-30} [1+5\times10^{-8} Q] \, n_e^2 \, S \quad .$$

A similar treatment yields the total optical depth in the center of H_α :

$$\tau_\alpha \approx 4.3 \times 10^{-29} \left[1+7\times10^{-8}Q\right] n_e^2 S \quad .$$

An estimation of τ_β now requires only a value for Q and for $n_e^2 S$. The electron density, n_e, can be estimated from the forbidden line data (cf. Figures 4). The diameter S can be estimated from the quantity $\mathcal{E} = n_e^2 V$, which is obtained either from the observed amplitude of the Balmer jump or from the observed $H\beta$ flux (cf. Table 10). This quantity is derived for the objects of interest in a later section of this thesis. We then have $n_e^2 S \approx \left[2n_e^4 \mathcal{E}\right]^{1/3}$ where the uncertainty is essentially the uncertainty of $n_e^{4/3}$ since $\mathcal{E}$ is more accurately specified than n_e.

Ignoring for the moment, the contribution to τ_β arising from the 2p-population we can write

$$\tau_\beta \geq 7.2 \times 10^{-30} n_e^2 S \quad .$$

A weak condition for $\tau_\beta \geq 1$ is then that $n_e^2 S \geq 10^{29}$. Computing $n_e^2 S$ from the observational data for the objects of interest, we find that this weak condition is satisfied by NGC1275, NGC4151, NGC5548 and NGC7469. NGC4051 nearly satisfies the condition. Unfortunately, NGC1068 and NGC3227 which have the greatest $H\alpha/H\beta$ ratios do not satisfy this condition. NGC3516, which also does not satisfy this condition, has a Balmer decrement deviating only slightly from the theoretical values.

The failure of NGC1068 and NGC3227 to satisfy this $\tau_\beta \gtrsim 1$ condition implies either that there is not significant optical depth in H_β, in which case we must look elsewhere for the reason for the observed Balmer decrements, or that the above condition is too weak. Obviously, if the appropriate Q is significantly greater than about 10^8, the optical depth will increase greatly. In order that $\tau_\beta \gtrsim 1$ for NGC1068 and NGC3227 values of Q greater than about 6×10^8 and 4×10^9, respectively, are required. For planetary nebulae, values of 10^6 or 10^7 are usually quoted (Aller and Liller 1968, Osterbrock 1964). Such values are obviously inadequate in the present context. To a first approximation, an upper limit to Q can be obtained by assuming the Ly α scatterings to be perfectly coherent (Ambartsumian, 1933). The number of scatterings before escape will then be proportional to S^2 (assuming the conditions are everywhere uniform: more specifically, that $n(1s)\,K_o(1s,2p)$ is constant throughout the volume). Insofar as the typical dimensions of Seyfert nuclei seem to be roughly 100 times those of planetary nebulae, and insofar as the conditions are similar, we might estimate $Q \sim 10^{10}$ to 10^{11} as an upper limit. This should be divided by about 20, as before, to account for the broader absorption coefficient profile. Values of $Q \sim 10^{10}$ would be more than adequate to produce significant optical depth in H_β.

Another means of increasing τ_β is to postulate an HI region surrounding the HII region in which the recombination emission arises. O'Dell (1965) has presented evidence for the existence of such HI regions surrounding planetary nebulae. This neutral-hydrogen region could "back scatter" a significant fraction of Lyα quanta, resulting in a net increase of the effective value of Q. If such an HI region were present, observable manifestations of its existence might include the presence of reversals in the Balmer line profiles. Since these reversals would not be present in the forbidden line profiles, it would be possible to distinguish them from "reversals" due to the relative motions of emitting clouds (as in the case of NGC1068). Asymmetries in the Balmer-line cores which are absent from the forbidden-line profiles might be a manifestation of the presence of an HI region or of significant optical depth in the HII region. The present spectroscopic data are of inadequate resolution and quality to investigate this problem. Attention is however directed to the continuous energy distributions of NGC1068, NGC1275, NGC7469 (Figures 1a, 1b and 1j) which show a slight depression blueward of the Hα + [NII] emission.

Capriotti (1964) has carried out calculations of the Balmer decrements for nebular shells of inner radius R_1 and outer radius R_2. For models such as these, the decrement is specified by two parameters; $R = R_1/R_2$ and

τ_α (corresponding to a geometrical thickness of $2\,[R_2 - R_1]$). In Figure 7 we have plotted, as dashed lines, the results of Capriotti for $R = 0$, $T_e = 2 \times 10^{-4}$°K: For values of τ_α of 25, 63, 125, and 250, the $H\alpha\,/H_\beta$ ratio increases rapidly with optical depth, the higher series ratios varying more slowly. (Capriotti's $\tau_\alpha = 1$ calculation essentially coincides with the Case B decrement.) It can be seen from this figure that the value of τ_α which best reproduces the observed $H\alpha\,/H_\beta$ ratio generally predicts intensities of $H\gamma$ and H_δ higher than those observed. Shown in Figure 8 are the $H\alpha\,/H_\beta$ - $H\gamma\,/H_\beta$ relations for the objects observed and for Capriotti's calculations, which more clearly illustrate this discrepancy. The observed points, with a single exception, fall below the curve defined by the calculations of Capriotti.

Parker (1964) has calculated Balmer decrements for the case of collisional excitation. In Figure 7 we have plotted the decrement obtained by Parker for $T_e = 2 \times 10^4$°K and optical thickness in the Lyman lines. (Under these conditions Parker obtains $N(HI)/N(HII) \approx 0.078$.) The collisional decrement is steeper than the self-absorption decrement for higher series members. This is further illustrated in Figure 8. The collisional calculations define a downward sloping curve whereas the self-absorption calculations define an upward sloping curve. (The close

agreement between the former and the reddening curve is coincidental.) All but one of the observed points lie above the collisional curve.

It seems clear that the observed Balmer decrements cannot be explained in terms of either a purely collisional or a purely radiative model, even if the effects of self-absorption are included in the latter. Hopefully, a combination of the two would give agreement with the observations of a given object. There seem to remain a number of difficulties in regard to the theoretical aspects of the Balmer decrement problem: It is not clear, for example, how points lying to the left of cases A and B in Figure 8 could be interpreted in terms of any combination of these collisional and radiative calculations. Planetary nebulae are observed with decrements lying within this region or outside of the extremes defined by the radiative and collisional calculations (cf. Osterbrock 1964, Fig. 1; Aller and Liller 1968, Fig. 3). It seems likely, therefore, that there are some rather severe theoretical shortcomings.

In connection with the properties of the Seyfert nuclei, it should be noted that calculations for the radiative cases customarily assume (cf. Baker and Menzel, 1937) that the only radiation available for atomic excitation lies beyond the Lyman limit. While this is a reasonable assumption for planetary nebulae, where the

radiation source is an exciting star and the Lyman radiation is severely depleted at any significant distance from this star, it may not be a reasonable assumption for Seyfert nuclei. The radiation source in these nuclei might be the ultraviolet non-thermal flux arising from a source extensively distributed throughout the region.

There exists an observational means of determining whether there is, in fact, any significant amount of neutral hydrogen within the line-emission region needed to produce the optical depth in H_β for the radiative self-absorption cases. Since OI and HI have approximately the same ionization potential (13.550 and 13.527 eV, respectively) the presence of the [OI] lines at λ6300 and λ6364 would imply the existence of neutral hydrogen. These lines do appear in the spectra of five of the Seyfert nuclei with measurable strength and may be present in the remaining objects. However, the strongest evidence for the presence of neutral hydrogen in the regions where the emission lines are formed is the absence or weakness of the permitted OIII λ3444 line in the Seyfert spectra (cf. VI-A).

V. THE CONTINUOUS SPECTRA

A. The Properties of the Observed Continua

If the spectra and energy distributions of the Seyfert nuclei (Figures 1) are compared to those of the nucleus of a normal spiral (Figure 2), a number of distinctions become apparent. The most obvious of these differences is the presence, in the Seyfert spectra, of many bright emission lines similar in some respects to those found in planetary nebulae. This emission is both stronger and more extensive than the weak emission occasionally encountered in normal spiral galaxies. In addition to the forbidden-line and Balmer-line emission, a noticeable Balmer jump in emission is present in some instances; the merging of the higher Balmer lines tending to produce a gradual increase in intensity from about $\lambda 4000$ to the Balmer jump, partially masking the latter.

The Seyfert nuclei also differ from normal nuclei in the properties of the observed continuum. The continuous energy distribution of a normal nucleus curves downward when plotted as in Figures 1 and 2. A rather pronounced feature is the abrupt drop in the flux distribution blueward of $\mu \sim 2.3$ due, in part, to the presence of G-band absorption. Other prominent features of the energy distribution of a normal nucleus include the absorption due to MgI in the

green and the strong absorption lines of CaII. These features are extremely weak in, or absent from, the energy distributions of the Seyfert nuclei: In particular, the Seyfert nuclei show little if any indication of an abrupt decrease in flux to the blue of $\mu \sim 2.3$. In the wavelength region for which energy distributions have been obtained, the continuous energy distributions of the Seyfert nuclei are considerably flatter than those of normal nuclei. In some cases, the observed continuous energy distributions approximate an exponential function of frequency quite accurately. If the energy distribution of a Seyfert nucleus and a normal nucleus are forced to coincide in the red region of the spectrum, say at about 8000Å, the differences in the continua increase rather rapidly to the blue, the Seyfert nucleus being the brighter. It is this phenomenon which is responsible for the unusually blue colors observed for these objects.

The absence, or weakness, of the G-type absorption spectrum expected in a spiral nucleus indicates that the principal source of the observed flux must be other than the distribution of stellar types found in normal nuclei. The excess flux in the blue (and infrared) lends further weight to this conclusion. With regard to the absorption spectrum, the possibility should be considered that this spectrum is, in fact, present but is masked by the extensive emission spectrum. A brief consideration shows that

this can hardly be the case: For instance, the possibility that the CaII H-line at λ3968 would, if present, be totally or partially concealed by the emission lines Hε at λ3970 and [NeIII] λ3968 is quite good insofar as these emission lines are generally quite broad. However, the K-line would be relatively unaffected, the nearest observed emission lines being [NeIII] λ3869, λ3968 and the hydrogen lines Hε λ3970 and Hζ λ3889. The widths observed in these emission-line profiles indicate that the effect of the [NeIII] lines would be completely negligible. The hydrogen lines, while having wings which may extend to the vicinity of CaIIK in some objects, are far too weak at this point to have any significant masking effect. The G-band at λ ≈ 4300 is an extremely prominent feature in normal spectra: In the Seyfert spectra this G-band would, in most instances, be affected by the presence of Hγ λ4340. However, if this absorption feature were present in any significant fraction of its usual strength, the observed emission strength in the wings of Hγ would be inadequate to significantly affect its depth. In any case, a rather marked asymmetry in the Hγ profile would be expected. This is not the case, insofar as the blue and red wings of Hγ appear reasonably symmetrical about the line center. The determination of the redward half of this profile is somewhat complicated by the presence of [OIII] λ4363, but this difficulty can be largely circumvented by comparing the blue halves of the

H_γ and H_β profiles. Within the uncertainties of the profile determinations, there is no significant difference between the emission profiles of H_γ and H_β and we conclude that the G-band is, at best, present in only a very small fraction of its normal strength. It therefore seems reasonable to conclude that the energy distributions of the Seyfert nuclei, at least blueward of about λ4300, arise in part from some source other than a distribution of stellar types such as is found in the nuclei of normal spirals.

The spiral galaxies NGC4258 (M108) and NGC6814 both appear on Seyfert's (1943) list of "suspected Seyfert galaxies". Both have been rejected as members of this group on the basis that they did not adequately fit the criteria established by Seyfert for the objects which he examined in detail (Burbidge, Burbidge, and Prendergast, 1963). In particular, the emission spectrum of NGC4258 is considerably weaker than that of the Seyfert nuclei, only λ3727 and H_α being of significant strength. The emission lines present are also quite narrow ($\lesssim$400 km/sec). In addition, the absorption spectrum of NGC4258 appears normal for a spiral, although perhaps slightly weak, and seems to extend through the nuclear region. The emission lines of NGC6814 are somewhat broader than those of NGC4258, but still narrower than those encountered in the Seyfert nuclei. On the basis of the rather poor-

quality spectra available, absorption seems to be present in the nucleus of this object. The continuous energy distributions of NGC4258 and NGC6814 are shown in Figures 1g and 1j, respectively. It seems clear that these resemble that of the normal nucleus much more closely than do the Seyfert nuclei. On this basis alone, these two objects should probably not be classified as Seyfert galaxies. A word of caution is in order with respect to this conclusion as applied to NGC6814: This face-on spiral does have a rather sharp nucleus but the surrounding nuclear regions are quite bright and the "extra-nuclear contamination" may be significant.

The weakness or absence of the G-type absorption spectrum in the Seyfert nuclei can be interpreted in three different ways: The first possibility is that the observed spectra are the consequence of the presence of a rather abnormal distribution of stellar types within the nuclei. The absorption spectrum of this population would have to be characterized by a great weakness of the G-type absorption lines, and the absence of other prominent absorption features as well. The only real possibility in this regard would be an early-type population , the prominent hydrogen absorption lines being concealed by the corresponding Balmer emission lines. However, the observed energy distributions of the Seyfert nuclei would be rather difficult to explain in terms of such a population.

The observational evidence, on the other hand, indicates that the stellar population which <u>is</u> present in the Seyfert nuclei is of fairly normal type: First, spectra which include the extra-nuclear regions show a fairly normal G-type spectrum in the regions adjacent to the Seyfert nuclei (A possible exception is NGC1275 which shows a somewhat earlier spectrum.). Second, observations have been made of NGC1068 with a series of circular apertures, all centered on the Seyfert nucleus. The continuous energy distributions obtained with aperture diameters of 8", 14", and 30" are shown in Figure 3. (One second of arc corresponds to about 50 parsecs at the adopted distance of approximately 10 Mpc.) By subtracting these distributions from one another, the energy distributions of annular regions centered on the Seyfert nuclei can be obtained. In comparing these energy distributions to that of the normal spiral nucleus it is found that, within the observational uncertainties, the energy distributions of these annuli are of the same form as that for a normal nucleus. (A further factor noted is that these annuli show no significant line emission, indicating that such emission arises within 4" of the nuclear center. This was, in any case, known from the spectra.) Assuming that the nuclear stellar population is abnormal, therefore, raises the necessity of postulating a rather abrupt change in the stellar-type distribution at the "boundary" of the

Seyfert nucleus and does not significantly assist in explaining the continuum energy distribution observed. We conclude, therefore, that the best approximation is to assume that the stellar population is normal for a spiral galaxy. The energy distribution remains unexplained as does the absence of significant G-type absorption.

A second possibility is that the normal absorption spectrum is, in fact, present but so broadened by motions as to be undetectable. Considering the strengths of these absorption features present in the spectrum of a normal nucleus, the velocity dispersions required would be considerably in excess of that indicated by the broadest emission lines in the Seyfert spectra. The velocity dispersion required to significantly affect the appearance of the continuous energy distribution would have to be several orders of magnitude higher than is observed. In stating that the extra-nuclear spectrum appears "normal", only the equivalent widths of the usual G-type absorption features were considered: In fact, the lines of this spectrum are usually somewhat wider than is normally the case. (In NGC7469, in particular, the absorption is quite broad, the estimated width of the K-line being comparable to the width of the forbidden emission lines.) The exact profiles were not determined since the extra-nuclear spectra which appeared were generally quite underexposed. However, the H and K lines have widths which appear to be

only slightly narrower than those of the narrowest emission lines observed. This would tend to indicate that the velocity dispersion of both stars and gas varies smoothly across the boundary of the Seyfert nucleus. Hence the velocity dispersion within the nucleus is inadequate to explain the weakness of the absorption lines. If the "external spectrum" is extrapolated into the nucleus, it seems clear that this absorption spectrum will be almost completely swamped by the nuclear continuum if the latter contains no additional absorption. It also seems clear that a large difference in the velocity dispersions of stars and gas should not be considered a likely possibility.

The simplest and most likely explanation is that a significant fraction of the nuclear luminosities of these objects arises from a source other than a normal, or abnormal, stellar component. The general properties required of the energy distribution of such a source can be roughly estimated: First, the flux due to this source, or sources, must be large enough to significantly mask the absorption features of the stellar component. Secondly, the flux of this source in the blue (and infrared) must be adequate to explain the observed flux excess(es). Finally, this energy distribution must be essentially continuous, containing no absorption features of significant strength.

An obvious choice for at least part of this additional continuous spectrum is the hydrogen recombination radiation.

The presence of the forbidden emission lines, in strengths comparable to those in planetary nebulae, strongly indicates the presence of a gaseous component and of conditions within this gas roughly comparable to those in planetary nebulae. The Balmer lines also appear in emission and we consequently expect continuous free-bound recombination radiation to be present. That this is the case is indicated by the presence of a jump in emission at the location of the Balmer jump in some objects. For the temperature range of interest, this recombination continuum has some of the desired properties, in that it might account for the excess of flux observed in the blue regions and the weakness of the absorption lines arising from the stellar component. We therefore shall consider the properties of this component in somewhat greater detail.

B. The Recombination Continuum

The emission of the gaseous component in the forbidden and recombination lines can be determined directly from the observational material. The uncertainties in the line intensity determinations arise largely as a consequence of the difficulty of clearly defining the continuum level on the tracings of the spectra and the inherent uncertainties of the photographic process. The former source of uncertainty is largely confined to very weak lines and the wings of the Balmer lines. The

uncertainties in the specification of the continuum distributions of flux are much smaller than those of the individual line intensities largely as a consequence of the relative smoothness of the continuous energy distribution. By utilizing both the photographic and photoelectric data, the energy distribution in the continuum is quite well determined over most of the wavelength region for which observations are available.

The portion of this continuum energy distribution arising from free-bound recombination cannot be determined directly from the observed distribution insofar as the contribution of at least one other component, the stellar population, is not known. This recombination contribution can, however, be calculated if certain parameters are observationally determinable. Since these calculations make no allowance for the effects of interstellar reddening, they must be referred to the reddening-corrected observed fluxes. The parameters required to specify the recombination contribution must be similarly corrected and the relatively minor effects of radial velocity are also assumed to have been removed.

The observed continuous recombination flux arising from a volume V, at a distance d, will be given by:

$$r(\mu)d\mu = \frac{h d\mu}{4\pi d^2} \int_V n_e\, n_+ \gamma(\mu, n_e, T_e)\, dV \qquad (8)$$

where h is Planck's constant, n_e is the electron density, n_+ is the density of the ions producing the recombination flux, T_e is the electron temperature, and $\gamma(\mu, n_e, T_e)$ is the effective recombination coefficient ($cm^3\ sec^{-1}$) for the ions. As before, μ (microns^{-1}) = $3.34 \times 10^{-15} \nu$ (sec^{-1}). The integration is over the emitting volume. For reasonably normal abundances, only the ions of hydrogen and helium will be significant producers of recombination radiation. As an adequate approximation, we can then write:

$$n_+ \gamma(\mu, n_e, T_e) \cong \tag{9}$$

$$n(H^+)\,\gamma(H^\circ) + n(H^+)\,\gamma(2q) + n(He^+)\,\gamma(He^\circ) + n(He^{++})\,\gamma(He^+)$$

and

$$n_e = n(H^+) + n(He^+) + 2n(He^{++}) \tag{10}$$

The frequency and temperature dependence of $\gamma(H^\circ)$, $\gamma(He^\circ)$, and $\gamma(He^+)$, the effective recombination coefficients for the corresponding ions, is not explicitly indicated. These coefficients are, to a good approximation, independent of electron density. The n's are the ionic number densities (cm^{-3}). The two-photon recombination coefficient for hydrogen, $\gamma(2q)$, is dependent upon n_e as well as upon μ and T_e. This dependence of $\gamma(2q)$ on the electron density can be approximated by the following expression

due to Seaton (1955a):

$$\gamma(2q) = \frac{\gamma_o(2q)}{1+n_e \frac{W^*}{A_{2q}}} \qquad (11)$$

where $A_{2q} = 8.227\ \text{sec}^{-1}$ (Spitzer and Greenstein, 1951) is the two-photon recombination coefficient and W^* is the collisional deexcitation coefficient for proton and electron collisions. The latter quantity can be obtained from the tables of W_e and W_p given by Seaton (1955b). With $n(H^+)/n_e \cong 0.85$ (see below) we have $W^* \cong W_e + 0.85W_p$, and obtain:

$$\gamma(2q) = \begin{cases} \dfrac{\gamma_o(2q)}{1+5.6\times10^{-5}n_e} & \text{for } T_e \cong 1\times10^4\,^\circ\text{K} \\ \dfrac{\gamma_o(2q)}{1+5.0\times10^{-5}n_e} & \text{for } T_e \cong 2\times10^4\,^\circ\text{K} \end{cases} \qquad (12)$$

where the quantity $\gamma_o(2a)$ depends only upon μ and T_e. (The value of W^*/A_{2q} can be interpolated from Seaton's tables for other temperatures, but this is hardly of value since the estimated uncertainty in W^* is about ± 20 percent.)

We define the auxiliary quantities ζ and γ_E by:

$$\zeta^{-1} = \frac{n_e}{n(H^+)} = 1 + \frac{n(He^+)}{n(H^+)} + 2\,\frac{n(He^{++})}{n(H^+)} \qquad 0 \leq \zeta \leq 1 \qquad (13)$$

and

$$\gamma_E(\mu, n_e, T_e) = \gamma(H^o) + \gamma(2q) + \frac{n(He^+)}{n(He^+)}\gamma(He^o) + \frac{n(He^{++})}{n(H^+)}\gamma(He^+) \tag{14}$$

We can then rewrite equation (8) as:

$$r(\mu)d\mu = \frac{h d\mu}{4\pi d^2} \int_V \zeta n_e^2 \gamma_E(\mu, n_e, T_e) dV \quad . \tag{15}$$

Insofar as we have no means of determining the nature of the variation of the integrand throughout the emitting volume, we shall assume that the region can be characterized by appropriate mean values of ζ, n_e^2, and γ_E. We therefore approximate equation (15) by:

$$r(\mu)d\mu = \frac{h d\mu}{4\pi d^2} n_e^2 V \zeta \gamma_E(\mu, n_e, T_e) \quad . \tag{16}$$

In order to compute the flux, $r(\mu)$, by equation (16) we must determine γ_E, $n_e^2 V$, and ζ. Computation of the first and last of these quantities requires knowledge of the relative abundances of the helium ions which may be determined from the relative intensities of $H\beta$ λ4861, HeIλ5876, and HeIIλ4686. We can write:

$$\frac{n(He^+)}{n(H^+)} = \frac{5876}{4861} \frac{I(\lambda 5876)}{I(\lambda 4861)} \frac{\alpha_{4,2}(H^o)}{\alpha_{3^3D,2^3P}(He^o)} \tag{17}$$

and (17) Cont.

$$\frac{n(He^{++})}{n(He^{+})} = \frac{4686}{4861}\,\frac{I(\lambda 4686)}{I(\lambda 4861)}\,\frac{\alpha_{4,2}(H^{o})}{\alpha_{4,3}(He^{+})}$$

where the α's are the effective recombination coefficients for the transitions indicated. These coefficients as a function of temperature can be obtained from Seaton's (1960) Table 8 and Equation 2.32. Table 9 gives the observed intensity ratios and the computed helium abundances for the Seyfert nuclei. It is assumed that Baker-Menzel "Case B" is applicable, and the assumed temperature was 2×10^{4}°K. No significant change in the derived abundances would have resulted from choices of T_e as low as 1×10^{4}°K or as high as 3×10^{4}°K. The individually computed values as well as the mean values for the Seyfert nuclei, may be compared to the helium abundances in planetary nebulae: For eight planetary nebulae listed by Osterbrock (1964), the mean values are: $N(He^{+})/n(H^{+}) = 0.12 \pm 0.04$ and $n(He^{++})/n(H^{+}) = 0.03 \pm 0.03$. The helium ion abundances of the Seyfert nuclei are, therefore, not significantly different from the abundances in planetary nebulae. In calculating the recombination continua for those Seyfert nuclei for which the relevant helium line intensity data are not available, the mean values for the planetary nebulae have been assumed. The values for these abundances are not critically important: Considering the γ -values

for the relevant ions, a factor of two error in the helium abundances will result in an error of less than 10 percent in $\xi\,\gamma_E(\nu, n_e, T_e)$ since the variations of ξ and γ_E with these abundances are similar in magnitude, but opposite in direction. For the derived mean abundances, the quantity ξ has the value 0.85. The corresponding value for the eight planetary nebulae is 0.84 ± 0.04.

The electron temperature, T_e, and the electron density, n_e, are taken to have the values indicated by the forbidden-line intensities. The value of n_e is, in general, rather poorly specified by the observational material but only enters the present calculation in the computation of $\gamma(2q)$. Inspection of equations (12) indicates that the effect of uncertainties in the value of n_e is only important for $n_e \sim 10^4$. For lower values, $\gamma(2q) \approx \gamma_o(2q)$ whereas for higher values $\gamma(2q)$ becomes small and the 2-photon contribution is negligible in any case. Insofar as $\gamma_o(2q)$ is comparable to $\gamma(H^o)$ for the range of temperatures of interest, the net effect of errors in n_e on the value of γ_E, for $n_e \sim 10^4$, will be further reduced.

The final datum required to compute $r(\mu)$ is $n_e^2 V$. It would be rather unsatisfactory to have to specify this quantity from the rather uncertain n_e-values and the value of V. The latter quantity could only be estimated from the angular diameter and distance of each Seyfert nucleus. However, these nuclei are not, in

general, resolved. Furthermore, even if the nuclei were resolved, an estimation of the "filling factor" would have to be made to obtain the effective emission-volume. Fortunately, there exist two other means of determining n_e^2V. The preferable approach is to use the Balmer jump in emission, the most obvious manifestation of the recombination continuum. If we let $\Delta_B r$ be the amplitude of the observed Balmer jump, corrected for reddening, $\Delta_B \gamma_E(\mu, n_e, T_e)$ the corresponding discontinuity in the calculated γ_E-value at the same point, we can write:

$$\Delta_B r = \frac{n_e^2 V h \nu}{4\pi d^2} \Delta_B \gamma_E(\mu, n_e, T_e), \quad (\mu \cong 2.74) \tag{18}$$

From tables of $\gamma(H^o)$ and $\gamma(He^+)$ we can compute $\Delta_B \gamma_E(\mu, n_e, T_e)$ for the appropriate conditions. As an adequate approximation, we assume $\gamma(He^o) \approx \gamma(H^o)$. Tables of $\gamma(H^o)$, $\gamma(He^+)$, and $\gamma_o(2q)$ have been published by Seaton (1960). We have used the values from somewhat more extensive unpublished tables computed by Oke. From these tables we have derived the following expressions:

$$\Delta_B \gamma(H^o) \cong 3.55 \times 10^{-7} T_e^{-3/2}$$

$$\Delta_B \gamma(He^o) \cong \Delta_B \gamma(H^o) \cong 3.55 \times 10^{-7} T_e^{-3/2} \tag{19}$$

(19) Cont.

$$\Delta_B \gamma(He^+) \cong 2.12 \Delta_B \gamma(H^o) \cong 7.57 \times 10^{-7} T_e^{-3/2} .$$

The two-photon coefficient is continuous so $\Delta_B \gamma(2q) = 0$. From equations (14) and (19) we have:

$$\Delta_B \gamma_E (\mu, n_e, T_e) \cong \Delta_B \gamma(H^o) \left[1+0.12 \frac{n(He^{++})}{n(H^+)} \right]. \quad (20)$$

Inserting this in (18) gives:

$$\Delta_B r \cong \frac{n_e^2 Vh}{4\pi d^2} \Delta_B \gamma(H^o) \left[1+0.12 \frac{n(He^{++})}{n(H^+)} \right] . \quad (21)$$

Since $\eta \approx 0.85$, and $n(He^{++})/n(H^+)$ is approximately 0.03, the second term in brackets is approximately 3×10^{-3} and can be safely neglected. Using equation (19) we rewrite (21) as:

$$\Delta_B r \cong 2.35 \times 10^{-33} T_e^{-3/2} \frac{n_e^2 V}{4\pi d^2} . \quad (22)$$

In those objects for which $\Delta_B r$ is measureable, $n_e^2 V$ can be computed using the temperature derived from the forbidden lines and the distance adopted. (In fact, only $n_e^2 V/4\pi d^2$ need be determined.) This quantity is then inserted in equation (16) and the recombination flux computed.

For many of the objects observed, an accurate determination of the amplitude of the Balmer jump cannot be made. That is, in these instances the observational uncertainties are comparable to, or greater than $\Delta_B r$. The presence of the recombination lines of hydrogen and helium indicates, however, that a recombination continuum is present and the Balmer line intensities can, in principle, be used to determine $n_e^2 V$ (or $n_e^2 V/4\pi d^2$) if we can assume that the recombination decrement is radiative (i.e. Case B). Under these conditions, the observed intensity of any Balmer line, ν_{n2}, can be expressed as:

$$I(\nu_{n2}) = \frac{n_e^2 V}{4\pi d^2} \; 10^{-26} \; Q_n(t) \qquad (23)$$

where $Q_n(T)$ contains the temperature dependence. The Balmer decrements observed, indicate that Case B is not, in fact, applicable but it will have to suffice as a first approximation. In considering the Balmer decrements in the previous chapter (IV-C), it was noted that the effect of significant optical depth in H_β is, to a first approximation, an increase in the H_α intensity and a decrease in the H_β intensity. This would indicate that we should use one of the higher series members ($n > 4$) in applying equation (23), these being relatively unaffected for moderate τ_β. Unfortunately, the intensities of these other Balmer lines are more uncertain than those of

H_β because of faintness ($H\delta$, H_ϵ ,...) or the presence of nearby forbidden-line emission (H_γ). In any case, the intensities H_n/H_β seem to be fairly normal for $n \geq 5$. We therefore shall use the relatively well determined H_β intensities for which $Q_4(T)$ has been conveniently calculated by Pengelly (1964). With $\zeta = 0.85$, and using the adopted temperature, $n_e^2V/4\pi d^2$ can be computed directly from equation (23). The continuous recombination flux is then computed as before. It should be remembered that significant optical depth in H_β will result in a lower value of $n_e^2V/4\pi d^2$ or n_e^2V than is actually the case, with a consequent over-estimation of the recombination continuum level. In those instances where a value of $\Delta_B r$ can be obtained from the observations, the corresponding $n_e^2V/4\pi d^2$ should be considered preferable to that obtained from the H_β intensity.

Table 10 summarizes the data concerning the recombination spectra of the Seyfert nuclei. Columns two and three give the observed monochromatic fluxes on either side of the Balmer jump and the fourth column gives the value of $\Delta_B r$. These values are <u>not</u> corrected for reddening. The fifth column gives $\Delta_B R = 4\pi d^2 \Delta_B r$ where $\Delta_B r$ <u>has</u> been corrected for reddening using the assumed reddening law. Columns 6, 7, and 8 give, respectively, the n_e^2V values obtained from the Balmer jump amplitude, from the H_β

intensity (taken from Table 6), and the adopted value. The last column gives the effective diameter, S, of the emitting volume defined by $S = \left(\frac{2\mathcal{E}}{n_e^2}\right)^{1/3}$ where $\mathcal{E} = n_e^2 V$. Because of the uncertainty in n_e, this value of S should be regarded as rather approximate.

In connection with the Balmer jump amplitudes, a number of factors should be noted: The upper limits given in the table are set by the root-mean-square errors in the scanner observations at $\mu \approx 2.74$. For half of the objects (i.e. NGC1068, NGC1275, NGC3227, and NGC3516) the Balmer jump was weak or absent. To a first approximation the continuum contribution from recombination can be neglected in these cases. For the remaining objects a "built-in" difficulty to the determination of $\Delta_B r$ is present in that the higher Balmer lines are quite broad and, because of their widths and the rather low wavelength resolution, coalesce to produce a general rise in the "continuum" level between $\lambda \sim 4000$ and the Balmer jump. This partially masks the amplitude of the Balmer jump and it is necessary to extrapolate the observed true continuum in order to determine $\Delta_B r$. For NGC4051, NGC5548, and NGC7469 this line contribution to the "continuum" is relatively small and $\Delta_B r$ is easily determined (see Figures 1). For NGC4151, however, it is not immediately clear how this extrapolation should proceed: The continuum appears to flatten somewhat before the point of increasing

flux due to these Balmer lines, is reached. Depending upon the region of continuum extrapolated, values of $\Delta_B r$ over a range of almost a factor of two could be obtained. Fortunately, higher dispersion spectra were available. In addition, a "Case B" calculation of the intensities of the higher Balmer lines relative to H_β (and H_γ) was performed for $T = 2 \times 10^4 °K$. Both sources indicate that the adopted extrapolation (essentially a linear extrapolation of the continuum for $\mu < 2.2$ in Figure 1f) is quite adequate.

Using the adopted $n_e^2 V/4\pi d^2$ values, together with the temperature and density derived from the forbidden-line spectrum and the computed (or assumed) ionic abundances of helium, the continuous recombination spectrum was computed for each object. The results of these calculations are given in Tables 11, where the third column gives $r(\mu)$ and the fourth column gives the observed (reddening corrected) continuous flux minus the continuous recombination contribution. The latter is the same as the total observed flux less the flux contribution from the gaseous component.

Two conclusions regarding the recombination spectrum are of interest. First, it is noted that for those objects in which both the H_β intensity and the Balmer jump amplitude are well determined, the former indicates a lower value of $n_e^2 V$ than does the latter in all cases except that of NGC1068. This could perhaps be interpreted as evidence for significant optical depth in H_β.

However, a comparison of the present H_β intensity data with that obtained by other authors (see Table 6) indicates some uncertainty in the H_β total fluxes. With regard to the Seyfert continua, examination of the energy distributions of Tables 11 indicates that the recombination flux represents an essentially negligible contribution to the total observed flux for most of the objects. For these objects, the residual flux distribution remaining after the gaseous flux (continuous recombination plus lines) has been removed is very insensitive to errors in the values of T_e or n_e^2V used in the calculations. The objects in which these parameters are most critical (NGC4151, NGC5548, and NGC7469) are, not surprisingly, those objects with Balmer jumps of significant amplitude. NGC5548 has the largest relative Balmer jump, the amplitude being about half of the flux immediately redward of $\mu = 2.74$. For this object, the fractions of the observed continuous flux immediately to the red of the Balmer jump due to the recombination continuum are, approximately, 18 percent, 26 percent, and 34 percent for temperatures $T_e \times 10^{-4} =$ 1.5, 2.0, and 2.5, respectively. If we adopt $T = (2.0 \pm 0.5) \times 10^4\,^\circ K$, then the non-recombination flux at this point is (74 ± 8)percent of the total flux: That is, the residual flux is determined to about ± 10 percent for T_e specified to ± 25 percent. At longer wavelengths, the importance of the recombination continuum decreases with

a consequent improvement in the accuracy of the residual flux determination. Shortward of the Balmer jump, the recombination flux is more important, representing (50±5) percent of the total flux. For the temperature range of interest, $\gamma_E(\mu, n_e, T_e)$ varies only slowly with μ in the $\mu > 2.74$ region, and the uncertainty in the computed residual flux is again about 10 percent plus, of course, the uncertainty in the determination of $\Delta_B r$. For NGC4151 and NGC7469, the corresponding uncertainties are considerably smaller and, for the remaining objects, are comparable to the uncertainties in the observed energy distributions.

C. The Non-Thermal Component

Once the continuous spectrum $r(\mu)$ has been computed for a given object, the spectral energy distribution of the gaseous component can be obtained by adding the corresponding emission-line contribution. That is, if $\ell(\mu)$ is the flux at μ due to line emission, the flux distribution of the gaseous component, designated as $g(\mu)$, will be given by:

$$g(\mu) = r(\mu) + \ell(\mu) \quad . \tag{24}$$

For the purposes of the present discussion, all "observed" quantities such as $\ell(\mu)$ are assumed to have been corrected for reddening and are, therefore, directly comparable to computed quantities such as $r(\mu)$. Unless otherwise noted,

all quantities are in flux units (erg cm^{-2} sec^{-1} $(c/s)^{-1}$) and upon multiplication by $4\pi d^2$, where d is the distance to the source, give the corresponding (monochromatic) total emission rate at the source.

We let $S(\mu)$ be the flux at μ due to the stellar component. The form of $S(\mu)$ is assumed to be identical to that of $S_o(\mu)$, the flux distribution of the nuclear regions of a normal spiral. It has not been assumed that the stellar components are of equal brightness in all sources. We will, instead, have:

$$S(\mu) = aS_o(\mu) \qquad a \geqslant 0 \qquad (25)$$

where a is a constant (i.e. independent of μ) which will, in general, have different values for different objects. The flux distribution $S_o(\mu)$ is given in Table 4. If $f_o(\mu)$ is the observed distribution of flux, we can define the "flux" distribution $n(\mu)$ by:

$$n(\mu) = f_o(\mu) - g(\mu) - a\, S_o(\mu) \quad . \qquad (26)$$

If the stellar and gaseous components are the only sources of observed flux, then there will exist some value of the parameter a for which $n(\mu) = 0$ for all μ. (Because of the observational uncertainties in $f_o(\mu)$ and in the computed continuous recombination flux, $r(\mu)$, the condition that $n(\mu) = 0$ should not be too stringently applied. In

practice, this condition should be applied only within the limits set by the estimated uncertainties $\sigma(\mu)$ of $f_o(\mu)$ and $r(\mu)$, i.e. the condition is really $|n(\mu)| < \sigma(\mu)$. We shall, however, refer to this condition as "$n(\mu) = 0$".)

For each object, the observed continuum flux distribution, $f_o(\mu) - \gamma(\mu)$, was obtained from the observations. The continuous recombination flux, $r(\mu)$, was computed using the procedures of the previous section. The differences between these two distributions is then $f_o(\mu) - g(\mu)$. These flux distributions are given in columns 2, 3, and 4, respectively, of Tables 11, and are also shown graphically in Figures 10. If the distribution $f_o(\mu) - g(\mu)$ is compared with that of $S_o(\mu)$ (Figure 9), it becomes clear that there is no value of $\underline{a}$ such that the condition $n(\mu) = 0$ is satisfied for all μ. This is the case for each of the Seyfert nuclei examined.

The failure of the residual flux distributions, $f_o(\mu) - g(\mu)$, to have the form of the "normal" stellar distributions, $S_o(\mu)$, could be the consequence of a number of factors. For example, the continuous recombination calculation could be in error. However, the principal uncertainty in this calculation is the value of $\mathcal{E} = n_e^2 V$ adopted. Alteration of the value of $\mathcal{E}$ only scales the relative importance of the recombination continuum without altering its form. Furthermore, the quantity $n(\mu)$ for each

object was computed according to equation (26) using a range of the parameter $\underline{a}$. For no value of $\underline{a}$ did $n(\mu)$ resemble a recombination spectrum. In any case, the values of $\mathcal{E}$ obtained from the Balmer jump in emission and the H_β intensity are in moderately good agreement. Even in the cases of most extreme difference in $\mathcal{E}(H_\beta)$ and $\mathcal{E}(\Delta_B r)$, the indicated range of $r(\mu)$ is inadequate to explain the differences. It is assumed that the uncertainties in the recombination theory itself are not the source of difficulty. Insofar as the theory is moderately satisfactory in application to other objects, such as planetary nebulae, this assumption seems reasonable.

A second possibility is that there exist systematic errors in the observations. The observations of standard stars were periodically reduced as if of "unknown" objects and the results compared with the adopted calibration. In these instances, the lack of significant differences implies that no systematic errors are present as a consequence of the observational procedures or of the techniques of reduction. Systematic errors in the adopted calibration of the standard stars can be essentially ignored, as far as the present difficulty is concerned. The reason is that $r(\mu)$ is very small in comparison to $f_o(\mu)$ for all μ in some objects, and for most μ in other objects. To the extent that $r(\mu) \ll f_o(\mu) - l(\mu)$, the condition $n(\mu) = 0$ is equivalent to:

$$f_o(\mu) - \ell(\mu) \approx a\, S_o(\mu)$$

for

$$r(\mu) \ll f_o(\mu) - \ell(\mu) \tag{27}$$

and some value of $\underline{a}$. Now $f_o(\mu)$, $\ell(\mu)$, and the flux distribution of the nucleus of the "normal" spiral (NGC224) are all defined by observations made with the same instruments, and with reference to the same set of standards. Therefore, any systematic error in the fundamental calibration will not, to the extent that the recombination continuum is negligible, have any effect upon the condition (27). That is, if there exists some value of $\underline{a}$ which satisfies this condition for the "true" flux distributions, the same value of a will satisfy the same condition for "erroneous" distributions obtained by using an erroneous fundamental calibration. In any case, contemporary model atmosphere calculations are rather more adequate than the required differences would indicate.

A somewhat more likely possibility is that $S(\mu)$ does not have the form of $S_o(\mu)$. For the reasons discussed earlier, the assumption that $S(\mu) \propto S_o(\mu)$ should be a fairly adequate approximation. In any case, the deviations from this relation which would be required in order to explain the observed discrepancies seem to be

ruled out by the observational evidence.

In view of the above, we are forced to the conclusion that $n(\mu)$ is not everywhere zero and, in fact, represents a third component of the continuum energy distributions of the Seyfert nuclei. For reasons which shall become apparent, this third component $n(\mu)$ will be designated as the "non-thermal" component. In view of the fact that the recombination continuum is generally inadequate to explain the absence of the stellar absorption lines and the blue and infrared flux excesses in the Seyfert nuclei, these characteristic features will have to be explained in terms of this third component. On this basis, several general properties of $n(\mu)$ can be stated: First, $n(\mu)$ will have to constitute a significant portion of the continuous flux in the blue and ultraviolet regions in order to suppress the absorption lines of the stellar component and provide the excess of flux observed in this region. On the basis of the observational material, $n(\mu)$ need not necessarily be a major flux-source in the red. The observations of excesses in the infrared continua of some Seyfert nuclei suggest that $n(\mu)$ may be dominant in this region. Finally, the third component must be free of prominent absorption features, for obvious reasons, and, because of both ultraviolet and infrared excesses in flux, can hardly be stellar in nature. Since the Seyfert continua are considerably flatter than that of a normal nucleus, $n(\mu)$ will

also be relatively flat and certainly not significantly steeper than the observed continuum flux distributions.

The "non-thermal" designation applied to this third component rests upon a number of considerations: First, the $n(\mu)$ component is absorption-line free and will possess a form deviating significantly in the blue (and, perhaps, infrared) from that to be expected from stellar sources. The contribution due to the gaseous material is also fairly well accounted for by the emission lines and the continuous recombination spectra of hydrogen and helium. In two instances, non-thermal radiation from Seyfert nuclei is observed in the radio regions. Each of these factors provides somewhat circumstantial evidence for the non-thermal nature of this component. The decisive factor, however, is the observation of polarized components in the optical flux of some Seyfert nuclei: Of the eight objects under consideration, all but one, NGC3516, have been reported to show such polarization (Hagen-Thorn and Dombrovsky 1967, Walker 1968a). In most instances the magnitude and/or the wavelength dependence of the observed polarization cannot be interpreted as of interstellar origin. In NGC1275, at rather low galactic latitude, part of the polarization in the R-bandpass could, perhaps, be due to the effects of intervening obscuring material, but the overall distribution of polarization with wavelength can probably not be interpreted in this manner (Visvanathan

1968b). Polarized optical radiation is not commonly encountered in the nuclei of normal galaxies, planetary nebulae, or in groups of stars. It is, on the other hand, associated with such objects as the Crab Nebula in which part of the optical flux is believed to arise from the synchrotron process. Such polarization, therefore, provides strong evidence for the existence of a non-thermal component to the optical flux of the Seyfert nucleus in which it is observed.

For most of the Seyfert nuclei, the observed polarization is but slightly above the limit of detectability (roughly 0.5 percent) and of relatively little value in determining the form of $n(\mu)$, other than producing evidence for the existence of such a third component. For two objects, NGC1068 and NGC1275, a relatively well-defined relation between polarization and wavelength is available (Visvanathan and Oke 1968, Visvanathan 1968b) and can be used to determine the form of $n(\mu)$ or, equivalently, to determine $\underline{a}$. In order to perform this determination, it is necessary to make two assumptions: It is assumed, first, that the observed polarization arises completely from the non-thermal component $n(\mu)$. The second assumption is that the radiation of $n(\mu)$ has a percentage polarization p_o which is independent of μ. Under these conditions, the variation of the observed percentage polarization, $p(\mu)$, with μ will be a

consequence only of the varying relative importance of thermal and non-thermal sources of radiation. With these assumptions

$$p(\mu) = p_o \, n(\mu)/f_o(\mu) \tag{28}$$

It should be noted that a small correction to the observed values of $p(\mu)$ is, strictly speaking, necessary to account for the effects of interstellar reddening. This correction, however, is only of consequence if the extinction varies significantly over the bandpass, centered on μ, for which the polarization measurements are made. In practice, this is not the case and the observed values of $p(\mu)$ can be used in equation (28).

For those objects in which $p(\mu)$ has been measured at two or more wavelengths, corresponding to μ_i, we can use equations (26) and (28) to write:

$$f_o(\mu_i)\, p(\mu_i)/p_o = f_o(\mu_i) - g(\mu_i) - a\, S_o(\mu_i) \tag{29}$$

$$i = 1, 2, \ldots$$

This set of equations can then be solved for the values of p_c and $\underline{a}$. Once this is accomplished, the individual components of which $f_o(\mu)$ is composed are each completely specified.

For most of the objects under consideration, the available polarization data are inadequate to permit a

solution for p_o and $\underline{a}$ in the above fashion. In these instances the value of $\underline{a}$ can be somewhat specified on observational or theoretical grounds. For instance, if absorption lines were observed in the Seyfert nuclei, which were also present in the spectra of normal nuclei, the relative strengths in each instance could be used to specify the relative importance of the stellar component in the Seyfert nuclei. Unfortunately, such absorption is not observed in the Seyfert nuclei. An upper limit on the value of $\underline{a}$ can be established by utilizing an estimate of the detection limit for such absorption features on the available spectra. This detection limit is obtained by assuming that the weakest absorption line observable has a depth equal to the noise amplitude on the spectrum.

In practice, it was found that a more stringent limitation could be placed on $\underline{a}$ by imposition of the condition that $n(\mu)$ be a monotonically decreasing function of μ. The basis for this condition is the nature of the distribution of synchrotron radiation from an assembly of relativistic electrons: For a monoenergetic energy distribution of such electrons, the maximum of the emitted flux distribution will occur at $\mu \sim 1/3\ \mu_c$, where μ_c corresponds to the usual critical frequency. For $\mu > 1/3\ \mu_c$, the flux distribution is a monotonically decreasing function of μ, asymptotically

of the form

$$\left(\frac{\mu}{\mu_c}\right)^{1/2} \exp\left(-\frac{\mu}{\mu_c}\right)$$

If we consider an assembly of electrons with a distribution in energy, we expect that the resultant flux distribution will be monotonically decreasing for $\mu > \frac{1}{3}\mu_c(\max)$, where $\mu_c(\max)$ corresponds to the critical frequency of the most energetic of the electrons. The condition is actually rather weaker than necessary in that we expect that the most energetic electrons will not, in general, be the most abundant since the most energetic electrons will decay fastest in energy because of radiation losses. If $n(\mu)$ arises from such a distribution, the condition that it be a monotonically decreasing function of μ, over the wavelength region of interest ($1 \leq \mu \leq 3$) is essentially equivalent to requiring that $\mu_c(\max) < 3$. There are two considerations which indicate that this condition will be satisfied: Since $\mu_c \propto EH_\perp^{1/2}$, where E is the electron energy and $H_\perp$ is the magnetic field strength, values of $\mu_c(\max) \geq 3$ would imply electron energies or field strengths vastly in excess of those customarily encountered in the most energetic non-thermal objects. ($\mu_c = 3$ corresponds to $EH_\perp^{1/2} \approx 7.5$ BeV-gauss$^{1/2}$.) For two Seyfert galaxies, the radio observations indicate a flux distribution, non-thermal in character, which

generally tends downward with increasing frequency. The infrared observations indicate similar behavior. If the radio and/or infrared flux distributions are considered to arise from the same electron distribution as does the optically polarized component, further evidence that $n(\mu)$ satisfies this condition is provided. With the condition that:

$$\frac{dn(\mu)}{d\mu} \leq 0 \quad , \quad 3 \geq \mu \geq 1 \tag{30}$$

the expression (26) can be used to obtain:

$$\frac{d}{d\mu} \left[f_o(\mu) - g(\mu) - aS_o(\mu) \right] \leq 0 \quad , \quad 3 \geq \mu \geq 1 \tag{31}$$

For each object, the distribution of $n(\mu)$ was computed according to (26) for various assumed values of the parameter $\underline{a}$. An upper limit on $\underline{a}$ was obtained by selecting that distribution which best satisfied the condition of equation (30) for the observed range of μ. Using this maximum value of $\underline{a}$, an upper limit on the stellar contribution (and a lower limit to the non-thermal contribution) to the observed flux distribution was obtained for each object. These limiting forms are given in the last two columns of Tables 11.

For the two objects for which $p(\mu)$ is fairly well determined, equations (29) were solved for p_o and $\underline{a}$ and the individual components computed. Within the

uncertainties of the observed polarization and flux distributions, the non-thermal component of NGC1068 is essentially coincident with the limiting form of $n(\mu)$ (Figure 10a). This determination agrees quite well with that of Visvanathan and Oke (1968) for this object. In the instance of NGC1275, the other extreme is nearly attained: The polarization data fit the observed flux distribution almost as well as it does the limiting $n(\mu)$ distribution: The present data would indicate, therfore, that the non-thermal component is dominant over much of the observed frequency region (cf. Figure 10b).

An implicit assumption has been repeatedly made in the above computations, namely that there is no fourth component to the observed flux. If such a component were present, it could not be assumed that $n(\mu)$, now characterizing two components, possessed an intrinsic polarization p_o which was independent of frequency. In their analysis of the spectrum of NGC1068, Osterbrock and Parker (1965) concluded that the observed ultraviolet radiation could be understood in terms of the two-photon emission of neutral hydrogen, excited by fast protons. Such an interpretation, however, does not assist in explaining the observed optical polarization and rests upon assumptions regarding the ionization mechanism which are difficult to verify. The assumption that the ultraviolet flux is due to synchrotron photons, on the other hand, is consistent with both

observational properties. In addition, the non-thermal third component may well be used to explain the infrared excesses whereas 2-photon radiation is inadequate in this regard. Finally, the observed dependence of polarization on wavelength is consistent with the $n(\mu)$ adopted for this object, and the latter accounts satisfactorily for the observed ultraviolet flux. The presence of a fourth component in any significant amount would alter this agreement. Observation of polarization in the infrared would provide a very strong argument for the non-thermal interpretation although the absence of such polarization would leave the question open. Similar arguments against the presence of a fourth component can be made in the case of NGC1275. For the remaining objects, an improvement in the quality of the polarimetric data must be awaited before this question can be resolved.

VI. THE SOURCE OF IONIZATION

A. The Mechanism of Ionization

The emission lines observed in the spectra in the Seyfert nuclei indicate that a wide range of ionization conditions are present in the emission-line regions of these objects. In every instance for which adequate spectroscopic material was available, lines arising from OI and NeV are observed, representing a 63eV. spread in ionization potential. Oxygen is present in the first two stages of ionization as well as in the neutral form. Weak lines indicating the presence of much higher levels of ionization are observed in the two objects for which the most extensive spectroscopic data are available: The forbidden emission lines of FeVII, observed in both NGC1068 and NGC4151 correspond to an ionization potential of 79 electron volts. Oke and Sargent (1968) have observed and measured the coronal [FeXIV] λ5303 emission in NGC4151, but this 355 eV. line is too weak to be seen on the present group of spectra. It is suspected that more sensitive spectroscopy of the remaining Seyfert nuclei would reveal similar lines of very high excitation. It is not, however, clear what is the source of the observed ionization conditions.

The electron temperatures indicated by the forbidden lines suggest that collisional ionization by thermal

electrons can probably be ignored as a significant factor in producing the observed levels of ionization: Relative populations of the levels of ionization for a number of elements have been calculated as functions of temperature by House (1964) and Parker (1964). Dielectronic recombination corrections, important at high temperatures, have been approximately treated by Osterbrock and Parker (1965) in their discussion of the spectrum of NGC1068. The results of these calculations indicate that at most two ionization states of a given atom are significantly represented for electron temperatures within the range of interest. The presence of [OI] , [OII] , and [OIII] lines in a given object are, therefore, difficult to reconcile with this mechanism. The calculations indicate that a temperature $T_e \gtrsim 4 \times 10^4 °K$ is required in order that there be a significant amount of OIII in the emitting region but, for such temperatures, OI is essentially non-existent and the presence of the [OI] lines becomes difficult to explain. The temperatures required to produce NeIII and NeV, to say nothing of FeVII and FeXIV, are correspondingly higher and would seem to be inconsistent with the presence of lines such as [OI] , [OII] , [NII] , [SII] , etc. This difficulty might be resolved by postulating rather large variations in T_e throughout the emitting region, the lines arising from different levels of ionization being formed in different parts of the Seyfert nuclei. In the

present instance, such variations in electron temperature may well be present, but cannot account for both the level of ionization and the strengths of the corresponding lines. In every instance, the ratio of the forbidden lines indicates $T_e \lesssim 2 \times 10^4 °K$ and for six out of the eight objects the intensity ratios of the [OIII] lines alone permit an upper limit of $T_e \lesssim 2 \times 10^4 °K$ to be placed upon the region responsible for the [OIII] emission. However, for OIII to exist in this region, $T_e > 4 \times 10^4 °K$ is required if the mechanism is collisional ionization by thermal electrons. Although such a mechanism may play a part in determining the ionization conditions within the Seyfert nuclei, it is clearly inadequate to explain the range of these conditions observed in a fashion consistent with the relative emission line intensities. Other ionization mechanisms should, therefore, be considered.

Having rejected photoionization by non-thermal photons, Osterbrock and Parker (1965) considered the possibility of ionization by high energy particles, principally protons and hydrogen atoms, in the nucleus of NGC1068. These considerations were necessarily rather approximate, largely due to the lack of information regarding the ionization cross-sections for this process. Such an ionization mechanism is fairly plausible in the case of the Seyfert nuclei: To produce the necessary range of ionization, particle energies in the vicinity of 20keV

are required. For protons and hydrogen atoms, such energies correspond to velocities in the region of 2000 km/sec, the presence of such velocities being indicated by the widths of the forbidden line profiles. The initial particle energies could then result from collisions between clouds within the Seyfert nucleus, the kinetic energy of the relative motions being converted into ionization energy in thin layers near the point of interaction. (The layers must be thin because the range of the particles is small for the energies of interest.) Insofar as the general conclusions of Osterbrock and Parker (1965) in regard to this mechanism are equally applicable to the remaining Seyfert nuclei, and since no observational means of testing the applicability of this mechanism to Seyfert nuclei is available, ionization by fast particles will not here be considered in greater detail.

The presence of excess radiation in the blue and ultraviolet Seyfert continua suggests that the radiation field in the far ultraviolet may be quite large and that this radiation be considered as a possible source of the ionization. If this ionizing flux arises from a small source, i.e. not distributed throughout the line emitting region, the ionization conditions might be considered analogous to those in planetary nebulae in which the radiation source is a central star. In the latter case, the work of Strömgren (1939) indicates the presence of

sharply defined zones of ionization, with the lower ionization zones lying at greater distances from the source of ionizing radiation. Such a model for the Seyfert nuclei, however, encounters a rather major difficulty: A peculiar feature of most of the Seyfert spectra is the weakness or absence of the permitted OIIIλ3444 emission line. This line, together with OIIIλ3312, is invariably observed in planetary nebulae showing HeII and [OIII] line emission. Typically, the strength of λ3444 in such planetary nebulae is comparable to that of HeIIλ4686 or [OIII] λ4363. In the Seyfert nuclei this line is relatively weaker by at least a factor of five. (The λ3444 intensity obtained for NGC4051 is extremely uncertain insofar as the line was "detected" only marginally on some plates and "absent" on others. At the present resolution the strength determination is complicated by the proximity of [NeV]λ3425.) The presence of λ3444 and λ3312 in planetary nebulae results from an accidental coincidence between the Lyman-α line of HeII (303.78Å) and the $2p^2\ {}^3P_2 - 2p3d\ {}^3P_2$ line of OIII(303.80Å) (Bowen, 1935). The only explanation for the absence of λ3444 (and λ3312) is that the HeII Ly-α photons are destroyed before they can be "converted" into observable λ3444 quanta. As a mechanism for this destruction, the most probable seems to be the photoionization of neutral helium or hydrogen. The absence of λ3444, therefore,

indicates the presence of significant amounts of neutral hydrogen and helium in the regions where the [OIII] and HeII emission lines are formed. It should be noted that this conclusion lends further weight to two possibilities discussed previously: A significant H^{o} abundance would greatly increase the number of atomic scatterings experienced by (hydrogen) Ly-α quanta before escape from the emitting region, with a consequent increase in the n = 2 level population. As a result the optical depth in the Balmer lines would increase. With this greater optical depth, the effects of self-absorption and electron scattering are effectively increased. A significant H^{o} abundance, therefore, is consistent with (1) the absence of the permitted OIII lines, (2) the electron-scattering model for the profiles of the Balmer wings, (3) the relative wing and core intensities indicated by this model and the observations, and (4) the self-absorption interpretation of the Balmer decrements. (cf. V). The ionization model based upon "Strömgren spheres" is, however, inconsistent with the above indications. The HeII region would be essentially free of neutral hydrogen and helium. Since this region would be presumably optically thick to HeII Lyα, the permitted lines of OIII would have to arise in this HeII region. Since no He^{o} or H^{o} is present, the HeII Lyα quanta cannot be destroyed before "conversion" into λ3444 and λ3312 and, all regions being optically thin

to these wavelengths, this OIII radiation should be observed: In fact, it is not. The only solution to this difficulty would seem to be the requirement that a large number of such ionizing sources of radiation is present, sufficient in quantity that the thin mixed-ionization regions between the HeII and HeI zones comprise a significant fraction of the total emitting volume. Alternatively, a source of ionizing radiation which is distributed continuously throughout the emitting region might be considered. As a first approximation, neither approach is very satisfactory: If the individual sources were too closely spaced, or the radiation of the extended source beyond the ionization limit too great, the emitting volume would be an HeII-HII region and the OIII lines would be observed. For too distant a spacing of individual "point sources", most of the volume would be an HI-HeI region and there would be essentially no mixing of ionization levels. As in the opposite case, λ3444 would be observed. For an extended source, a much lower level of ionizing flux will result in a large HI-HeI region with no forbidden line emissions. Both models would therefore seem to be applicable only within a very narrow range of conditions and it would seem unlikely that this metastable condition could be maintained for any length of time in all of the Seyfert nuclei examined.

A final objection to such multi-source or ex-

tended source models is the observation of optical variability in some of the Seyfert nuclei. Insofar as the time scales are short in comparison to the light transit times of the nuclei, such extended sources are contraindicated. If the flux of the ionizing radiation varies in a similar manner, it is difficult to see how the conditions of mixed ionization of hydrogen and helium could be maintained. As the ionizing flux increased, it would be expected that HeII λ4686 would increase in strength and, as a consequence of the lower H^{o} abundance, the wings of the Balmer lines would decrease in intensity, and the $H\alpha/H\beta$ intensity ratio would decline. (This assumes that the electron-scattering and self-absorption interpretations of these features are the correct ones.) In only one instance, NGC3516, is there evidence for such spectral variation and, in this instance, the observational data are very uncertain.

Strömgren's (1939) considerations, however, were intended for application to planetary nebulae in which the source of ionizing radiation is a central star. Williams (1967) has shown that considerable mixing of levels of ionization will occur if the distribution of the ionizing radiation is considerably flatter than that of the usual exciting star. The optically thick models, in this case, correspond to a source or sources distributed throughout the emitting region. Since the non-

thermal optical components of some of the Seyfert nuclei seem to possess relatively flat distributions, it might be expected that this flatness is characteristic of the far-ultraviolet non-thermal radiation as well. The calculations of Williams (1967) indicate that such a distribution will produce the mixture of ionization levels observed and, specifically, will permit both neutral and ionized forms of hydrogen and helium to occur in the same regions. This factor will resolve the difficulties regarding the OIII λ4344 line discussed above. The principal question, then, is whether the strength of this ultraviolet radiation is adequate to produce the range of ionization observed.

Since the far ultraviolet region is not accessible to observation, estimation of the available flux of ionizing radiation must be based upon extrapolation of the non-thermal optical and/or radio continua to very much higher frequencies. As is indicated below, this can be a rather hazardous procedure. We shall consider the ionizing flux available for the ionization of hydrogen in terms of the observed intensities of Hα: If $n(\mu)$ is the non-thermal flux distribution at the earth, the <u>number</u> of photons received at the earth capable of ionizing hydrogen will be:

$$\Phi(\mu_o) = \int_{\mu_o}^{\infty} \frac{n(\mu)\, d\mu}{h\mu} \qquad (cm^{-2}sec^{-1})$$

where μ_o corresponds to the Lyman limit ($\mu_o \cong 10.97$). If the gas is optically thick to $\mu \geq \mu_o$, every ionizing photon will be absorbed by the gas, each ionizing a single H^o atom. Each of these ionizations is followed by a recombination. According to Spitzer (1948) about 0.65 of the recombinations (under Case B conditions) occur to the third or higher levels. If all recombinations to $n \geq 3$ eventually result in the emission of an $H\alpha$ photon, the $H\alpha$ flux observed will be:

$$I(H\alpha) \approx 0.65 h \nu_\alpha \Phi(\mu_o)$$

$$\approx 2 \times 10^{-12} \Phi(\mu_o) \quad \text{erg/cm}^2\text{sec}$$

Osterbrock and Parker (1965) extrapolated the non-thermal radio spectrum of NGC1068 to large frequencies. According to Kellermann (1964), $n(\mu) \propto \mu^{-\alpha}$, where $\alpha = 0.59$ and $n(\mu) = 1.04 \times 10^{-22}$ erg/cm^{2}sec (c/s) at 400 Mc/s ($\mu \simeq 1.3 \times 10^{-6}$). Using these values, and assuming that this spectrum continued to $\mu >> \mu_o$, Osterbrock and Parker obtained $\Phi(\mu_o) \approx 2.2$ and $I(H\alpha) \approx 4 \times 10^{-12}$ erg/cm^{2}sec. Comparing the latter value with their observed $H\alpha$ intensity of 1.6×10^{-11} erg/cm^{2}sec, they concluded that there were insufficient ionizing photons to explain the observed $H\alpha$ intensity (We obtain an observed reddening-corrected $H\alpha$ intensity of

2.1×10^{-11} erg/cm^2 sec.). However, this extrapolation of the radio spectrum predicts a flux $n(3) \approx 1.9 \times 10^{-26}$ erg/cm^{2}sec (c/s) at λ3333 whereas a small extrapolation of the non-thermal component (Figure 10a) for this object indicates $N(3) \approx 1.7 \times 10^{-25}$. Fitting a power law of the form used by Osterbrock and Parker to the present data yields $\alpha \approx 0.55$, in fairly good agreement with the above value. Extrapolation of the optical data, however, indicated $\Phi(\mu_o) \approx 23.$ and $I(H\alpha) \approx 4.6 \times 10^{-11}$, a factor of two greater than the observed intensity. This would seem to indicate that the ionizing flux might be adequate to explain the observed intensity of $H\alpha$. It is, however, suspected that this extrapolation is nearly as extreme as that based upon the radio data. One feature, however, seems clear: The non-thermal spectrum of NGC1068 does decrease in curvature toward shorter wavelengths in the accessible optical and radio regions. If this continues into the far ultraviolet, the number of available photons capable of ionizing hydrogen will increase significantly over the above values. Finally, it should be noted that a power-law extrapolation of the non-thermal component is not necessarily the most reasonable insofar as the intensity distribution of synchrotron radiation is proportional to $\nu^{-\gamma} G(\nu/\nu_2)$ where γ is a constant which depends upon the conditions within the source and ν_2 is the high-energy cutoff frequency.

$G(\nu/\nu_2)$ is tabulated by Westfold (1959) as a function of ν/ν_2. For $\nu << \nu_2$, the intensity distribution does approximate a power law, but for $\nu >> \nu_2$ the intensity distribution is exponential. In the first instance, where $n(\mu) \propto \mu^{-\alpha}$, we have

$$\Phi(\mu_o) = \frac{S(\mu_o)}{\alpha h}$$

whereas in the second instance, with $n(\mu) \propto \exp(-\gamma\mu)$, we have

$$\Phi(\mu_o) = \frac{S(\mu_o)}{h} e^{\gamma\mu_o} E_1(\gamma\mu_o)$$

where E_1 is the usual exponential integral. Applying the latter form to the radio data will yield greater discrepancies with respect to the optical non-thermal fluxes, and extrapolation of the optical non-thermal component to the far ultraviolet will yield somewhat lower values of $\Phi(\mu_o)$ than obtained from the power-law extrapolation. (In the case of NGC1068, an exponential extrapolation yields $\Phi(\mu_o) \approx 0.6$.)

Only in the instances of NGC1068 and NGC1275 is the non-thermal component adequately specified by the available polarization data and the present observations. In the latter case, extrapolation of the adopted non-thermal distribution to large frequencies indicates that the available ionizing flux may be adequate to explain the

observed Hα intensity. For the remaining objects, only the lower limits of the $n(\mu)$ distributions are available and, because these lower limits are probably flatter than the true distributions, an extrapolation such as performed above would usually result in an overestimate of $\Phi(\mu_o)$. The latter conclusion assumes, of course, that the non-thermal spectrum can be represented by a power-law or exponential form : In the cases of NGC3227 and NGC4051, neither form seems very adequate even when the rather large uncertainties are taken into consideration. It is of interest, however, that the limiting $n(\mu)$ of NGC1068, NGC1275, NGC3516, and NGC4151 are similar in that they are all quite flat and can be fitted adequately with an exponential form (and equally well with a power-law). The limiting forms in NGC5548 and NGC7469 are different in that both curve upward in the red. This might suggest that these two objects would show greater excesses than the others in the near infrared.

The question of the appropriate ionization mechanism, or mechanisms, responsible for the ionization conditions in the Seyfert nuclei is clearly not resolved by the present observations. Neither the ionization by synchrotron photons, nor ionization by high energy particles can be rejected on the basis of the available material. On the other hand, neither mechanism can be proved the applicable one although more extensive

observational data might assist in this regard. In particular, the energy spectrum of ionizing particles might be inferred from the detailed velocity profiles of the emission lines and a better basis for the extrapolation of the non-thermal continua might be provided by additional ultraviolet and infrared observations. Of particular importance in this regard is the observation of the infrared Paschen lines in order to estimate the effects of reddening upon the observations.

A rather severe shortcoming of the fast-particle ionization mechanism has been pointed out by Souffrain (1968): Under such a mechanism, the forbidden lines should be much stronger, relative to the recombination lines, than is observed. Because the cross-section for electron-proton and electron-electron interactions is much greater than that for ionization or direct collisional excitation of H_α, most of the particle energy would be dissipated in heating, rather than ionizing the gas. Much of this energy, therefore, would appear as forbidden-line emission rather than in the recombination lines. Observationally, the forbidden lines are much weaker, relative to the Balmer lines than the (admittedly rough) calculations based upon fast-particle excitation would indicate. This implies that direct collisional excitation by fast particles is probably not the appropriate mechanism. In a general way, the above conclusion can be applied to almost any

collisional mechanism. It seems likely, therefore, that the radiation field is primarily responsible for the obser- observed mixture of ionization levels. The calculations of Strömgren (1939) and Williams (1967) discussed above imply that the distribution of this ionizing radiation must be considerably flatter than the Planckian exponential of Strömgren's exciting-stars, in order that significant mixing of ionization levels may occur.

B. The Energy Sources

As for the non-thermal sources of optical and/or radio radiation, the fundamental problem in the case of the Seyfert galaxies is the specification of the mechanism responsible for the production of the relativistic electron energies. It must here be presumed that the observed "non-thermal" radiation does, in fact, arise via the synchrotron process and as a consequence of the interaction of the relativistic electrons with a magnetic field. The principal evidence for this assumption, as discussed earlier, is the presence of optical polarization and/or non-thermal radio spectra.

In confronting this problem, a first step is the estimation of the energetics and associated time scales of the relevant process(es). A crude estimate of the total lifetime of the Seyfert phenomenon in galaxies can be obtained from the observed frequency of such objects:

Since about 2 percent of all spiral galaxies are of the Seyfert type, a lifetime of about 10^8 years is obtained if it is assumed that all spirals undergo a Seyfert phase at some point in their evolution. If the Seyfert category is taken to include some of those objects presently classified as N-galaxies, the corresponding time-scale becomes greater. At the other extreme, assuming that only 2 percent of galaxies are capable of every becoming Seyfert galaxies yields a characteristic time of $\sim 10^{10}$ years. A lifetime of $10^{9\pm1}$ years is, therefore, indicated.

A somewhat different time-scale estimate can be obtained by assuming that the Seyfert phenomenon is a consequence of a number of violent events occurring in the nuclear regions. Burbidge, Burbidge, and Sandage (1963), in discussing the evidences for the occurrences of such events in galaxies, estimated that the kinetic energy of the ionized gas in Seyfert nuclei was in the range $10^{55\pm2}$ ergs. If it is assumed that <u>all</u> of this kinetic energy is converted into line emission, approximately 10^{42} erg/sec, through heating of the gas, a time scale of about $3 \times 10^{5\pm2}$ years is indicated. With observed total luminosities being in the range of $10^{45\pm1}$ erg/sec, a somewhat comparable time scale of 10^5 years or less results from similar considerations. These imply the occurrence of at least 10^3 events in the lifetime

of the Seyfert phenomenon.

Finally, the emission line profiles indicate velocities in excess of the 500 km/sec which is typical of the escape velocities of normal spiral systems. This suggests that mass will almost certainly be ejected from the nuclear regions, as is indicated by the spectroscopic data in some instances. Taking 10^3 km/sec as a velocity characteristic of the mass motions in the Seyfert nuclei, and 10 pc. as a characteristic diameter for the nuclei, an escape-time of about 10^4 years results. (A somewhat shorter lifetime is obtained if the Balmer wings are interpreted as being of kinematic origin. We are here assuming that these wings are formed by electron scattering.)

Insofar as the latter pair of estimates, based upon the observational data for the individual objects, indicate smaller time scales than the 10^9 years indicated by the frequency of Seyfert galaxies among spirals, the occurrence of a rather large number of energetic events is implied. Significant variations in the continuum fluxes of these objects have been reported as occurring within intervals of considerably less than one year. In the case of NGC3516, line intensity variations have occurred over a span of about 25 years. Such variations lend further weight to the suggestion that the energy production occurs in the form of a series of violent

events rather than as a more-or-less continuous process.

A number of mechanisms for the production of the requisite amount of energy have been suggested. Certain processes which involve the gradual accretion of matter from the intergalactic medium have been proposed (e.g. Sturrock and Feldman, 1968). One shortcoming of such models is the requirement that the conditions of the intergalactic medium in the environs of the Seyfert galaxies be highly peculiar. As discussed above, it is also difficult to interpret the observed intimate mixture of levels of ionization as being produced in the shock-fronts resulting from the infall of such material. Furthermore, such models would seem to imply a fairly smooth input of energy and would, therefore, not adequately explain the observed radio and optical variations which are of relatively short time scale.

Perhaps the strongest indication of the mechanism responsible is the fact that the characteristic Seyfert spectra arise in the centers of the galaxies rather than in the external or spiral-arm regions. Insofar as galactic nuclei are generally characterized by a higher density of matter, and higher velocities, than the outer regions, the interaction between stars or gas clouds may produce the requisite energy in some fashion. The possibility of cloud collisions is suggested by the structure occasionally found in the emission lines. As in the accretion model,

however, it is not clear how an extremely close mixture of ionization levels could be produced at the resulting shock fronts. A second difficulty with both the cloud-collision and accretion models is that no clear mechanism for the production of the relativistic electrons, implied by the spectra and polarization, is apparent.

The most tempting hypotheses, at present, rest upon supernovae as energy sources. Supernovae, or supernova-like events, might be produced by the accretion of the gaseous material by the nuclear stellar population. The accumulation of such material by the more massive stars might be adequate to result in the rapid evolution of these objects to the supernova stage. An alternative hypothesis, of somewhat similar nature, is based upon interactions between the stars themselves: If the stellar density is sufficiently great, violent events might result from the disruptive consequences of such interactions. On the other hand, coalescence into more massive stars ($\backsim 50 M_{\odot}$) might result with the resulting massive objects evolving rapidly to the supernova phase. The latter possibility has been considered by Colgate (1968). Although the available calculations are rather approximate, preliminary results have indicated the feasibility of such a mechanism.

Such supernova explosions are satisfactory in two principal regards: First, such violent events might

adequately explain the broad line profiles observed - the motions of the emitting gas arising directly as a consequence of such events. Second, and perhaps most significantly, a means for the production of relativistic electrons is provided. Instances are known in which the violent evolution of stars has eventually resulted in the production of non-thermal radiation. (e.g. the Crab nebula, which is a supernova remnant). It suffices, for present purposes, to know that such non-thermal radiation can be produced in this manner, despite the fact that the details of the process are not understood.

An advantage of the supernova hypothesis is that it may well be capable of observational verification: The luminosity maximum for such an explosive event is typically of the order of 10^{43} erg/sec (Colgate, 1968) which might well produce an apparent motion of the observed Seyfert nucleus if the latter is resolved. (It is understood that an attempt to detect such motion in the nuclear image of NGC4151 is presently underway at the U. S. Naval Observatory at Flagstaff). Energetically, a supernova model does provide an adequate energy input: Typically 10^{50} erg is radiated as a consequence of such an explosion.

On the basis of such evidences as are available, the supernova hypothesis seems the most plausible in that such events are known to be capable both of eventually

producing non-thermal radiation and mass-motions of gaseous material. The details of both processes however, are not understood and resolution of this problem must await further theoretical and observational studies.

REFERENCES

Allen, C. W. 1963, Astrophysical Quantities, 2nd ed. (London: University of London Press), p. 197.

Aller, L. H. 1963, Astrophysics, 2nd ed. (New York: Ronald Press), p. 166.

Aller, L. H. and Liller, W. 1968, Nebulae and Interstellar Matter, ed. B. M. Middlehurst and L. H. Aller, (Chicago: University of Chicago Press).

Andrillat, Y. 1968, *SGRO, Paper 15.

Ambartsumian, V. A. 1933, Pulkovo Obs. Bull., 13, 3.

———————— 1958, Theoretical Astrophysics (New York: Pergamon Press), p. 494.

Arp, H. C. 1968, SGRO, Paper 4.

Arp, H. C. Khachikian, E. Y., Lynds, C. R., and Weedman, D. 1968 Ap.J. 152, L103.

Arp, H. C. 1962, Ap.J., 135, 971.

Bethe, H. A., and Salpeter, H. 1957, Hdb.d.Phys., 35, 352.

Bowen, I. S. 1935, Ap.J., 81, 1.

Boyarchuk, A. A., Gershberg, R. E., and Pronik, V. I. 1963, Izv.Krym.Astrofiz.Obs., 29, 291.

Burbidge, E. M., and Burbidge, G. R. 1965, Ap.J., 142, 1351.

Burbidge, E. M., Burbidge, G. R., and Prendergast, K. H. 1959, Ap.J., 130, 26.

Baker, J. G. and Menzel, D. H. 1937, Ap.J., 86, 70.

---

*SGRO: "Proceedings of the Conference on Seyfert Galaxies and Related Objects", Steward Observatory, University of Arizona, 14-16 February, 1968. ed. Pacholczyk, A.G., and Weymann, R.J. (preprint).

Burbidge, E. M., Burbidge, G. R., and Prendergast, K. H. 1963, Ap.J., 137, 1022.

Burbidge, G. R. SGRO, Paper 30. 1968.

Burbidge, G. R., Burbidge, E. M., and Sandage, A. R. 1963, Rev.Mod.Phys., 35, 947.

Campbell, W. W., and Moore, J. H. 1918a, Lick Obs. Publ., 13, 88.

_____ 1918b, ibid., 13, 122.

Capriotti, E. R. 1964, Ap.J., 139, 225.

Chester, C., and Roberts, M. S. 1964, A.J., 69, 635.

Code, A. D. 1960, Stellar Atmospheres, ed. J. L. Greenstein, (Chicago: University of Chicago Press), p. 50.

Code, A. D., and Liller, W. 1962, Astronomical Techniques, ed. W. A. Hiltner (Chicago: University of Chicago Press).

Colgate, S. A. 1968, SGRO, Paper 40.

Dent, W. A. 1965, Science, 148, 1458.

deVaucouleurs, G., and deVaucouleurs, A. 1968 SGRO, Paper 12.

Dibai, E. A., Esipov, V. F., and Pronik, V. I. 1968, Soviet Astron.-AJ, 11, 553.

Dibai, E. A., and Pronik, V. I. 1968, Soviet Astron.-AJ, 11, 767.

_____ 1965, Astrofizika, 1, 78.

Dibai, E. A., and Shakhlovski, I. S. 1966, Astron.Cirk., 375, 1.

DuPuy, D. L. 1968, SGRO, Paper 25.

Fastie, W. G. 1952, J.Opt.Soc.America, 42, 641.

Fath, E. A. 1908, Lick. Obs. Bull., 5, 61.

Field, G. B. 1959, A.J., 64, 58.

Hagen-Thorn, B. A., and Dombrovski, V. A. 1967, Astron.Cirk., 454, 4.

Haro, G. 1956, Bol.Obs.Tonantzintla.yTacubaya, 14, 8.

Heeschen, D. S., and Wade, C. M. 1964, A.J., 69, 277.

Holmberg, E. B. 1957, Medd.Lund.Ser.II, 136.

House, L. L. 1964, Ap.J.Suppl, 8, 307.

Hubble, E. P. 1926, Ap.J. 64, 328; Mt.W.Contr. 324.

_____ 1934, ibid., 79, 8.

Humason, M. L. 1932, Pub.A.S.P., 44, 267.

Humason, M. L., Mayall, N. U., and Sandage, A. R. 1956, A.J., 61, 97.

Johnson, H. L. 1966, Ann.Rev.Ast.and Ap., 4, 193

Kellermann, K. I. 1964, Pub.Owens Valley Radio Observatory, Vol. I, No. 1

Kellermann, K. I., and Pliny-Toth, I. I. 1968, Ap.J., 152 L169.

Khachikian, E. Y. 1968, SGRO, Paper 31.

Kinman, T. D. 1968, SGRO, Paper 27.

Low, F. J., and Kleinmann, D. E. 1968, SGRO, Paper 17.

Lynds, C. R. 1968, SGRO, Paper 29.

Matthews, T. A., Morgan, W. W., and Schmidt, J. 1964, Ap.J., 140, 35.

Mayall, N. U. 1934, Pub.A.S.P., 46, 134.

Mayall, N. U. 1939, Lick Obs. Bull, 19, 33.

Mihalas, D. M. 1966, Ap.J.Suppl, 13, 1

Minkowski, R. 1957, I.A.U.Symposium No. 4, 107, (Cambridge: Cambridge University Press).

Minkowski, R. 1968, SGRO, Paper 1.

Morgan, W. W. 1968, Ap.J., 153, 27.

Morgan, W. W., Smith, H. J., and Weedman, D. 1968, Ap.J., 152, L113.

Munch, G. 1948, Ap.J., 108, 116.

Naqvi, A. M., and Talwar, S. P. 1957, M.N., 117, 463.

O'Dell, C. R. 1965, Ap.J., 142, 1093.

Oke, J. B. 1960, Ap.J., 131, 358.

———— 1964, ibid., 140, 689.

Oke, J. B. 1965a, Ann.Rev.Astr.and Ap., 3, 23.

Oke, J. B. 1965b, Ap.J., 141, 10.

———— 1967, private communication

Oke, J. B., and Sargent, W. L. W. 1968, Ap.J., 151, 807.

Oke, J. B., and Visvanathan, N. 1968, see: Visvanathan and Oke.

Osterbrock, D. E. 1964, Ann.Rev.Astr.and Ap., 2, 95.

Osterbrock, D. E., and Parker, R. A. 1965, Ap.J., 141, 892.

Pacholczyk, A. G., and Wisniewski, W. A. 1967, Ap.J., 147, 394.

Pacholczyk, A. G., and Weymann, R. J. 1968a, SGRO, Paper 6.

———— ———— 1968b, ibid. Paper 18.

Page, T. L. 1952, Ap.J., 116, 63.

Parker, R. A. 1964, Ap.J., 189, 202.

Pengelly, R. M. 1964, M.N.R.A.S., 127, 145.

Peterson, B. A. 1968, private communication.

Sandage, A. R. 1967, Ap.J., 150, L177.

Sargent, W. L. W. 1967, Publ.A.S.P., 79, 369.

———————— 1968, SGRO, Paper 33

Schatzman, E. 1968, SGRO, Paper 42.

Seaton, M. J. 1955a, Proc.Phys.Soc.London. Ser. 4., 68, 457.

———————— 1955b, M.N.R.A.S., 115, 279.

———————— 1960, Repts.Progr.in Phys., 23, 313.

Seaton, M. J., and Osterbrock, D. E. 1957, Ap.J., 125, 66.

Sersic, J. L. 1957, Observatory, 77, 146.

Seyfert, C. K. 1943, Ap.J., 97, 28.

Shane, et.al. 1959, A.J., 64, 197; Lick Obs. Bull., 542.

Shakhovski, I. S. 1965, Soviet Astr.-AJ, 9, 683.

Slipher, V. M. 1917, Proc.Amer.Phil.Soc., 56, 403; Pop.Astr., 25, 36.

Smith, H., Weedman, D., and Morgan, W. W. 1968, see: Morgan, Smith, and Weedman.

Souffrain, S. 1968, SGRO, Paper 36.

Spitzer, L. 1948, Ap.J., 107, 6.

Spitzer, L., and Greenstein, J. L. 1951, Ap.J., 114, 407.

Strömgren, B. 1939, Ap.J., 89, 526.

Sturrock, P.A. and Feldman, P.A. 1968, SGRO, Paper 43.

Visvanathan, N. 1968 private communication.

Visvanathan, N., and Oke, J. B. 1968, Ap.J., 152, L165.

Walker, M. F. 1968a, Ap.J., 151, 71.

———————— SGRO, Paper 9, 1968b.

Westerlund, B. E., and Wall, J. V. 1968, SGRO, Paper 26.

Westfold, K. C. 1959, Ap.J., 130, 241.

Weymann, R. J., and Williams, R. E. 1968, SGRO, Paper 35

Whitford, A. 1958, Ap.J., 63, 201.

Williams, R. E. 1967, Ap.J., 147, 556.

Williams, R. E. and Weymann, R. J. 1968, see: Weymann and Williams.

Woltjer, L. 1959, Ap.J., 130, 38.

Zwicky, F. 1964, Ap.J., 140, 1467.

———— 1966, ibid., 143, 192.

Table 1: General properties of the Seyfert galaxies. Values followed by (N) refer to the Seyfert nucleus. The distance d is obtained from v_r using H = 100 km/sec Mpc. unless otherwise noted. P_v is the fraction of the total visual light arising from the nucleus.

Object	Type	Sp	v_r	d Mpc.	m_{pg}	V	B	m_{pg}(N)	v(N)	B(N)	p_v %	α (1960) h m	δ (1960) o '
NGC 1068 3C71, M77	Sb	F0 G3	+1032	10.3	9.9	8.91	9.7	13.0	11.9	12.4	6	02 41	-00 19
NGC 1275 3C84,Per A	Irr	A[2] G3	+5293	52.9	11.0	12.3	13:	15.5	15.0		8	03 18	+41 24
NGC 3227	Sb	F3	+1006	10.1	11.3	10.9	11.5	13.8[8]	14.3[8]		4	10 22	+20 02
NGC 3516	Sb0	F0 G2	+2770	27.7	12.7	12.1	12.6	13.7	13.2	14.7	36	11 05	+72 45
NGC 4051	Sa	A5 G2	+679	5.2[5]	11.0	10.2	10.8	14.0	13.7	14.5	4	12 01	+44 43
NGC 4151	Sa	A8 G2	+990	9.9	11.2	10.5	11.2	12.0	11.5	12.4	40	12 09	+39 36
NGC 4258 M 108	Sb	G0	+494	6.6[6]	9.0							12 17	+47 30
NGC 5548	Sa	F5	+4990	49.9	12.8	12.9	13.1		14:[7]		36	14 16	+25 18
NGC 6814	Sb	F0	+1590	15.9	12.2		12.1					19 41	-10 24
NGC 7469	Sa	F5 G0	+4988	49.9	12.7	12.0	12.8	14.3	14.6		9	23 02	+08 42
Ref.		1 1 3	1		1	2	3	4	2	3			

References:

1. Humason, Mayall, & Sandage (1956)
2. Minkowski (1968)
3. deVaucouleurs & deVaucouleurs (1968)
4. Seyfert (1943)
5. Chester & Roberts (1964)
6. Burbidge, Burbidge & Prendergast (1959)
7. Dibai , Esipov, and Pronik (1968)
8. Dibai & Pronik (1968)

Table 2: Standard deviation of grey corrections about the mean. (zero point uncertainty)

Object	λ3300-λ6055 Scans	σ_{rms}	λ4785-λ8400 Scans	σ_{rms}
NGC 1068	6	0.015	6	0.022
NGC 1275	4	0.021	7	0.048
NGC 3227	8	0.029	10	0.028
NGC 3516	6	0.011	6	0.094
NGC 4051	6	0.065	4	0.094
NGC 4151	4	0.041	6	0.029
NGC 4258	7	0.025	5	0.031
NGC 5548	8	0.035	6	0.122
NGC 6814	8	0.194	10	0.070
NGC 7469	7	0.038	6	0.039

Table 3a: The continuous energy distribution of NGC 1068
(50Å bandpass, V_r = +1020 km/sec, csc b = 1.27)

Observed			Corrected			
λ'	μ'	-log f'	λ	μ	-log f	σ
3390	2.950	24.773	3379	2.960	24.622	0.011
3441	2.906	24.334	3429	2.916	24.184	0.008
3448	2.900	24.414	3436	2.910	24.265	0.008
3509	2.850	24.740	3497	2.860	24.593	0.012
3571	2.800	24.725	3559	2.810	24.580	0.010
3636	2.750	24.686	3624	2.760	24.543	0.015
3680	2.717	24.695	3668	2.727	24.553	0.008
3704	2.700	24.690	3691	2.709	24.549	0.007
3727	2.683	24.469	3714	2.692	24.328	0.007
3862	2.589	24.630	3849	2.598	24.493	0.009
4032	2.480	24.509	4018	2.489	24.376	0.013
4070	2.457	24.463	4056	2.465	24.331	0.027
4101	2.438	24.431	4087	2.447	24.300	0.018
4167	2.400	24.512	4153	2.408	24.383	0.000
4255	2.350	24.444	4241	2.358	24.317	0.003
4290	2.331	24.430	4275	2.339	24.303	0.016
4315	2.317	24.478	4300	2.325	24.352	0.020
4340	2.304	24.363	4325	2.312	24.237	0.003
4350	2.299	24.328	4335	2.307	24.203	0.009
4365	2.291	24.294	4350	2.299	24.169	0.010
4464	2.240	24.362	4449	2.248	24.239	0.011
4566	2.190	24.320	4551	2.198	24.200	0.000
4600	2.174	24.294	4584	2.181	24.176	0.005
4686	2.134	24.270	4670	2.141	24.154	0.013
4777	2.093	24.246	4761	2.707	24.133	0.021
4785	2.090	24.263	4769	2.097	24.150	0.005
4800	2.083	24.243	4784	2.090	24.131	0.005
4824	2.073	24.190	4808	2.080	24.078	
4850	2.062	24.150	4834	2.069	24.039	
4860	2.058	24.124	4844	2.065	24.013	0.008
4870	2.053	24.142	4853	2.060	24.032	0.013
4900	2.041	24.130	4883	2.048	24.027	0.014
4910	2.037	24.094	4893	2.044	23.985	0.000
4950	2.020	23.924	4933	2.027	23.816	0.010
4970	2.012	23.766	4953	2.019	23.659	
5000	2.000	23.544	4983	2.007	23.437	0.017
5009	1.996	23.504	4992	2.003	23.398	
5050	1.980	23.528	5033	1.987	23.423	0.000
5080	1.969	23.802	5063	1.975	23.698	0.032
5100	1.961	24.208	5083	1.967	24.104	0.007
5263	1.900	24.160	5245	1.907	24.060	0.008
5400	1.852	24.122	5382	1.858	24.026	0.013
5500	1.818	24.104	5481	1.824	24.010	
5556	1.800	24.086	5537	1.806	23.993	0.001
5600	1.786	24.070	5581	1.792	23.978	0.020

(Table 3a, continued)

Observed			Corrected			
λ'	μ'	-log f'	λ	μ	-log f	σ
5680	1.767	24.054	5667	1.767	23.964	0.003
5840	1.712	24.031	5820	1.718	23.944	0.003
5882	1.700	24.006	5862	1.706	23.920	
6055	1.652	24.008	6034	1.657	23.925	0.000
6370	1.570	23.935	6348	1.575	23.858	0.010
6420	1.558	23.943	6398	1.563	23.867	0.011
6436	1.554	23.960	6414	1.559	23.884	
6470	1.546	23.943	6448	1.551	23.868	0.007
6520	1.534	23.918	6498	1.539	23.843	0.006
6560	1.524	23.427	6538	1.530	23.353	0.001
6570	1.522	23.327	6548	1.527	23.253	0.005
6580	1.520	23.277	6558	1.525	23.137	0.011
6600	1.515	23.175	6578	1.520	23.102	0.003
6620	1.511	23.372	6598	1.516	23.299	0.009
6640	1.506	23.766	6617	1.511	23.693	0.012
6726	1.487	23.758	6703	1.492	23.687	0.017
6800	1.471	23.911	6777	1.476	23.841	0.001
7100	1.408	23.863	7076	1.413	23.797	0.005
7530	1.328	23.804	7504	1.333	23.743	0.010
7550	1.325	23.820	7524	1.329	23.760	
7780	1.285	23.776	7754	1.290	23.718	0.015
7850	1.274	23.777	7823	1.278	23.720	0.032
8080	1.238	23.764	8053	1.242	23.710	0.016
8090	1.236	23.768	8063	1.240	23.714	
8370	1.195	23.736	8342	1.199	23.685	0.000
8400	1.190	23.723	8372	1.195	23.672	0.021
8708	1.148	23.728	8678	1.152	23.690	
8805	1.136	23.707	8775	1.140	23.660	0.020

Table 3b: The continuous energy distribution of NGC 1275 (50Å bandpass, V_r = +5160 km/sec, csc b =4.44)

Observed			Corrected			
λ'	μ'	-log f'	λ	μ	-log f	σ
3390	2.950	25.299	3333	3.002	24.711	0.015
3448	2.900	25.290	3390	2.951	24.769	0.043
3509	2.850	25.279	3450	2.900	24.765	0.034
3571	2.800	25.286	3511	2.849	24.779	0.020
3636	2.750	25.272	3574	2.798	24.772	0.015
3704	2.700	25.263	3641	2.747	24.770	0.041
3727	2.683	25.249	3664	2.730	24.758	0.002
3797	2.638	24.821	3727	2.684	24.337	0.013
3800	2.632	24.829	3736	2.678	24.345	
3862	2.589	25.173	3797	2.635	24.695	0.048
3933	2.543	24.997	3866	2.587	24.526	0.030
4032	2.480	25.120	3964	2.524	24.658	0.021
4167	2.400	25.058	4096	2.442	24.607	0.016
4255	2.350	25.031	4183	2.391	24.587	0.031
4341	2.304	25.013	4268	2.344	24.575	
4350	2.299	24.937	4276	2.339	24.500	0.005
4415	2.265	24.993	4340	2.305	24.561	0.009
4464	2.240	24.981	4388	2.279	24.552	0.008
4566	2.190	24.947	4489	2.228	24.524	0.015
4785	2.090	24.871	4704	2.726	24.478	0.015
4900	2.041	24.857	4817	2.077	24.476	0.018
4944	2.023	24.793	4860	2.058	24.417	
4950	2.020	24.813	4866	2.056	24.437	0.013
5000	2.000	24.831	4975	2.035	24.460	0.026
5050	1.980	24.719	4965	2.015	24.353	0.025
5080	1.969	24.693	4994	2.003	24.330	
5094	1.963	24.613	5008	1.997	24.251	
5100	1.967	24.670	5014	1.995	24.308	0.021
5263	1.900	24.823	5174	1.933	24.823	0.005
5350	1.869	24.737	5259	1.902	24.397	0.039
5500	1.818	24.777	5407	1.850	24.450	0.022
5556	1.800	24.772	5462	1.837	24.449	0.008
5840	1.712	24.704	5741	1.742	24.402	0.037
6055	1.652	24.683	5953	7.680	24.396	0.017
6370	1.570	24.640	6262	1.597	24.372	0.019
6570	1.522	24.651	6459	1.549	24.395	0.020
6590	1.517	24.639	6478	1.544	24.384	0.020
6610	1.513	24.615	6498	1.539	24.367	0.021
6630	1.508	24.533	6518	1.535	24.280	0.014

(Table 3b, continued)

Observed			Corrected			
λ'	μ'	-log f'	λ	μ	-log f	σ
6650	1.504	24.384	6537	1.530	24.132	0.039
6670	1.499	24.214	6557	1.526	23.963	0.024
6690	1.495	24.164	6577	1.527	23.914	0.012
6674	1.498	24.238	6567	1.525	23.987	
6710	1.490	24.249	6596	1.576	24.000	0.000
6776	1.476	24.584	6667	1.502	24.339	0.017
6790	1.473	24.508	6675	1.499	24.263	0.017
6800	1.471	24.589	6685	1.496	24.345	0.019
7100	1.408	24.547	6980	1.433	24.318	0.025
7530	1.325	24.509	7422	1.348	24.300	0.024
7780	1.285	24.476	7648	1.308	24.276	
8080	1.238	24.447	7943	1.259	24.259	0.041
8090	1.236	24.457	7953	1.258	24.269	
8370	1.195	24.434	8228	1.216	24.258	
8708	1.148	24.434	8561	1.168	24.267	
9830	1.017	24.304	9664	1.035	24.169	

Table 3c: The continuous energy distribution of NGC 3227 (50Å bandpass, V_r = +1111 km/sec, csc b = 1.21)

Observed			Corrected			
λ'	μ'	-log f'	λ	μ	-log f	σ
3390	2.950	25.500	3377	2.961	25.356	0.046
3448	2.900	25.474	3435	2.911	25.332	0.049
3509	2.850	25.421	3496	2.860	25.281	0.047
3571	2.800	25.446	3558	2.811	25.308	0.021
3636	2.750	25.446	3623	2.761	25.310	0.021
3704	2.700	25.386	3690	2.710	25.252	0.016
3775	2.649	25.415	3761	2.659	25.283	0.019
3862	2.589	25.352	2848	2.599	25.222	0.012
4032	2.480	25.250	4017	2.489	25.124	0.030
4167	2.400	25.194	4152	2.409	25.071	0.015
4255	2.350	25.799	4239	2.359	25.078	0.015
4350	2.299	25.170	4334	2.307	25.057	0.017
4464	2.240	25.109	4448	2.248	24.992	0.018
4566	2.190	25.043	4549	2.198	24.930	0.016
4785	2.090	24.996	4767	2.098	24.889	0.017
4900	2.090	24.996	4882	2.048	24.778	0.013
4975	2.070	24.832	4957	2.018	24.730	0.001
5000	2.000	24.751	4982	2.007	24.650	0.021
5050	1.980	24.700	5031	1.988	24.600	0.014
5100	1.961	24.881	5081	1.968	24.782	0.020
5263	1.900	24.876	5244	1.907	24.781	0.011
5556	1.800	24.815	5535	1.807	24.727	0.007
5840	1.712	24.720	5818	1.719	24.638	0.011
6055	1.652	24.697	6033	1.658	24.619	0.009
6370	1.570	24.660	6346	1.576	24.587	0.012
6520	1.534	24.608	6496	1.539	24.537	0.017
6540	1.529	24.530	6576	1.535	24.460	0.022
6560	1.524	24.423	6536	1.530	24.353	0.026
6580	1.520	24.321	6556	1.525	24.251	0.025
6600	1.515	24.270	6576	1.521	24.200	0.040
6620	1.511	24.284	6596	1.516	24.215	0.006
6640	1.506	24.497	6615	1.512	24.428	0.024
6726	1.487	24.575	6701	1.492	24.507	0.015
6800	1.471	24.660	6775	1.476	24.593	0.036
7100	1.408	24.614	7074	1.414	24.557	0.032
7530	1.328	24.603	7502	1.333	24.546	0.044
7850	1.274	24.536	7821	1.279	24.482	0.042
8080	1.238	24.538	8050	1.242	24.487	0.055
8400	1.190	24.616	8369	1.195	24.568	0.202

Table 3d: The continuous energy distribution of NGC 3516 (50Å bandpass, V_r = +2614 km/sec, csc b = 1.49)

Observed			Corrected			
λ'	μ'	-log f'	λ	μ	-log f	σ
3448	2.900	25.199	3418	2.925	25.029	
3509	2.850	25.179	3479	2.875	25.011	0.042
3571	2.800	25.201	3540	2.825	25.035	0.043
3636	2.750	25.189	3605	2.774	25.025	0.029
3704	2.700	25.200	3672	2.724	25.039	0.049
3862	2.589	25.148	3829	2.612	24.992	0.012
4032	2.480	25.012	3997	2.502	24.861	0.018
4167	2.400	24.946	4131	2.421	24.799	0.017
4255	2.350	24.934	4218	2.371	24.789	0.013
4350	2.299	24.888	4312	2.319	24.745	0.022
4464	2.240	24.844	4425	2.260	24.704	0.019
4566	2.190	24.820	4527	2.209	24.684	0.015
4785	2.090	24.717	4744	2.108	24.589	0.009
4900	2.047	24.604	4858	2.059	24.480	0.019
4950	2.020	24.521	4907	2.038	24.498	0.008
5000	2.000	24.607	4957	2.018	24.486	0.006
5050	1.980	24.566	5006	1.998	24.447	0.042
5100	1.961	24.638	5056	1.978	24.520	0.018
5263	1.900	24.654	5218	1.9.7	24.541	0.017
5350	1.869	24.684	5304	1.886	24.573	0.045
5556	1.800	24.573	5508	1.816	24.468	0.008
5840	1.712	24.492	5790	1.727	24.394	0.011
6055	1.652	24.474	6003	1.666	24.381	0.015
6370	1.570	24.432	6315	1.584	24.345	0.010
6520	1.534	24.401	6464	1.547	24.317	0.022
6540	1.529	24.352	6483	1.543	24.268	0.018
6560	1.524	24.344	6503	1.538	24.261	0.014
6580	1.520	24.281	6523	1.533	24.198	0.009
6600	1.515	24.208	6543	1.528	24.125	0.020
6620	1.511	24.137	6563	1.524	24.055	0.007
6726	1.487	24.302	6668	1.500	24.222	0.037
6800	1.471	24.332	6741	1.484	24.253	0.014
7100	1.408	24.336	7039	1.421	24.262	0.017
7550	1.328	24.297	7465	1.340	24.229	0.025
7850	1.274	24.265	7782	1.285	24.201	0.033
8080	1.238	24.255	8010	1.249	24.194	0.132

Table 3e: The continuous energy distribution of NGC 4051 (50Å bandpass, V_r = +627 km/sec, csc b = 1.07)

Observed			Corrected			
λ'	μ'	-log f'	λ	μ	-log f	σ
3390	2.950	25.317	3383	2.956	25.190	0.029
3448	2.900	25.218	3441	2.906	25.093	0.017
3509	2.850	25.303	3502	2.856	25.180	0.043
3571	2.800	25.271	3564	2.806	25.149	0.033
3636	2.750	25.248	3628	2.756	25.128	0.035
3704	2.700	25.238	3696	2.705	25.120	0.001
3775	2.649	25.268	3767	2.655	25.151	0.000
3862	2.589	25.253	3854	2.595	25.738	0.021
4032	2.480	25.174	4024	2.485	25.063	0.016
4167	2.400	25.196	4158	2.405	25.088	0.017
4255	2.350	25.137	4246	2.355	25.030	0.005
4350	2.299	25.028	4341	2.304	24.923	0.003
4464	2.240	25.082	4455	2.245	24.979	0.013
4566	2.190	25.036	4556	2.195	24.936	0.011
4650	2.157	24.958	4640	2.155	24.860	
4785	2.090	25.019	4775	2.094	24.925	0.070
4900	2.041	24.877	4890	2.045	24.786	0.006
4975	2.010	24.842	4965	2.014	24.752	
5000	2.000	24.772	4990	2.004	24.683	0.005
5050	1.980	24.912	5039	1.984	24.824	0.017
5100	1.961	24.913	5089	1.965	24.826	0.007
5263	1.900	24.919	5252	1.904	24.836	0.018
5556	1.800	24.859	5544	1.804	24.781	0.013
5840	1.712	24.787	5828	1.716	24.714	0.019
6055	1.652	24.800	6042	1.655	24.731	0.010
6370	1.570	24.787	6357	1.573	24.722	0.009
6520	1.534	24.761	6506	1.537	24.698	0.013
6540	1.529	24.713	6526	1.532	24.651	0.009
6560	1.524	24.452	6546	1.528	24.390	0.009
6580	1.520	24.393	6566	1.523	24.331	0.019
6600	1.515	24.440	6586	1.518	24.379	0.028
6640	1.506	24.717	6626	1.509	24.656	0.019
6726	1.487	24.747	6712	1.490	24.687	0.027
6800	1.471	24.800	6786	1.474	24.741	0.023
7100	1.408	24.786	7085	1.411	24.731	0.018
7530	1.328	24.744	7514	1.221	24.693	0.016
7850	1.274	24.787	7834	1.277	24.739	0.040
8080	1.238	24.590	8063	1.240	24.544	0.063

Table 3f: The continuous energy distribution of NGC 4151 (50Å bandpass, V_r = +960 km/sec, csc b = 1.04)

Observed			Corrected			
λ'	μ'	-log f'	λ	μ	-log f	σ
3297	3.033	24.261	3286	3.043	24.135	0.024
3390	2.950	24.416	3379	2.959	24.293	0.018
3448	2.900	24.311	3437	2.910	24.189	0.009
3509	2.850	24.351	3498	2.859	24.231	0.025
3571	2.800	24.356	3560	2.809	24.238	0.022
3636	2.750	24.338	3624	2.759	24.221	0.017
3704	2.700	24.348	3692	2.708	24.233	0.019
3862	2.589	24.391	3850	2.598	24.279	0.011
4032	2.480	24.409	4019	2.488	24.301	0.026
4167	2.400	24.360	4154	2.408	24.255	0.005
4255	2.350	24.376	4241	2.358	24.272	0.014
4350	2.299	24.226	4336	2.306	24.124	0.010
4464	2.240	24.316	4450	2.247	24.216	0.004
4566	2.190	24.290	4551	2.197	24.193	0.014
4785	2.090	24.201	4770	2.097	24.109	0.002
4860	2.058	24.032	4844	2.064	23.942	0.011
4900	2.041	23.919	4884	2.047	23.830	0.004
4950	2.020	24.089	4934	2.027	24.001	0.007
5000	2.000	23.810	4984	2.006	23.723	0.004
5050	1.990	23.556	5034	1.987	23.470	0.009
5100	1.961	24.150	5084	1.967	24.065	0.012
5263	1.900	24.144	5246	1.906	24.063	0.003
5350	1.869	24.096	5333	1.875	24.017	0.004
5556	1.800	24.102	5538	1.806	24.026	0.016
5840	1.712	24.036	5821	1.718	23.965	0.019
6055	1.652	24.039	6036	1.657	23.972	0.011
6370	1.570	23.985	6350	1.575	23.922	0.006
6520	1.534	23.798	6499	1.539	23.737	0.007
6540	1.529	23.643	6519	1.534	23.583	0.013
6560	1.524	23.461	6539	1.529	23.401	0.021
6580	1.520	23.251	6559	1.525	23.191	0.019
6600	1.515	23.246	6579	1.520	23.186	0.014
6620	1.511	23.438	6599	1.515	23.379	0.023
6640	1.506	23.668	6619	1.511	23.609	0.016
6726	1.487	23.824	6705	1.492	23.766	0.012
6800	1.471	23.976	6778	1.475	23.9.9	0.019
7100	1.408	23.951	7077	1.413	23.897	0.031
7530	1.328	23.912	7506	1.332	23.863	0.039
7850	1.274	23.890	7825	1.278	23.844	0.033
8080	1.238	23.862	8054	1.242	23.818	0.042
8400	1.190	23.841	8373	1.794	23.799	0.043

Table 3g: The Continuous energy distribution of NGC 4258 (50Å bandpass, V_r = +420 km/sec, csc b = 1.07)

Observed			Corrected			
λ'	μ'	-log f'	λ	μ	-log f	σ
3390	2.950	25.258	3385	2.954	25.130	0.051
3448	2.900	25.134	3443	2.904	25.007	0.054
3509	2.850	25.212	3504	2.854	25.087	0.034
3571	2.800	25.207	3566	2.804	25.084	0.057
3636	2.750	25.088	3631	2.754	24.966	0.038
3704	2.700	25.086	3699	2.704	24.966	0.045
3862	2.589	25.076	3857	2.593	24.960	0.028
4032	2.480	24.822	4026	2.484	24.709	0.025
4167	2.400	24.806	4161	2.403	24.696	0.014
4255	2.350	24.767	4249	2.353	24.659	0.026
4350	2.299	24.756	4344	2.302	24.649	0.033
4464	2.240	24.635	4458	2.243	24.530	0.024
4566	2.190	24.636	4560	2.193	24.534	0.041
4785	2.090	24.519	4778	2.093	24.423	0.009
4850	2.062	24.496	4843	2.065	24.402	0.020
4900	2.041	24.506	4893	2.044	24.413	0.019
4950	2.020	24.510	4943	2.023	24.418	0.064
5000	2.000	24.498	4993	2.003	24.407	0.028
5050	1.980	24.488	5043	1.983	24.399	0.021
5100	1.961	24.470	5093	1.964	24.388	0.015
5263	1.900	24.437	5256	1.903	24.352	0.015
5350	1.869	24.410	5343	1.872	24.327	0.019
5556	1.800	24.431	5548	1.802	24.352	0.028
5840	1.712	24.328	5832	1.715	24.254	0.008
6055	1.652	24.284	6047	1.654	24.214	0.013
6370	1.570	24.249	6361	1.572	24.183	0.009
6520	1.534	24.251	6511	1.536	24.187	0.009
6540	1.529	24.212	6531	1.531	24.149	0.021
6560	1.524	24.206	6551	1.527	24.143	0.003
6580	1.520	24.172	6571	1.522	24.109	0.011
6600	1.515	24.211	6591	1.517	24.148	0.025
6620	1.511	24.238	6611	1.513	24.176	0.012
6640	1.506	24.204	6631	1.500	24.142	0.006
6726	1.487	24.148	6717	1.489	24.087	0.019
6800	1.471	24.196	6790	1.473	24.136	0.016
7100	1.408	24.168	7090	1.410	24.112	0.015
7530	1.328	24.054	7519	1.330	24.002	0.017
7850	1.274	24.015	7839	1.276	23.966	

Table 3h: The continuous energy distribution of NGC 5548 (50Å bandpass, V_r = +4930 km/sec, csc b = 1.06)

Observed			Corrected			
λ'	μ'	-log f'	λ	μ	-log f	σ
3390	2.950	24.979	3335	2.999	24.857	0.030
3448	2.900	25.045	3392	2.949	24.925	0.022
3509	2.850	24.996	3452	2.897	24.878	0.023
3571	2.800	25.021	3513	2.847	24.904	0.030
3636	2.750	24.986	3577	2.796	24.871	0.022
3704	2.700	25.006	3644	2.745	24.893	0.016
3775	2.649	25.055	3714	2.693	24.943	0.003
3862	2.589	25.148	3800	2.633	25.038	0.021
4032	2.480	25.084	3967	2.522	24.978	0.014
4167	2.400	25.098	4100	2.440	24.995	0.009
4255	2.350	25.133	4186	2.389	25.031	0.009
4350	2.299	25.111	4280	2.337	25.011	0.007
4464	2.240	25.031	4392	2.278	24.933	0.014
4566	2.190	25.041	4492	2.227	24.946	0.014
4785	2.090	24.990	4708	2.125	24.901	0.013
4900	2.041	24.873	4821	2.075	24.787	0.022
4975	2.010	24.884	4895	2.044	24.799	0.003
5000	2.000	24.881	4919	2.033	24.797	0.024
5050	1.980	24.817	4968	2.013	24.734	0.015
5100	1.961	24.644	5017	1.994	24.562	0.005
5175	1.932	24.969	4091	1.965	24.889	0.018
5263	1.900	25.013	5178	1.932	24.935	0.025
5350	1.869	24.970	5263	1.900	24.894	0.006
5556	1.800	24.950	5466	1.830	24.886	0.024
5840	1.712	24.891	5746	1.741	24.824	0.008
6055	1.652	24.871	5957	1.679	24.807	0.027
6370	1.570	24.792	6267	1.596	24.733	0.016
6520	1.534	24.756	6415	1.559	24.699	0.023
6540	1.529	24.770	6434	1.555	24.713	0.020
6560	1.524	24.732	6454	1.550	24.675	0.022
6580	1.520	24.648	6474	1.545	24.592	0.021
6600	1.515	24.521	6493	1.540	24.465	0.031
6620	1.511	24.296	6513	1.536	24.240	0.041
6640	1.506	24.236	6533	1.531	24.181	0.002
6660	1.502	24.161	6552	1.527	24.106	0.005
6726	1.487	24.512	6617	1.512	24.458	0.031
6800	1.471	24.791	6690	1.495	24.738	0.067
7100	1.408	24.745	6985	1.432	24.695	0.022
7530	1.328	24.700	7408	1.350	24.655	0.048
7850	1.274	24.685	7723	1.295	24.642	0.063
8080	1.238	24.625	7949	1.258	24.585	0.123

Table 3i: The continuous energy distribution of NGC 6814 (50Å bandpass, V_r = +1437 km/sec, csc b = 3.63)

Observed			Corrected			
λ'	μ'	-log f'	λ	μ	-log f	σ
3390	2.950	25.659	3374	2.964	25.249	0.116
3448	2.900	25.568	3432	2.914	25.163	0.213
3509	2.850	25.729	3452	2.864	25.330	0.128
3571	2.800	25.686	3554	2.814	25.292	0.163
3636	2.750	25.621	3619	2.764	25.232	0.153
3704	2.700	25.716	3686	2.713	25.333	0.083
3745	2.670	25.763	3727	2.683	25.383	
3862	2.589	25.750	3844	2.602	25.379	0.076
4032	2.480	25.564	4013	2.492	25.205	0.057
4167	2.400	25.588	4147	2.411	25.237	0.104
4255	2.350	25.605	4235	2.361	25.260	0.063
4350	2.299	25.398	4329	2.310	25.058	0.082
4464	2.240	25.240	4443	2.251	24.906	0.056
4566	2.190	25.380	4544	2.201	24.956	0.053
4785	2.090	25.192	4762	2.100	24.886	0.053
4860	2.058	25.160	4837	2.068	24.866	0.074
4900	2.041	25.141	4877	2.051	24.844	0.091
4950	2.020	25.194	4926	2.030	24.901	0.083
5000	2.000	25.115	4976	2.101	24.826	0.045
5050	1.980	25.076	4026	1.980	24.797	0.046
5100	1.961	25.177	5076	1.970	24.895	0.062
5150	1.942	25.031	5125	1.951	24.753	0.004
5263	1.900	25.141	5238	1.909	24.870	0.043
5350	1.869	25.074	5324	1.878	24.809	0.072
5556	1.800	24.997	5529	1.809	24.745	0.036
5840	1.712	24.934	5812	1.721	24.698	0.028
6055	1.652	24.903	6026	1.659	24.678	0.023
6370	1.570	24.791	6340	1.577	24.581	0.019
6520	1.534	24.764	6489	1.541	24.561	0.017
6540	1.529	24.764	6509	1.536	24.562	0.040
6560	1.524	24.661	6529	1.532	24.460	0.025
6580	1.520	24.605	6549	1.527	24.404	0.037
6600	1.515	24.443	6569	1.522	24.353	0.029
6640	1.506	24.700	6608	1.513	24.502	0.056
6726	1.487	24.757	6694	1.494	24.563	0.046
6800	1.471	24.736	6768	1.478	24.545	0.055
7100	1.408	24.752	7066	1.415	24.572	0.057
7530	1.328	24.580	7494	1.334	24.415	0.120
7850	1.274	24.575	7813	1.280	24.420	0.083
8080	1.238	24.537	8041	1.244	24.388	0.081

Table 3j: The continuous energy distribution of NGC 7469 (50Å bandpass, V_r = +4780 km/sec, csc b = 1.41)

Observed			Corrected			
λ'	μ'	-log f'	λ	μ	-log f	σ
3390	2.950	24.958	3337	2.998	24.795	0.051
3448	2.900	24.978	3394	2.947	24.817	0.046
3509	2.850	24.952	3454	2.896	24.793	0.043
3571	2.800	24.978	3515	2.846	24.821	0.020
3636	2.750	24.965	3579	2.795	24.810	0.032
3709	2.700	25.035	3646	2.744	24.883	0.057
3862	2.589	25.052	3801	2.631	24.905	0.009
4032	2.480	25.018	3969	2.520	24.875	0.024
4167	2.400	24.953	4102	2.439	24.814	0.018
4255	2.350	25.037	4188	2.388	24.900	0.021
4350	2.299	25.035	4282	2.336	24.901	0.025
4464	2.246	24.952	4394	2.276	24.820	0.013
4566	2.190	24.918	4494	2.226	24.790	0.016
4785	2.090	24.860	4710	2.124	24.740	0.014
4900	2.041	24.863	4823	2.074	24.746	0.020
4950	2.020	24.656	4872	2.053	24.541	0.017
5000	2.000	24.804	4922	2.032	24.691	0.008
5050	1.980	24.710	4971	2.012	24.598	0.032
5100	1.961	24.548	5020	1.993	24.438	0.024
5150	1.942	24.844	5069	1.973	24.735	0.003
5263	1.900	24.782	5180	1.931	24.676	0.021
5350	1.869	24.822	5266	1.899	24.719	0.055
5556	1.800	24.782	5469	1.829	24.684	0.013
5840	1.712	24.783	5748	1.440	24.692	0.015
6055	1.652	24.684	5960	1.678	24.597	0.014
6376	1.570	24.598	6270	1.595	24.517	0.070
6520	1.534	24.668	6418	1.559	24.590	0.017
6540	1.529	24.661	6437	1.554	24.583	0.022
6560	1.524	24.641	6457	1.549	24.564	0.004
6580	1.520	24.628	6477	1.544	24.551	0.018
6600	1.515	24.572	6496	1.540	24.496	0.017
6620	1.511	24.468	6516	1.535	24.392	0.007
6640	1.506	24.262	6536	1.530	24.186	0.026
6660	1.502	23.965	6555	1.526	23.890	0.008
6680	1.497	23.910	6575	1.521	23.835	
6700	1.493	24.105	6595	1.517	24.030	0.030
6726	1.487	24.437	6620	1.511	24.363	0.018
6800	1.471	24.546	6693	1.494	24.473	0.007
7100	1.408	24.548	6989	1.431	24.480	0.029
7530	1.328	24.451	7412	1.350	24.389	0.077
7850	1.274	24.517	7727	1.295	24.459	0.052
8080	1.238	24.465	7953	1.258	24.410	0.032

Table 4: The flux distribution for a "normal elliptical" or the nuclear region of a normal spiral for a 50Å bandpass. This distribution is based upon the nuclear distribution of NGC 224 (M 31) obtained by Oke (1967). The "observed" values correspond to csc b = 1, the corrected values to csc b = 0. The common zero-point of the log s_o' and log s_o scales is arbitrary.

λ	μ	Observed log s_o'	Corrected log s_o
3390	2.950	0.281	0.401
3448	2.900	0.366	0.485
3509	2.850	0.361	0.478
3571	2.800	0.344	0.460
3636	2.750	0.478	0.592
3704	2.700	0.500	0.613
3862	2.589	0.476	0.583
4032	2.480	0.865	0.971
4167	2.400	0.848	0.951
4255	2.350	0.964	1.066
4350	2.299	1.009	1.109
4464	2.240	1.108	1.206
4566	2.190	1.181	1.276
4785	2.090	1.247	1.337
4860	2.058	1.258	1.346
4900	2.041	1.284	1.371
4950	2.020	1.309	1.395
5000	2.000	1.269	1.354
5050	1.980	1.288	1.372
5080	1.969	1.290	1.373
5150	1.942	1.262	1.344
5263	1.900	1.358	1.438
5350	1.869	1.405	1.483
5556	1.800	1.439	1.513
5840	1.712	1.522	1.592
6055	1.652	1.571	1.637
6370	1.570	1.574	1.638
6560	1.524	1.626	1.685
6600	1.515	1.645	1.704
6726	1.487	1.641	1.698
7100	1.408	1.689	1.742
7530	1.328	1.761	1.810
7850	1.274	1.783	1.829
8080	1.238	1.802	1.846
8400	1.190	1.821	1.862
8805	1.136	1.845	1.884

Table 5: Relative emission line intensities. $I(H_\beta) = 10.0$. The values in parentheses have been corrected for reddening.

Ion	λ	NGC 1068		NGC 1275		NGC 3227		NGC 3516	
NeV	3425.8	9.0	(9.9)	16.	(22.1)	2.9	(3.2)	2.7	(3.0)
OIII	3444.1	<0.6	(0.7)	<0.8	(1.1)				
OII	3726.0	8.3	(8.9)	26.0	(33.3)	9.0	(9.6)	2.7	(2.9)
OII	3728.8								
NeIII	3868.7	7.5	(8.0)	6.6	(8.2)	3.3	(3.5)	3.8	(4.1)
Hζ	3888.9	<0.6	(0.6)					0.6	(0.6)
NeIII	3967.5	1.8	(1.9)	1.8	(2.2)	1.0	(1.1)	1.1	(1.2)
Hε	3970.1								
SII	4068.6	1.4	(1.5)	2.9	(3.5)	0.8	(0.8)	1.2	(1.3)
SII	4076.3								
Hδ	4101.7	1.4	(1.5)	1.8	(2.1)	2.9	(3.0)	2.7	(2.9)
Hγ	4340.4	3.2	(3.3)	4.1	(4.7)	4.7	(4.9)	4.3	(4.5)
OIII	4363.2	2.8	(2.9)	3.3	(3.7)	<0.8	(0.8)	0.6:	(0.6)
HeII	4685.7	3.7	(3.7)	1.7:	(1.8)	<0.8	(0.8)	2.0:	(2.0)
AIV	4711.3	1.5	(1.5)	<0.6	(0.6)				
AIV	4740.2	1.2	(1.2)	<0.6	(0.6)				
Hβ	4861.3	10.0		10.0		10.0		10.0	
OIII	4958.9	42.0	(41.7)	8.4	(8.2)	10.0	(9.9)	4.9	(4.9)
OIII	5006.9	129.	(128.)	24.6	(23.8)	25.0	(24.8)	14.2	(14.0)
FeVII	5158.9	<0.6	(0.6)						
NI	5198.0	2.9	(2.8)						
FeVII	5721.1	1.5:	(1.4)						
NII	5754.6	1.5	(1.4)		(1.0)				
HeI	5875.6	2.2	(2.1)						
FeVII	6085.3	2.0	(1.9)						
OI	6300.3	6.2	(5.8)	18.0	(14.0)	3.0	(2.8)		
OI	6363.8	2.0	(1.9)	5.0:	(3.8)	1.2	(1.1)		
NII	6548.1	26.	(23.9)	4.	(3.0)	21.4	(19.8)	2.3	(2.1)
Hα	6562.8	126.	(116.)	48	(36.0)	168.	(155.)	36.	(32.6)
NII	6583.4	68.	(62.5)	12.	(9.0)	62.0	(57.2)	6.2	(5.6)
SII	6716.5	28.	(25.6)	25.	(18.4)				
SII	6730.7								
OII	7319.2	4.0	(3.6)		(<1.0)				
OII	7330.2								

Table 5 (continued): Relative emission line intensities.

Ion	λ	NGC 4051		NGC 4151		NGC 5548		NGC 7469	
NeV	3425.8	3.9	(4.2)	3.4	(3.7)	2.8	(3.0)	1.8	(2.0)
OIII	3444.1	3.7	(4.0)	<0.6	(<0.6)	1.3:	(1.4)	<0.5	(0.6)
OII	3726.0	2.9	(3.1)	4.5	(4.8)	1.7	(1.8)	1.3	(1.4)
OII	3728.8								
NeIII	3868.7	2.4	(2.5)	3.0	(3.2)	3.1	(3.3)	<0.7	(0.7)
Hζ	3888.9	0.8	(0.8)	0.6	(0.6)			<1.0	(1.1)
NeIII	3967.5	0.7	(0.7)	1.0	(1.0)	1.3	(1.4)	1.4	(1.5)
Hε	3970.1								
SII	4068.6	0.8	(0.8)	0.8	(0.8)				
SII	4076.3								
Hδ	4101.7	2.2	(2.3)	1.4	(1.5)	3.7	(3.9)	2.8	(3.0)
Hγ	4340.4	4.8	(4.9)	3.5	(3.6)	6.6	(6.8)	5.5	(5.7)
OIII	4363.2	1.5	(1.5)	1.0	(1.0)	0.7	(0.7)	0.9	(0.9)
HeII	4685.7	2.3	(2.3)	2.0	(2.0)				
AIV	4711.3			<0.5	(0.5)				
AIV	4740.2			<0.5	(0.5)				
Hβ	4861.3	10.0		10.0		10.0		10.0	
OIII	4958.9	2.9	(2.9)	6.9	(6.9)	3.7	(3.7)	2.8	(2.8)
OIII	5006.9	8.5	(8.4)	22.7	(22.7)	10.7	(10.6)	7.9	(7.8)
FeVII	5158.9			<0.6	(0.6)				
NI	5198.0			<0.6	(0.6)				
FeVII	5721.1			0.8:	(0.8)				
NII	5754.6	<0.7	(0.7)	0.4:	(0.4)		(1.0)		(<1.0)
HeI	5875.6			0.5:	(0.5)				
FeVII	6085.3			0.8	(0.8)				
OI	6300.3	4.6	(4.3)	2.0	(1.9)				
OI	6363.8	3.1	(2.9)	0.7:	(0.7)				
NII	6548.1	3.1	(2.9)	1.5	(1.4)	1.0	(0.9)	4.	(3.7)
Hα	6562.8	75.	(69.9)	38.7	(36.1)	35.	(32.7)	63	(57.5)
NII	6583.4	7.9	(7.4)	3.0	(2.8)	2.5	(2.3)	12.	(10.9)
SII	6716.5	6.4	(5.9)	6.5	(6.0)				
SII	6730.7								
OII	7319.2			2.0	(1.8)		(<1.0:)		
OII	7330.2								

Table 6: The H_β intensities: W_β is the measured equivalent width, and I_w the corresponding absolute intensity. I_s is the intensity obtained from the photoelectric data alone. The corrected values are obtained by applying the reddening correction to the observed values and multiplication by $4\pi d^2$. The values given from other sources should be multiplied by the same power of ten as the adopted value.

		Observed erg/cm^2 sec		Corrected erg/sec		Adopted erg/sec	Other sources
Object	W_β(Å)	I_w	I_s	I_w	I_s	I_β	
NGC 1068	15 (15[1])	1.1×10^{-12}	2.1×10^{-12}	1.8×10^{40}	3.4×10^{40}	2.3×10^{40}	0.5[1], 1.8[3], 1.8[4], 59[5]
NGC 1275	18 (18[1])	3.1×10^{-13}	1.8×10^{-12}	2.5×10^{41}	1.5×10^{41}	2.2×10^{41}	0.18[1]
NGC 3227	20 (20[1])	2.7×10^{-13}	1.9×10^{-13}	4.2×10^{39}	2.9×10^{39}	3.8×10^{39}	
NGC 3516	20 (20[1])	3.0×10^{-13}	3.8×10^{-13}	3.8×10^{39}	4.7×10^{39}	4.1×10^{39}	8.0[1]
NGC 4051	27 (25[1])	2.7×10^{-13}	2.6×10^{-13}	1.1×10^{39}	1.0×10^{39}	1.1×10^{39}	1.0[1]
NGC 4151	85 (88[2])	6.7×10^{-12}	6.1×10^{-12}	9.7×10^{40}	8.9×10^{40}	9.4×10^{40}	7.4[2]
NGC 5548	35 (30[1])	4.1×10^{-13}	6.7×10^{-13}	1.5×10^{41}	2.5×10^{41}	1.8×10^{41}	.65[1]
NGC 7469	40 (35[1])	7.1×10^{-13}	1.1×10^{-12}	2.8×10^{41}	4.2×10^{41}	3.3×10^{41}	

References:

1. Dibai & Pronik (1965)
2. Oke & Sargent (1968)
3. Osterbrock & Parker (1965)
4. Pacholczyk & Weymann (1968 b)
5. Woltjer (1959)

Table 7: Components of the emission line profiles.

Object	Δv_C (km/sec)	Δv_B (km/sec)	Δv_W (km/sec)	f_C	f_B	f_W	Notes
NGC 1068	$\pm$1800			1.00			a
NGC 1275	$\pm$400	$\pm$1700	$\pm$2700	0.17	0.54	0.29	
NGC 3227	$\pm$800	$\pm$1200	$\pm$5000	0.47	0.24:	0.29:	b
NGC 3516	$\pm$500	$\pm$1250	$\pm$5000	0.62	0.38		c
NGC 4051	$\pm$500	$\pm$750	$\pm$2500	0.21	0.02	0.77	
NGC 4151	$\pm$600		$\pm$5500	0.21		0.79	
NGC 5548	$\pm$750	$\pm$1000	$\pm$5000	0.20	0.04	0.76	
NGC 7469	$\pm$1000	$\pm$1250	$\pm$4500	0.14	0.03	0.83	

Notes:

a. Balmer profiles essentially identical to forbidden line profiles.
b. Balmer lines are asymmetrical.
c. No core observed in Balmer lines: $f_C \leq 0.15$.

Table 8: Relative Balmer line intensities corrected for reddening. The observed intensities are given in parentheses. All intensities are normalized to $I(H_\beta) = 1.00$.

OBJECT	$I(H_\alpha)$	$I(H_\beta)$	$I(H_\gamma)$	$I(H_\delta)$	$I(H_\epsilon)$	$I(H_\zeta)$
NGC 1068	11.6 (12.6)	1.00 (1.00)	0.33 (0.32)	0.15 (0.14)	<0.19 (<0.18)	<0.06 (<0.06)
NGC 1275	3.6 (4.8)	1.00 (1.00)	0.47 (0.41)	0.21 (0.18)	<0.22 (<0.18)	<0.07 (<0.06)
NGC 3227	15.5 (16.8)	1.00 (1.00)	0.49 (0.47)	0.30 (0.29)	<0.11 (<0.10)	<0.06 (<0.05)
NGC 3516	3.3: (3.6:)	1.00: (1.00:)	0.45: (0.43:)	0.29: (0.27:)	<0.12 (<0.11)	<0.06 (<0.06)
NGC 4051	7.0: (7.5:)	1.00 (1.00)	0.49 (0.48)	0.23 (0.22)	<0.07 (<0.07)	<0.08 (<0.08)
NGC 4151	3.6 (3.9)	1.00 (1.00)	0.36 (0.35)	0.15 (0.14)	<0.10 (<0.10)	0.06: 0.06:
NGC 5548	3.3 (3.5)	1.00 (1.00)	0.68 (0.66)	0.39 (0.37)	<0.14 (<0.13)	<0.06 (<0.06)
NGC 7469	5.8 (6.3)	1.00 (1.00)	0.57 (0.55)	0.30 (0.28)	<0.15 (<0.14)	<0.11 (<0.10)
Case A:						
10,000 °K	1.91 (2.48)	1.00 (1.00)	0.59 (0.51)	0.38 -	0.26 -	0.18 -
20,000 °K	1.99 (2.36)	1.00 (1.00)	0.57 (0.51)	0.36 -	0.24 -	0.17 -
Case B:						
10,000 °K	2.71 (2.62)	1.00 (1.00)	0.51 (0.49)	0.30 -	0.19 -	0.13 -
20,000 °K	2.79 (2.53)	1.00 (1.00)	0.49 (0.49)	0.28 -	0.18 -	0.12 -

Table 9: Helium ion abundances.

(Case B: $T_e \approx 2 \times 10^4$ °K)

Object	$\frac{I(\lambda 5876)}{I(\lambda 4861)}$	$\frac{I(\lambda 4686)}{I(\lambda 4861)}$	$\frac{n(He^+)}{n(H^+)}$	$\frac{n(He^{++})}{n(H^+)}$
NGC 1068	0.21	0.37	0.21	0.05
NGC 1275		0.18		0.02
NGC 3227		<0.08		<0.01
NGC 3516		0.20		0.03
NGC 4051		0.23		0.03
NGC 4151	0.05	0.20	0.05	0.03
NGC 5548				
NGC 7469				
Mean			0.13 ± 0.08	0.03 ± 0.01

Table 10: $\mathcal{E} = n_e^2 V$ as indicated by the recombination spectrum. S is the effective emission diameter.

Object	$f_+ \times 10^{27}$	$f_- \times 10^{27}$	$\Delta r \times 10^{27}$	$\Delta R \times 10^{-25}$	$\mathcal{E}_B \times 10^{-64}$	$\mathcal{E}_\beta \times 10^{-64}$	$\mathcal{E} \times 10^{-64}$	$S \times 10^{-18}$
NGC 1068	207.	197.	9.3	17.	10.	24.	10.	7.
NGC 1275	53.5	53.5	=2.5	≦270.	≦330.	330.	330.	0.4
NGC 3227	35.8:	33.7:	2.2:	3.7:	3.8:	5.2	3.2	9.
NGC 3516	63.6	63.6	≦2.7	≦3.7	≦45.	6.2	6.0	11.
NGC 4051	56.5	50.9	5.6	2.4	2.8	1.7	2.8	5.
NGC 4151	45.5	303.	152.	234.	280.	140.	280	15.
NGC 5548	98.5	64.6	34.	1330.	1600.	270.	1600.	54.
NGC 7469	107.	82.5	26.	1120.	1350.	500.	1350.	41.

Table 11a: The components of the continuous energy distribution of NGC 1068, in units of 10^{-26} erg cm^{-2} sec^{-1} $(c/s)^{-1}$.

μ	$\log(f_o-1)$	log r	$\log(f_o-g)$	log s	log n
2.950	1.38	0.12	1.36	0.77	1.22
2.850	1.41	0.16	1.39	0.85	1.24
2.750	1.45	0.20	1.43	0.98	1.24
2.743	1.46	0.20	1.43		
2.740	1.44	-0.53	1.43		
2.650	1.48	-0.51	1.47	1.00	1.31
2.550	1.54	-0.49	1.54	1.15	1.31
2.450	1.61	-0.46	1.61	1.37	1.24
2.350	1.69	-0.44	1.69	1.39	1.39
2.250	1.76	-0.41	1.76	1.58	1.30
2.150	1.83	-0.38	1.83	1.68	1.31
2.050	1.88	-0.35	1.88	1.72	1.36
1.900	1.95	-0.30	1.95	1.80	1.30
1.800	2.00	-0.26	2.00	1.88	1.41
1.756	2.03	-0.25	2.03		
1.755	2.03	-0.29	2.03		
1.700	2.05	-0.27	2.06		
1.600	2.10	-0.23	2.10	2.02	1.35
1.500	2.16	-0.19	2.16	2.07	1.43
1.400	2.21	-0.15	2.21	2.12	1.46
1.300	2.26	-0.11	2.26	2.20	1.37
1.219	2.30	-0.08	2.30		
1.218	2.30	-0.37	2.30		
1.200	2.31	-0.36	2.31	2.23	1.52
1.100	2.36	-0.32	2.36	2.31	1.40

Table 11b: The components of the continuous energy distribution of NGC 1275, in units of 10^{-26} erg cm^{-2} sec^{-1} $(c/s)^{-1}$.

μ	$\log(f_o-1)$	log r	$\log(f_o-g)$	log s	log n
2.950	1.23	-0.03	1.21	0.08	1.20
2.850	1.23	-0.01	1.20	0.16	1.19
2.750	1.23	+0.02	1.20	0.28	1.18
2.743	1.23	+0.02	1.20		
2.740	1.23	-0.53	1.22		
2.650	1.28	-0.51	1.27	0.31	1.23
2.550	1.33	-0.50	1.32	0.46	1.27
2.450	1.39	-0.47	1.39	0.68	1.30
2.350	1.42	-0.45	1.42	0.70	1.33
2.250	1.45	-0.43	1.45	0.88	1.31
2.150	1.47	-0.41	1.47	0.98	1.30
2.050	1.50	-0.39	1.50	1.03	1.32
1.900	1.55	-0.35	1.55	1.11	1.35
1.800	1.57	-0.33	1.57	1.19	1.34
1.756	1.59	-0.32	1.59		
1.755	1.59	-0.33	1.59		
1.700	1.60	-0.32	1.60	1.27	1.32
1.600	1.63	-0.30	1.63	1.32	1.34
1.500	1.66	-0.26	1.66	1.38	1.34
1.400	1.69	-0.24	1.69	1.43	1.34
1.300	1.72	-0.21	1.72	1.51	1.31
1.219	1.74	-0.19	1.74		
1.218	1.74	-0.38	1.74		
1.200	1.75	-0.38	1.75	1.54	1.34
1.100	1.78	-0.35	1.78	1.62	1.28

Table 11c: The components of the continuous energy distribution of NGC 3227, in units of 10^{-26} erg cm^{-2} sec^{-1} $(c/s)^{-1}$.

μ	$\log(f_o-1)$	log r	$\log(f_o-g)$	log s	log n
2.950	0.66	-0.48	0.63	-0.20	0.56
2.850	0.68	-0.46	0.65	-0.12	0.56
2.750	0.69	-0.43	0.65	0.01	0.54
2.743	0.69	-0.43	0.66		
2.740	0.66	-0.96	0.65		
2.650	0.72	-0.95	0.71	0.04	0.67
2.550	0.80	-0.94	0.79	0.19	0.67
2.450	0.90	-0.92	0.89	0.40	0.72
2.350	0.93	-0.91	0.92	0.43	0.76
2.250	1.00	-0.89	0.99	0.61	0.76
2.150	1.06	-0.88	1.05	0.71	0.79
2.050	1.13	-0.86	1.13	0.76	0.87
1.900	1.22	-0.83	1.22	0.84	0.98
1.800	1.29	-0.81	1.29	0.92	1.05
1.756	1.32	-0.80	1.32		
1.755	1.32	-0.81	1.32		
1.700	1.34	-0.80	1.34	1.00	1.08
1.600	1.39	-0.77	1.39	1.05	1.12
1.500	1.42	-0.75	1.42	1.11	1.13
1.400	1.45	-0.72	1.45	1.16	1.13
1.300	1.47	-0.70	1.47	1.24	1.09
1.219	1.49	-0.68	1.49		
1.218	1.49	-0.89	1.49		
1.200	1.49	-0.89	1.49	1.27	1.09
1.100	1.52	-0.86	1.52	1.35	1.04

Table 11d: The components of the continuous energy distribution of NGC 3516, in units of 10^{-26} erg cm^{-2} sec^{-1} $(c/s)^{-1}$.

μ	$\log(f_o-1)$	log r	$\log(f_o-g)$	log s	log n
2.950	0.97	-1.11	0.97	0.28	0.86
2.850	0.98	-1.09	0.98	0.36	0.84
2.750	0.98	-1.07	0.98	0.49	0.80
2.743	0.99	-1.07	0.98		
2.740	0.97	-1.54	0.97		
2.650	0.98	-1.53	0.98	0.51	0.80
2.550	1.08	-1.52	1.08	0.66	0.87
2.450	1.17	-1.51	1.17	0.88	0.86
2.350	1.23	-1.49	1.23	0.90	0.95
2.250	1.29	-1.48	1.29	1.09	0.86
2.150	1.36	-1.46	1.36	1.19	0.88
2.050	1.42	-1.44	1.42	1.24	0.96
1.900	1.50	-1.42	1.50	1.32	0.96
1.800	1.54	-1.40	1.54	1.40	0.99
1.756	1.57	-1.39	1.57		
1.755	1.57	-1.41	1.57		
1.700	1.60	-1.40	1.60	1.48	0.95
1.600	1.65	-1.37	1.65	1.53	1.03
1.500	1.70	-1.35	1.70	1.58	1.08
1.400	1.74	-1.33	1.74	1.64	1.06
1.300	1.79	-1.31	1.79	1.71	1.01
1.219	1.82	-1.29	1.82		
1.218	1.82	-1.47	1.82		
1.200	1.82	-1.47	1.82	1.75	1.06
1.100	1.86	-1.44	1.86	1.82	0.78

Table 11e: The components of the continuous energy distribution of NGC 4051, in units of 10^{-26} erg cm^{-2} sec^{-1} $(c/s)^{-1}$.

μ	$\log(f_o-1)$	log r	$\log(f_o-g)$	log s	log n
2.950	0.81	-0.03	0.74	-0.56	0.72
2.850	0.83	-0.01	0.76	-0.48	0.74
2.750	0.87	+0.02	0.80	-0.35	0.77
2.743	0.87	+0.02	0.80		
2.740	0.83	-0.49	0.81		
2.650	0.85	-0.48	0.83	-0.33	0.80
2.550	0.88	-0.46	0.86	-0.18	0.82
2.450	0.92	-0.44	0.90	0.04	0.84
2.350	0.97	-0.43	0.95	0.06	0.89
2.250	1.01	-0.41	0.99	0.25	0.91
2.150	1.05	-0.39	1.03	0.35	0.93
2.050	1.10	-0.37	1.08	0.40	0.99
1.900	1.16	-0.34	1.15	0.48	1.04
1.800	1.22	-0.31	1.21	0.56	1.10
1.756	1.23	-0.31	1.22		
1.755	1.23	-0.32	1.22		
1.700	1.24	-0.31	1.23	0.64	1.10
1.600	1.25	-0.29	1.24	0.69	1.10
1.500	1.26	-0.26	1.25	0.74	1.09
1.400	1.28	-0.24	1.27	0.80	1.08
1.300	1.29	-0.22	1.28	0.87	1.05
1.219	1.29	-0.20	1.28		
1.218	1.29	-0.38	1.28		
1.200	1.29	-0.38	1.28	0.90	1.04
1.100	1.30	-0.35	1.29	0.98	1.00

Table 11f: The components of the continuous energy distribution of NGC 4151, in units of 10^{-26} erg cm^{-2} sec^{-1} $(c/s)^{-1}$.

μ	$\log(f_o-1)$	log r	$\log(f_o-g)$	log s	log n
2.950	1.76	1.44	1.48	0.52	1.43
2.850	1.77	1.46	1.48	0.60	1.42
2.750	1.78	1.48	1.48	0.73	1.40
2.743	1.78	1.48	1.48		
2.740	1.60	1.01	1.47		
2.650	1.64	1.02	1.52	0.75	1.44
2.550	1.67	1.03	1.56	0.90	1.45
2.450	1.70	1.05	1.59	1.12	1.41
2.350	1.73	1.06	1.62	1.14	1.45
2.250	1.79	1.07	1.70	1.33	1.46
2.150	1.85	1.09	1.77	1.43	1.50
2.050	1.89	1.11	1.82	1.48	1.54
1.900	1.96	1.13	1.89	1.56	1.62
1.800	1.99	1.15	1.92	1.64	1.61
1.756	2.00	1.16	1.93		
1.755	2.00	1.14	1.93		
1.700	2.02	1.15	1.95	1.72	1.58
1.600	2.05	1.18	1.99	1.77	1.60
1.500	2.08	1.20	2.02	1.82	1.59
1.400	2.12	1.22	2.06	1.88	1.60
1.300	2.15	1.24	2.09	1.95	1.53
1.219	2.18	1.26	2.12		
1.218	2.18	1.08	2.14		
1.200	2.18	1.08	2.14	1.98	1.65
1.100	2.22	1.10	2.18	2.06	1.57

Table 11g: The components of the continuous energy distribution of NGC 5548, in units of 10^{-26} erg cm^{-2} sec^{-1} $(c/s)^{-1}$.

μ	$\log(f_o-1)$	log r	$\log(f_o-g)$	log s	log n
2.950	1.10	0.77	0.82	-0.58	0.80
2.850	1.11	0.80	0.82	-0.50	0.80
2.750	1.11	0.82	0.80	-0.37	0.79
2.743	1.11	0.82	0.80		
2.740	0.93	0.34	0.80		
2.650	0.95	0.35	0.82	-0.35	0.79
2.550	0.79	0.37	0.84	-0.20	0.80
2.450	0.98	0.38	0.85	0.02	0.79
2.350	1.00	0.39	0.88	0.04	0.81
2.250	1.02	0.41	0.90	0.23	0.80
2.150	1.04	0.43	0.92	0.33	0.79
2.050	1.06	0.44	0.94	0.38	0.80
1.900	1.10	0.47	0.98	0.49	0.81
1.800	1.14	0.49	1.03	0.54	0.86
1.756	1.16	0.50	1.05		
1.755	1.16	0.48	1.06		
1.700	1.18	0.49	1.08	0.62	0.90
1.600	1.23	0.51	1.14	0.67	0.96
1.500	1.27	0.54	1.18	0.72	1.00
1.400	1.32	0.56	1.24	0.78	1.06
1.300	1.37	0.58	1.29	0.85	1.10
1.219	1.41	0.60	1.33		
1.218	1.41	0.42	1.36		
1.200	1.42	0.42	1.37	0.89	1.20
1.100	1.47	0.44	1.43	0.96	1.25

Table 11h: The components of the continuous energy distribution of NGC 7469, in units of 10^{-26} erg cm^{-2} sec^{-1} $(c/s)^{-1}$.

μ	$\log(f_o-1)$	log r	$\log(f_o-g)$	log s	log n
2.950	1.19	0.70	1.02	-0.20	0.99
2.850	1.19	0.72	1.01	-0.12	0.98
2.750	1.19	0.74	1.00	0.00	0.97
2.743	1.19	0.74	1.00		
2.740	1.07	0.27	0.99		
2.650	1.10	0.28	1.03	0.03	0.98
2.550	1.12	0.29	1.05	0.18	0.99
2.450	1.14	0.30	1.07	0.40	0.97
2.350	1.16	0.32	1.09	0.42	0.99
2.250	1.19	0.33	1.12	0.60	0.97
2.150	1.21	0.35	1.14	0.70	0.96
2.050	1.24	0.37	1.18	0.75	0.97
1.900	1.28	0.40	1.22	0.87	0.96
1.800	1.32	0.42	1.26	0.91	1.00
1.756	1.35	0.42	1.29		
1.755	1.35	0.41	1.30		
1.700	1.37	0.42	1.32	0.99	1.04
1.600	1.42	0.44	1.37	1.04	1.09
1.500	1.46	0.46	1.41	1.10	1.13
1.400	1.51	0.48	1.47	1.15	1.18
1.300	1.56	0.50	1.52	1.23	1.21
1.219	1.60	0.52	1.56		
1 218	1.60	0.34	1.57		
1.200	1 61	0.34	1.58	1.26	1.30
1.100	1 66	0.37	1.64	1.34	1.33

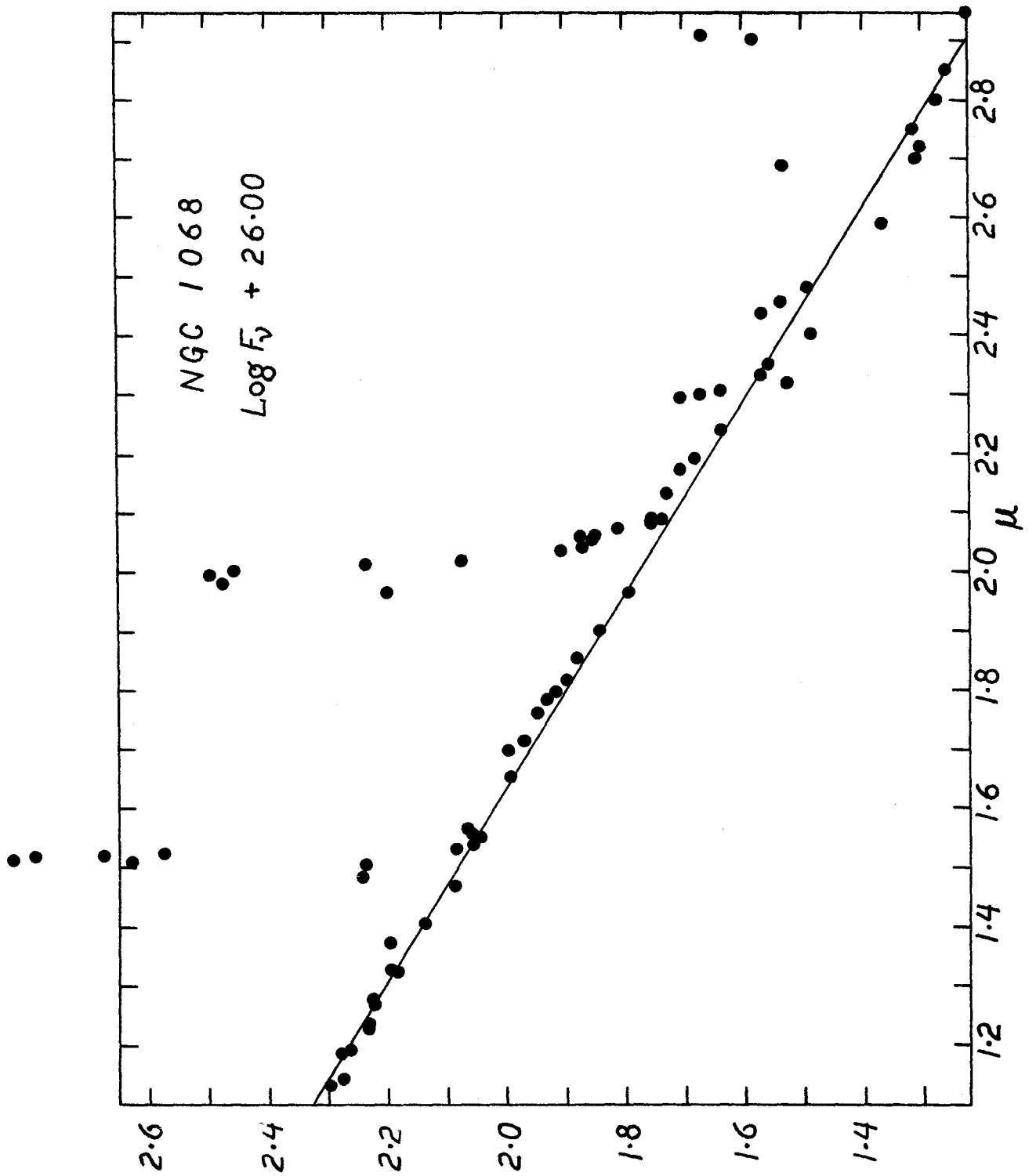

Figure 1a: The continuous energy distribution of NGC 1068 uncorrected for reddening. (50Å bandpass)

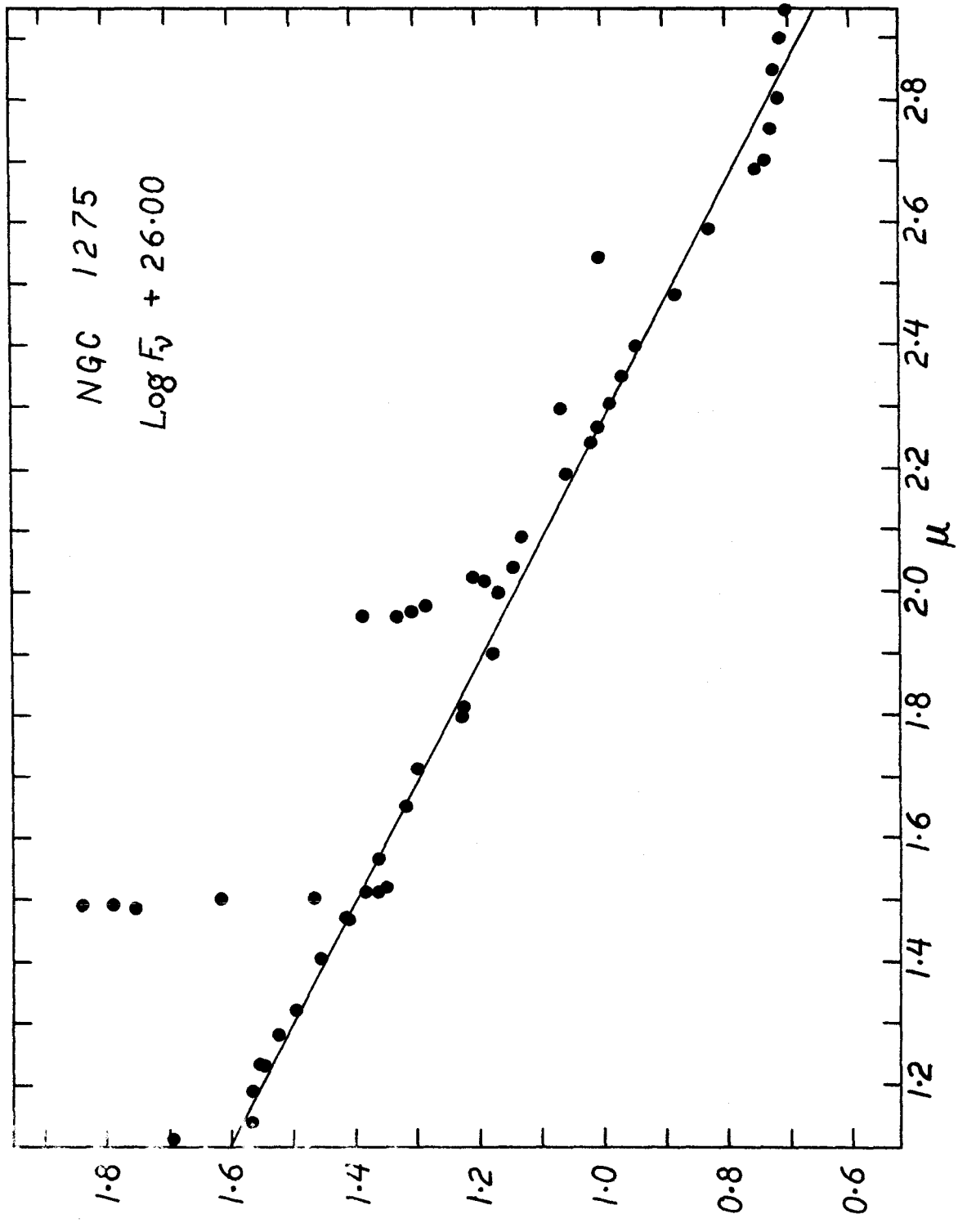

Figure 1b: The continuous energy distribution of NGC 1275 uncorrected for reddening. (50Å bandpass)

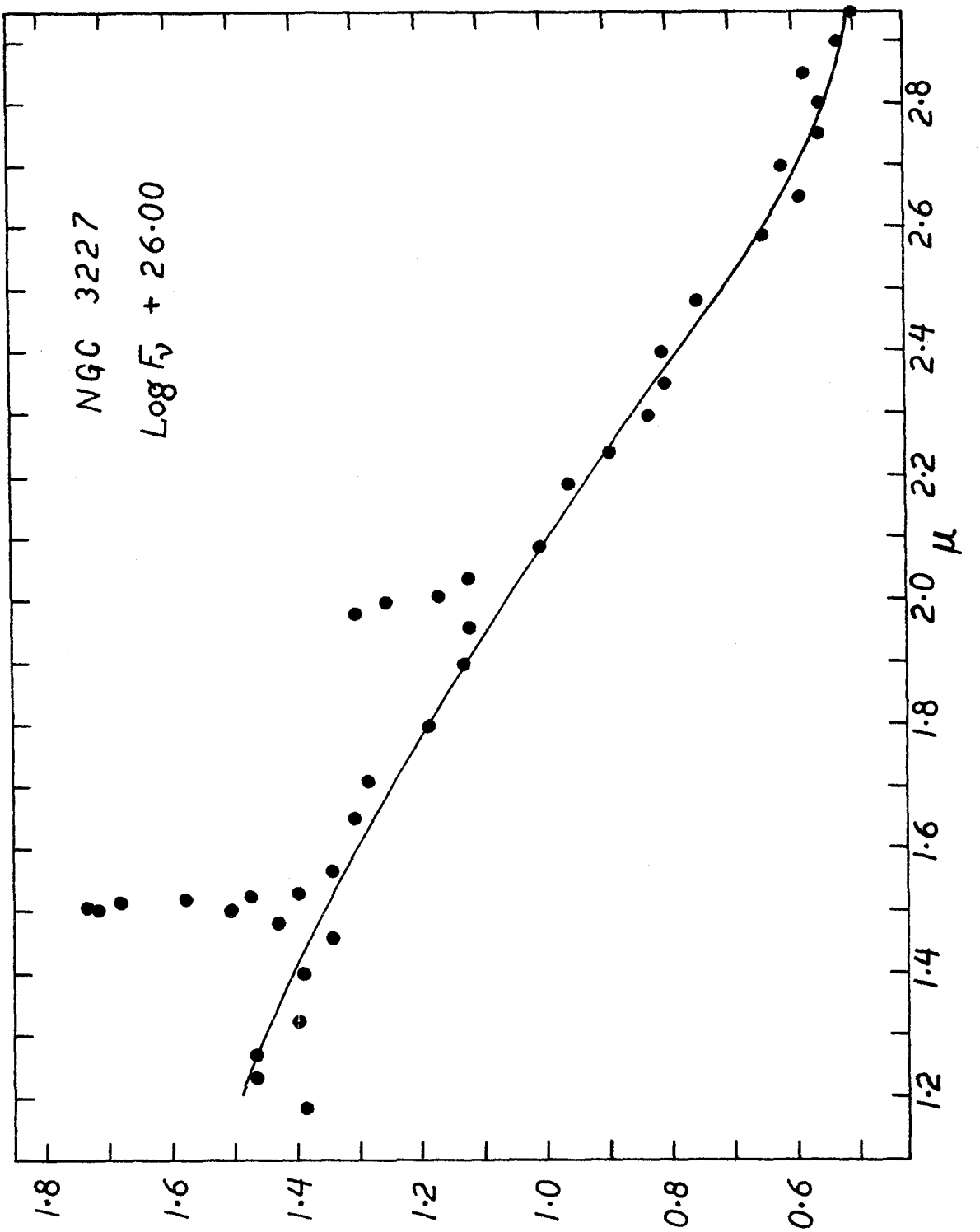

Figure 1c: The continuous energy distribution of NGC 3227 uncorrected for reddening. (50Å bandpass)

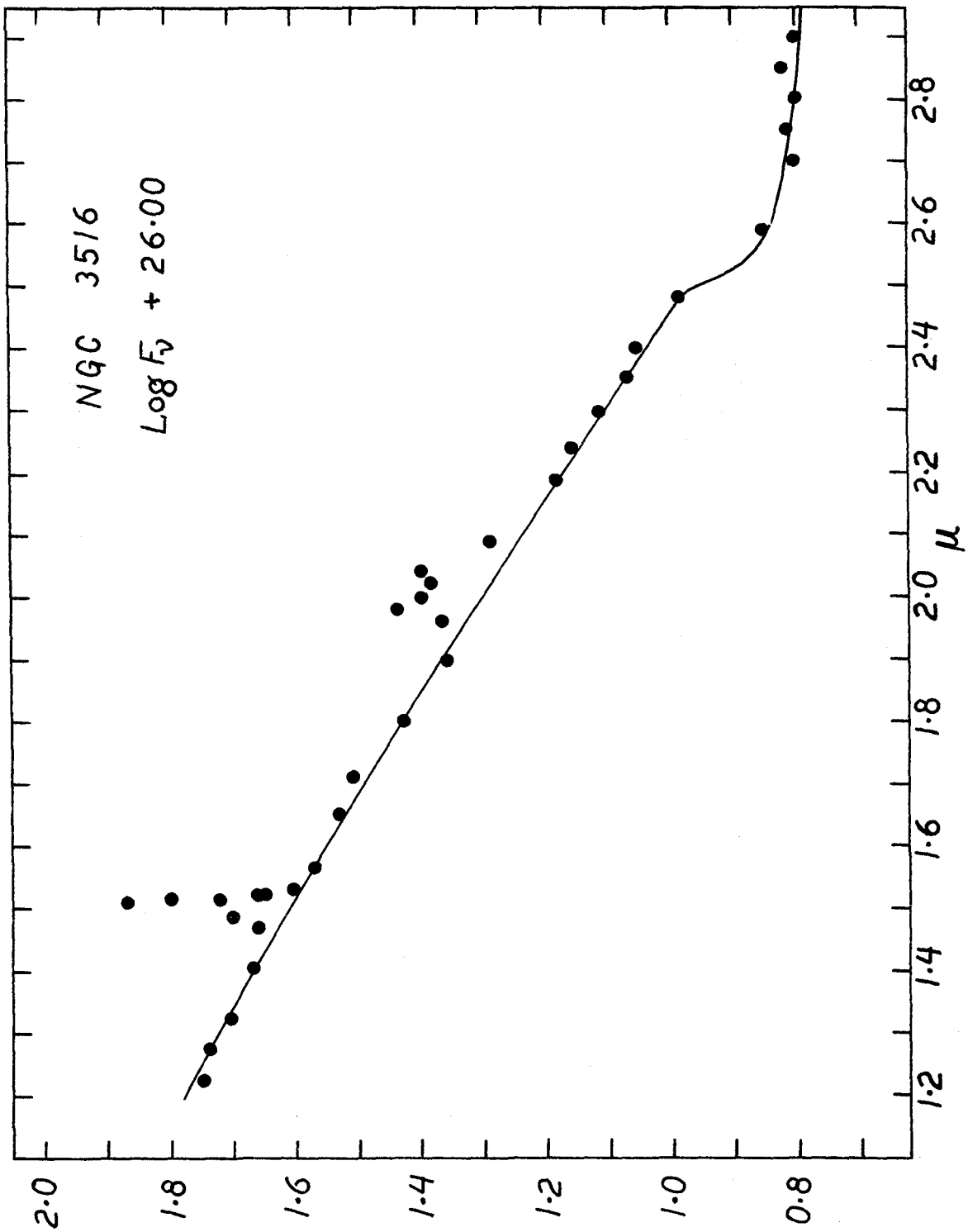

Figure 1d: The continuous energy distribution of NGC 3516 uncorrected for reddening. (50Å bandpass)

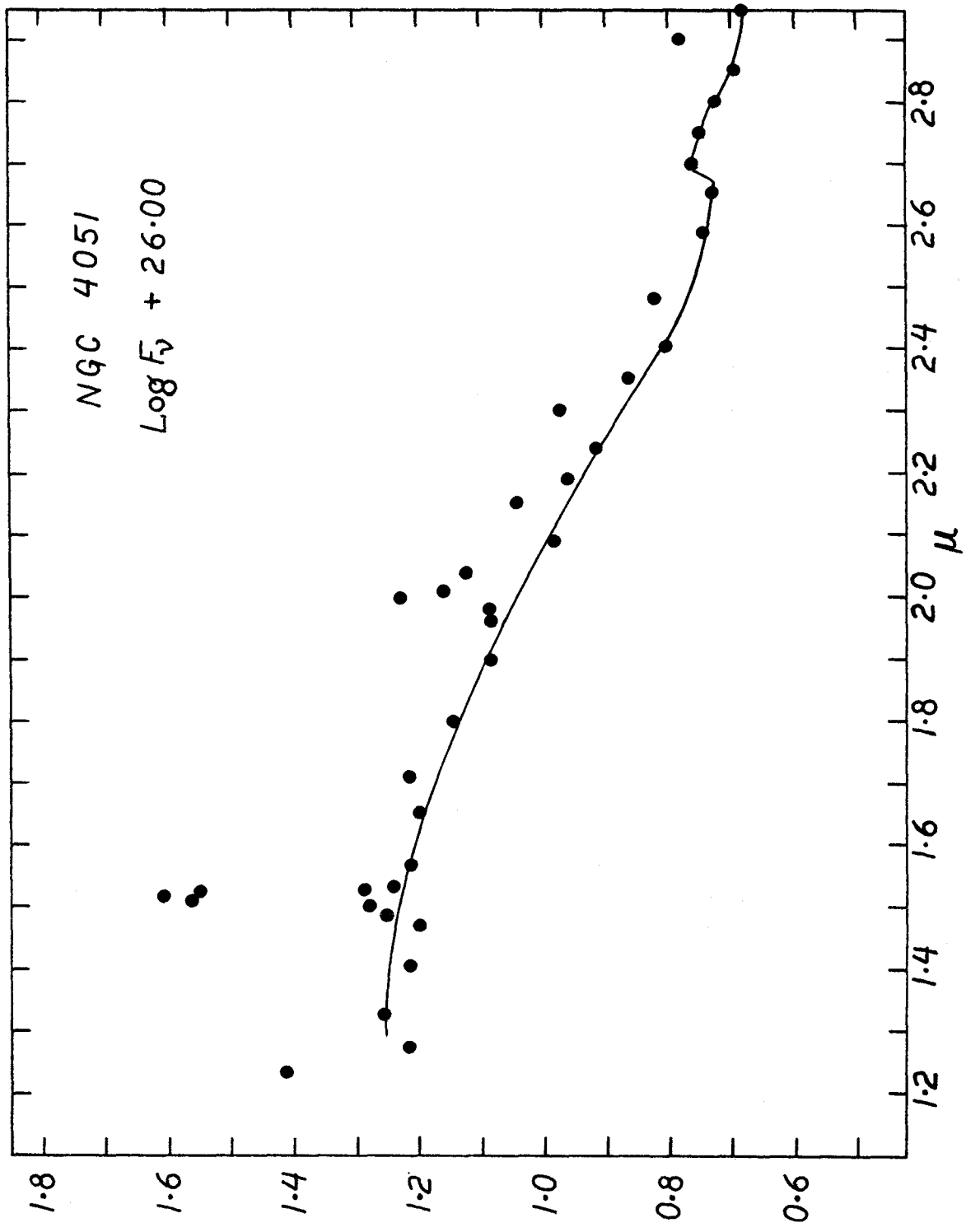

Figure 1e: The continuous energy distribution of NGC 4051 uncorrected for reddening. (50Å bandpass)

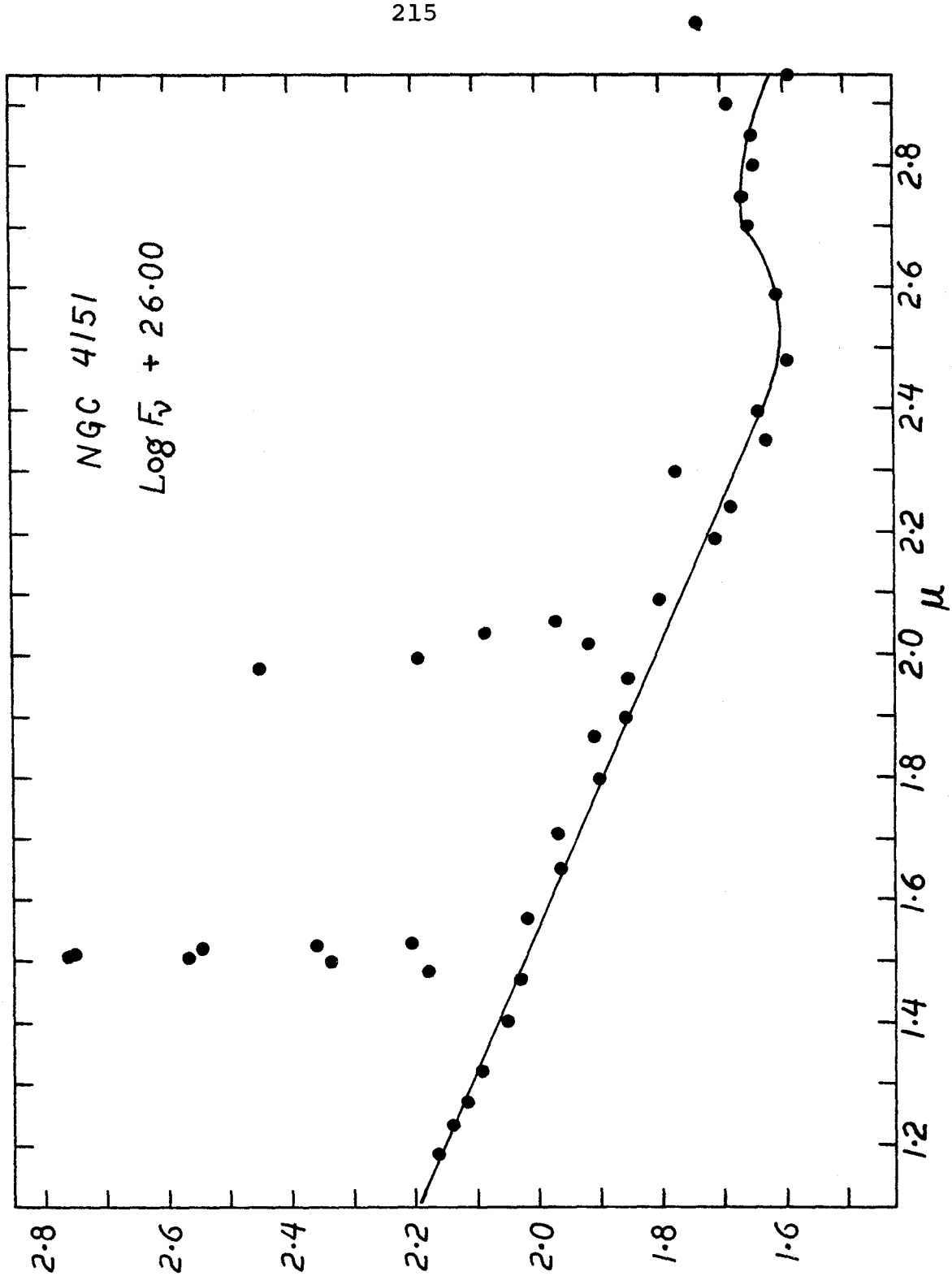

Figure 1f: The continuous energy distribution of NGC 4151 uncorrected for reddening. (50Å bandpass)

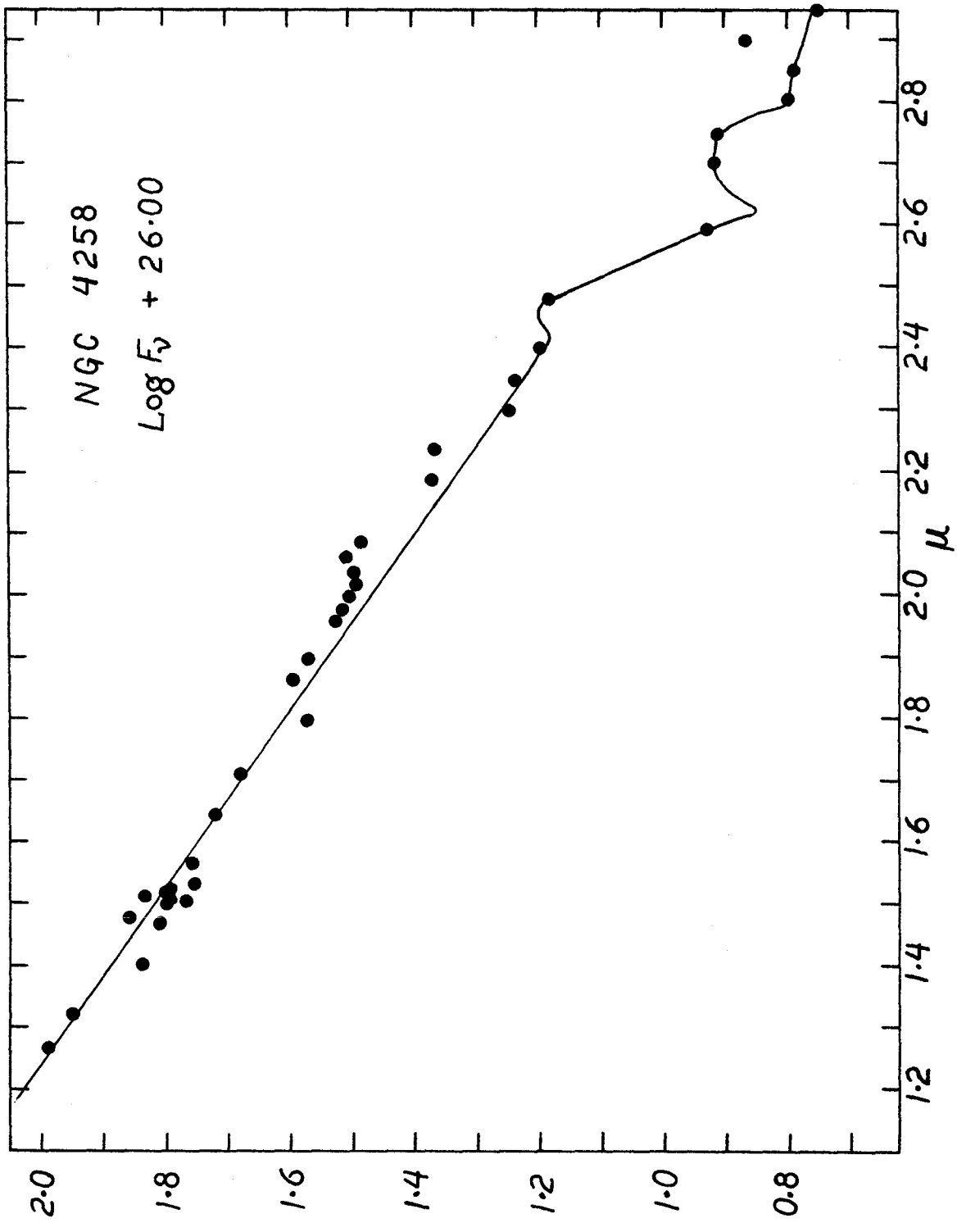

Figure 1g: The continuous energy distribution of NGC 4258 uncorrected for reddening. (50Å bandpass)

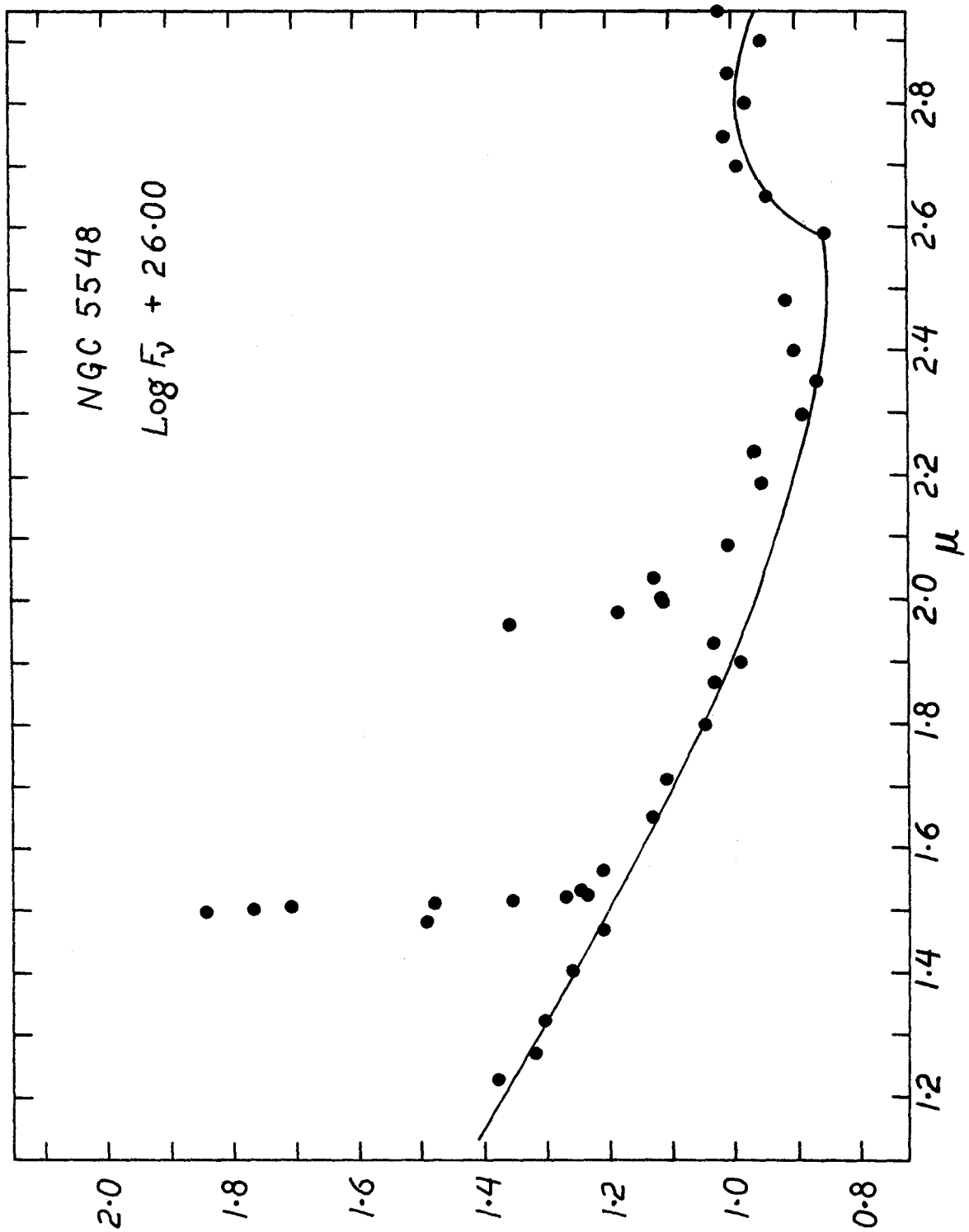

Figure 1h: The continuous energy distribution of NGC 5548 uncorrected for reddening. (50Å bandpass)

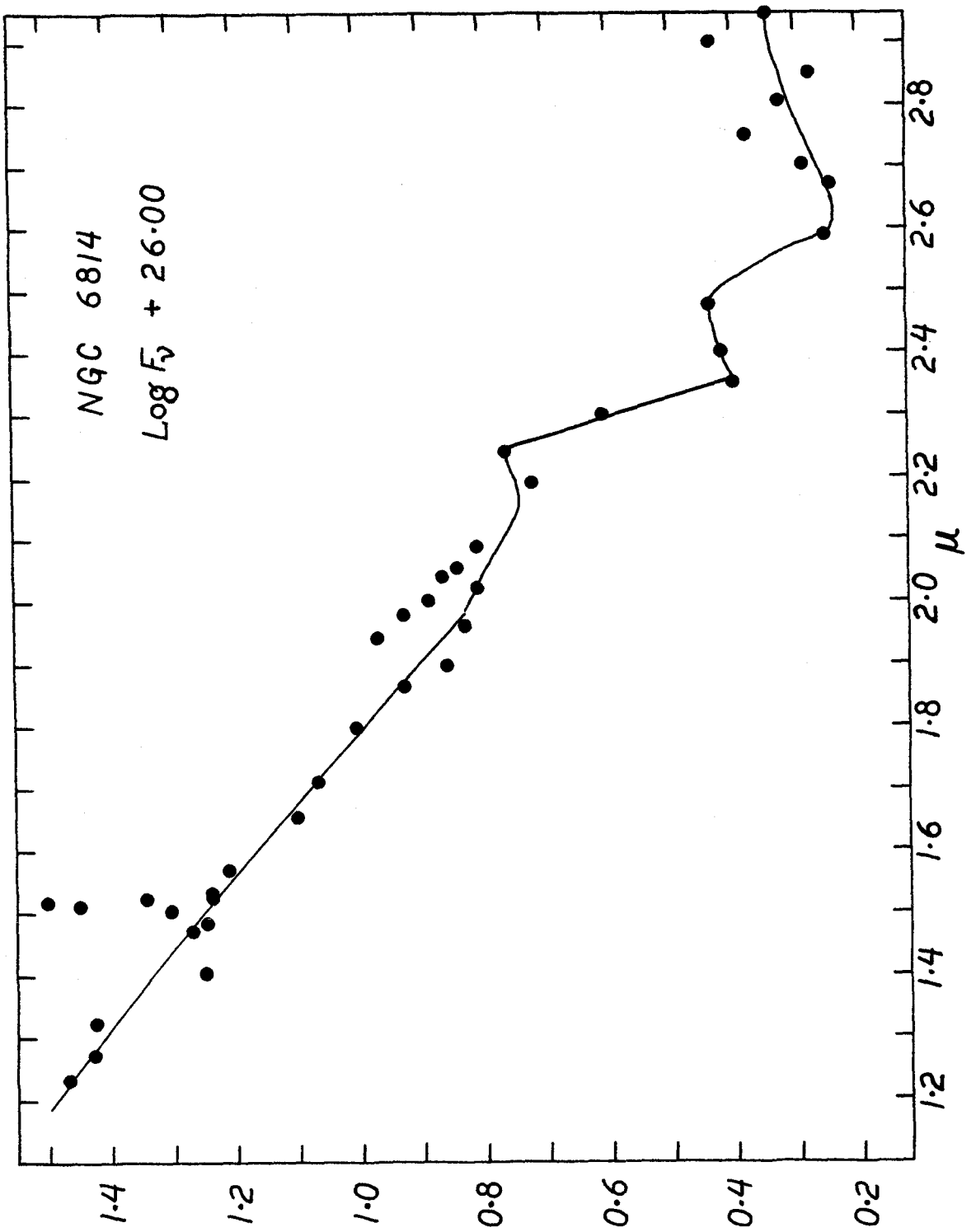

Figure 1i: The continuous energy distribution of NGC 6814 uncorrected for reddening. (50Å bandpass)

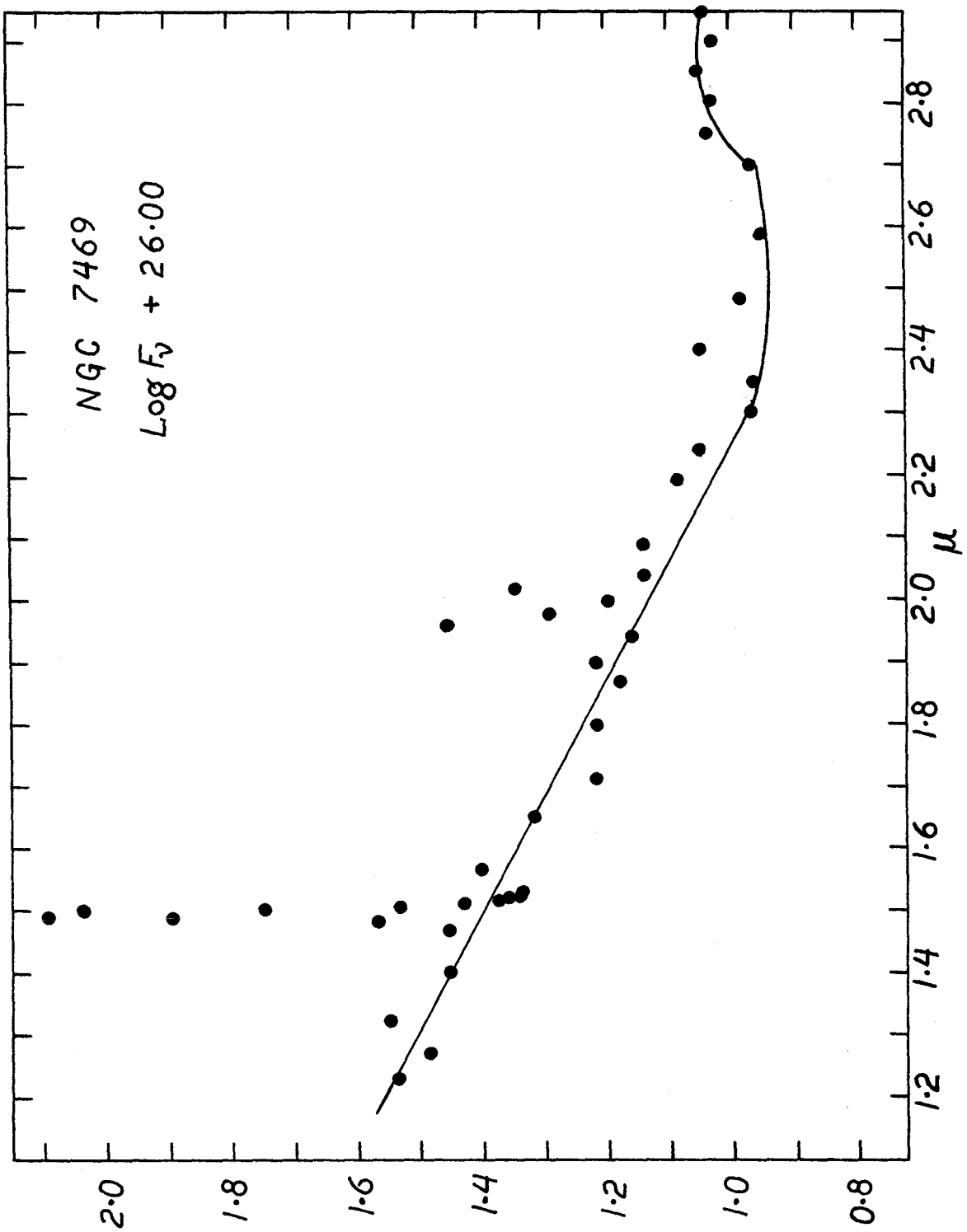

Figure 1j: The continuous energy distribution of NGC 7469 uncorrected for reddening. (50Å bandpass)

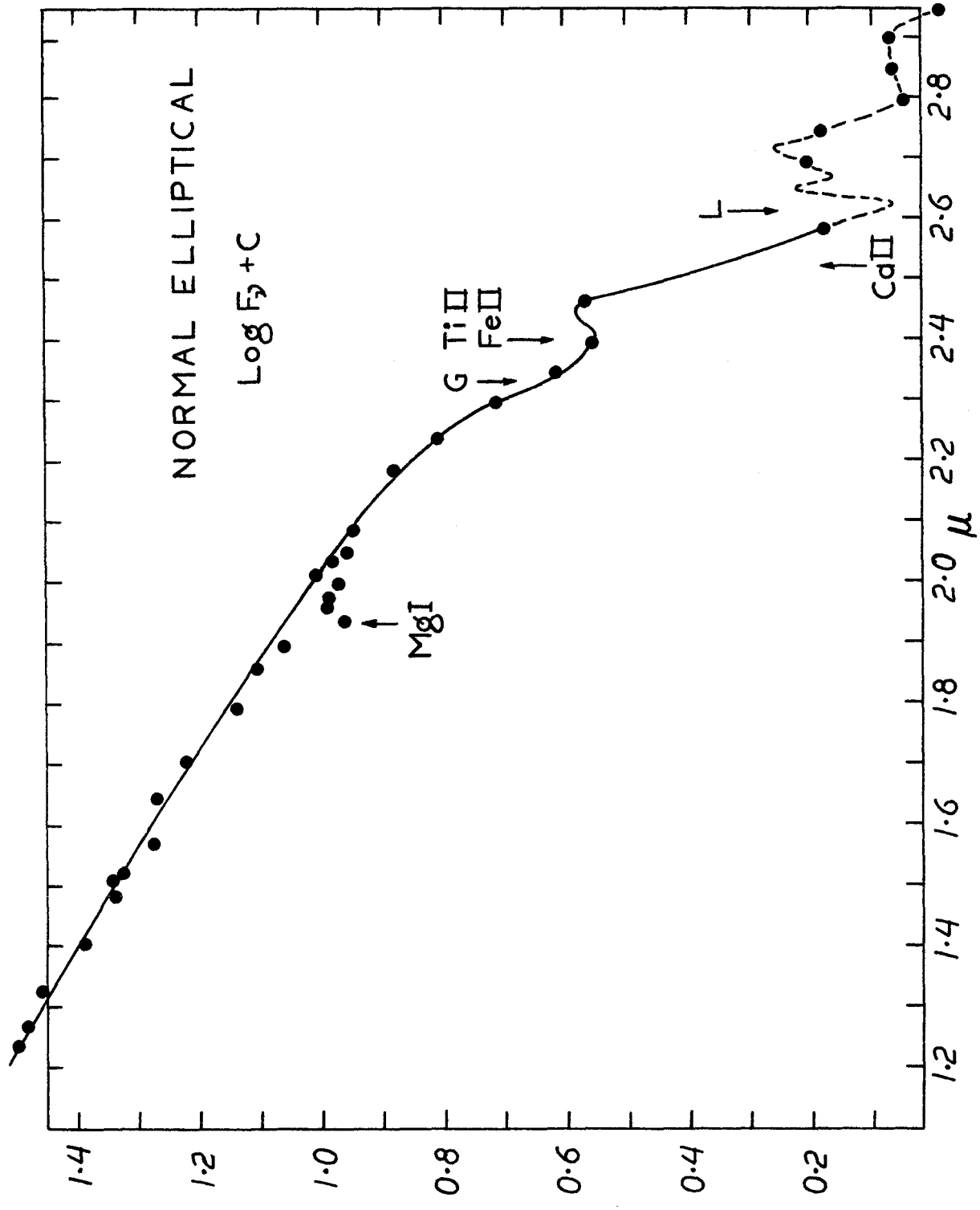

Figure 2: The continuous energy distribution of the nucleus of a normal spiral, based upon NGC 224. The zero point of the log F_λ scale is arbitrary. Fluxes correspond to csc b = 1. (50Å bandpass)

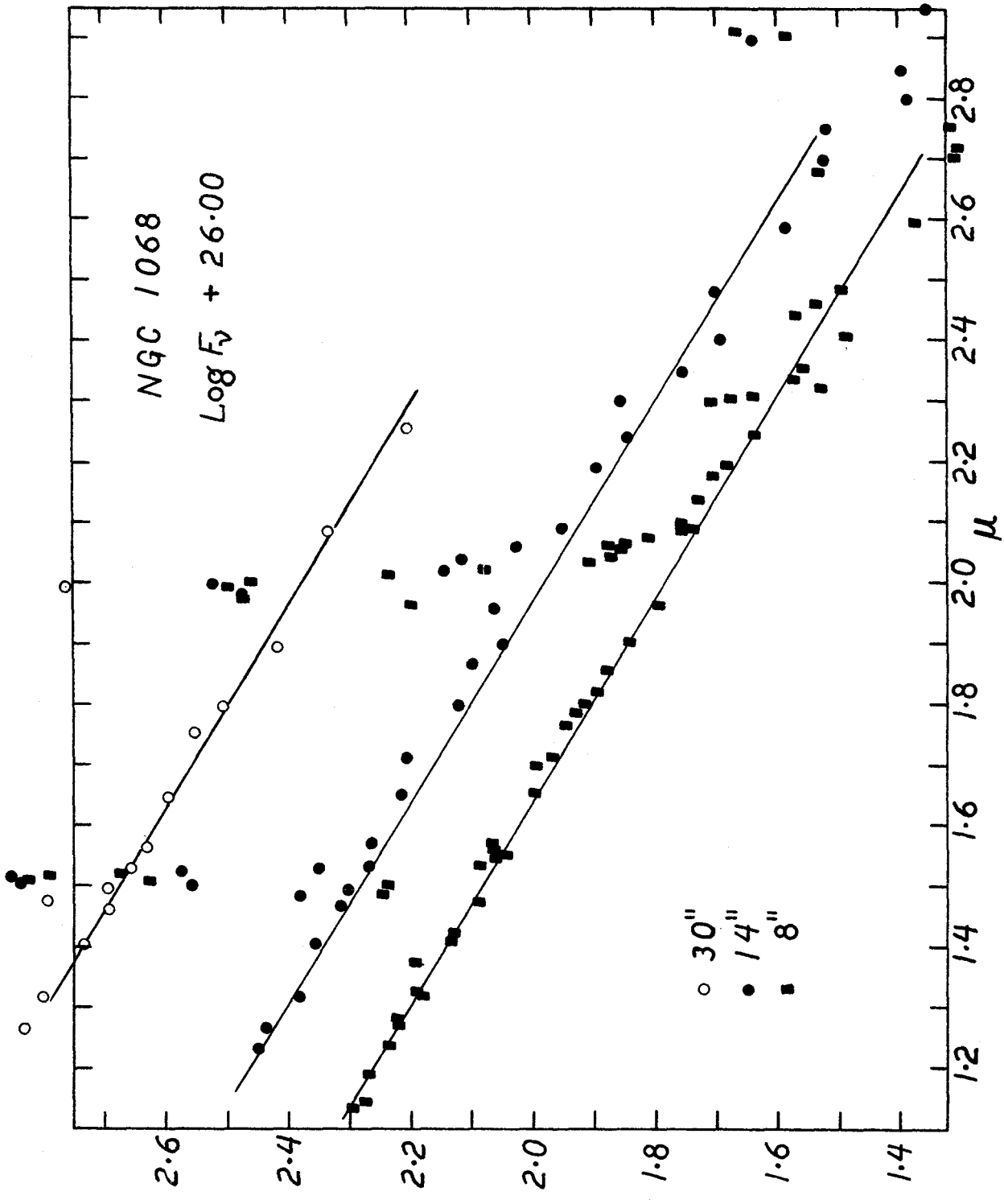

Figure 3: The observed absolute flux distribution of NGC 1068 as a function of aperture diameter. (50Å bandpass)

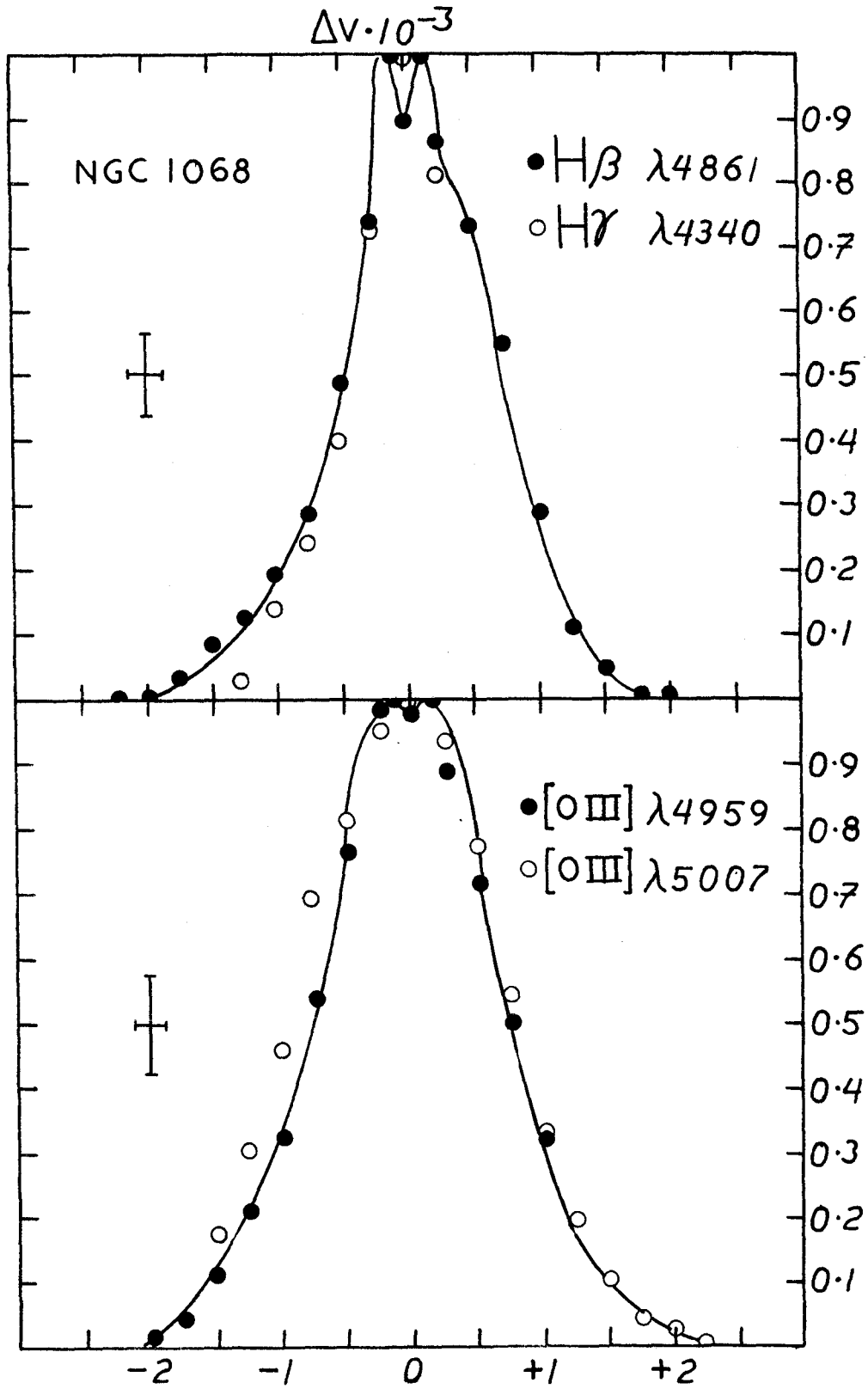

Figure 4a: Relative Doppler profiles of the emission lines of NGC 1068. The horizontal scale is in units of 1000 km/sec.

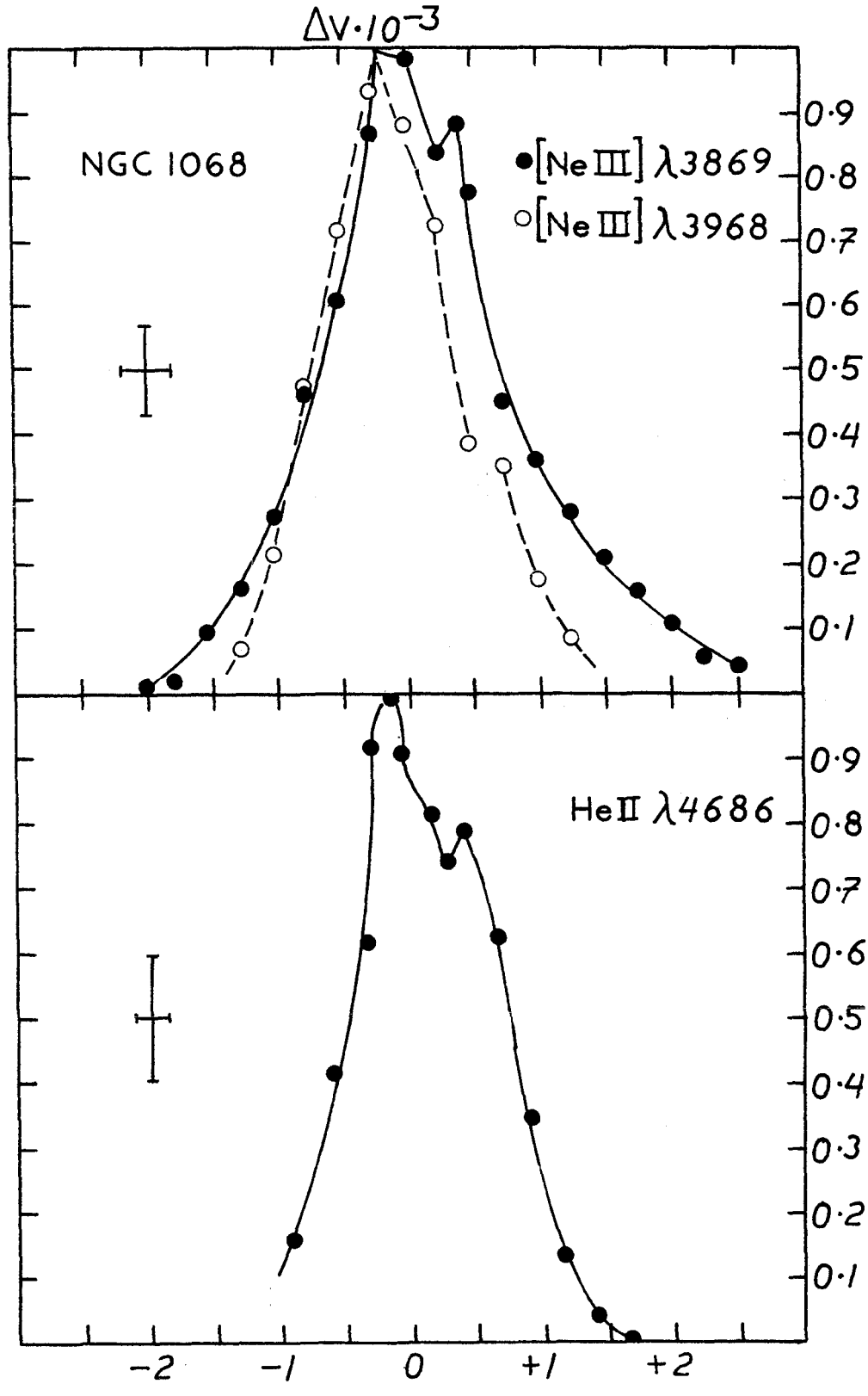

Figure 4a (continued): Relative Doppler profiles of the emission lines of NGC 1068. The horizontal scale is in units of 1000 km/sec.

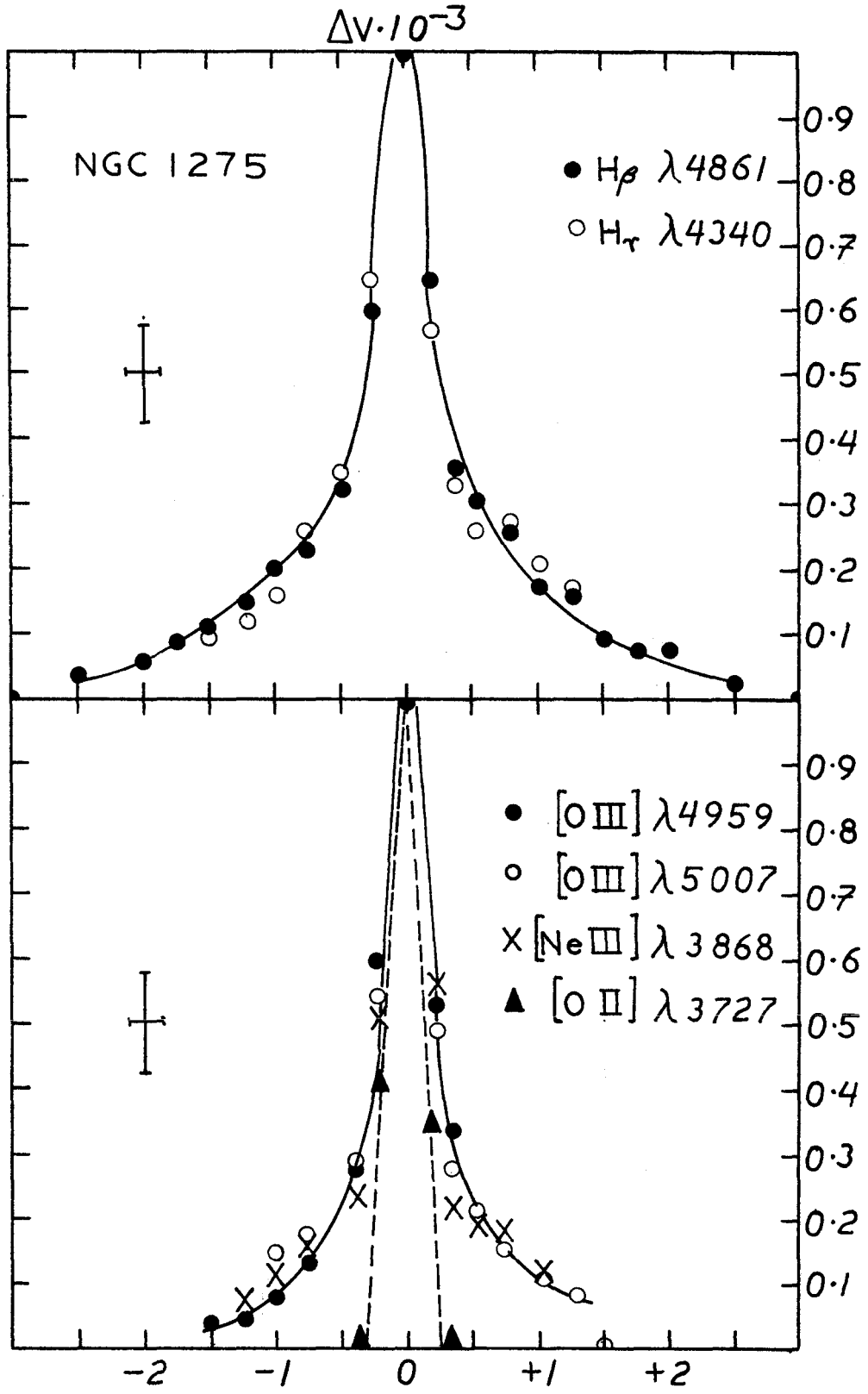

Figure 4b: Relative Doppler profiles of the emission lines of NGC 1275. The horizontal scale is in units of 1000 km/sec.

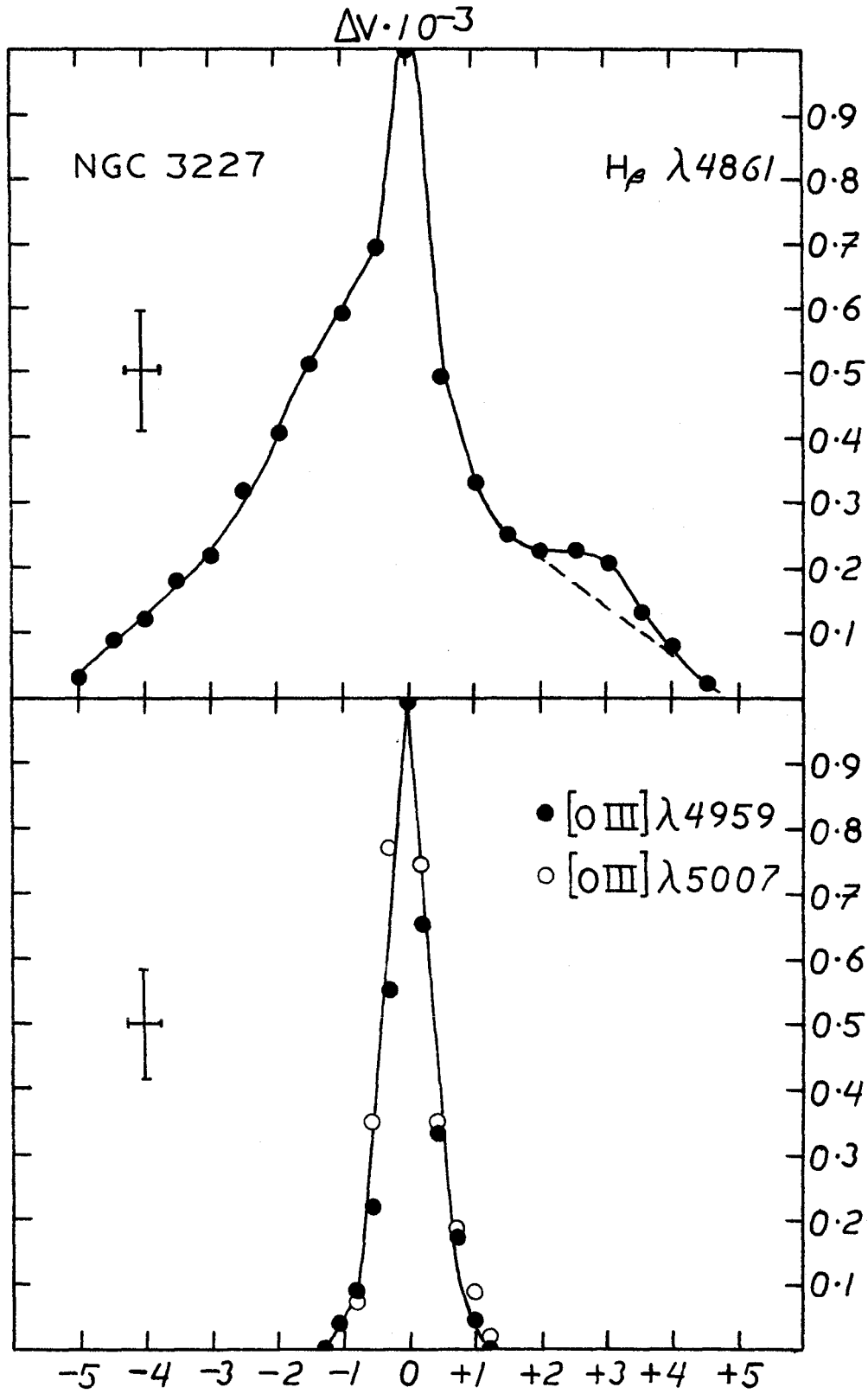

Figure 4c: Relative Doppler profiles of the emission lines in NGC 3227. The horizontal scale is in units of 1000 km/sec.

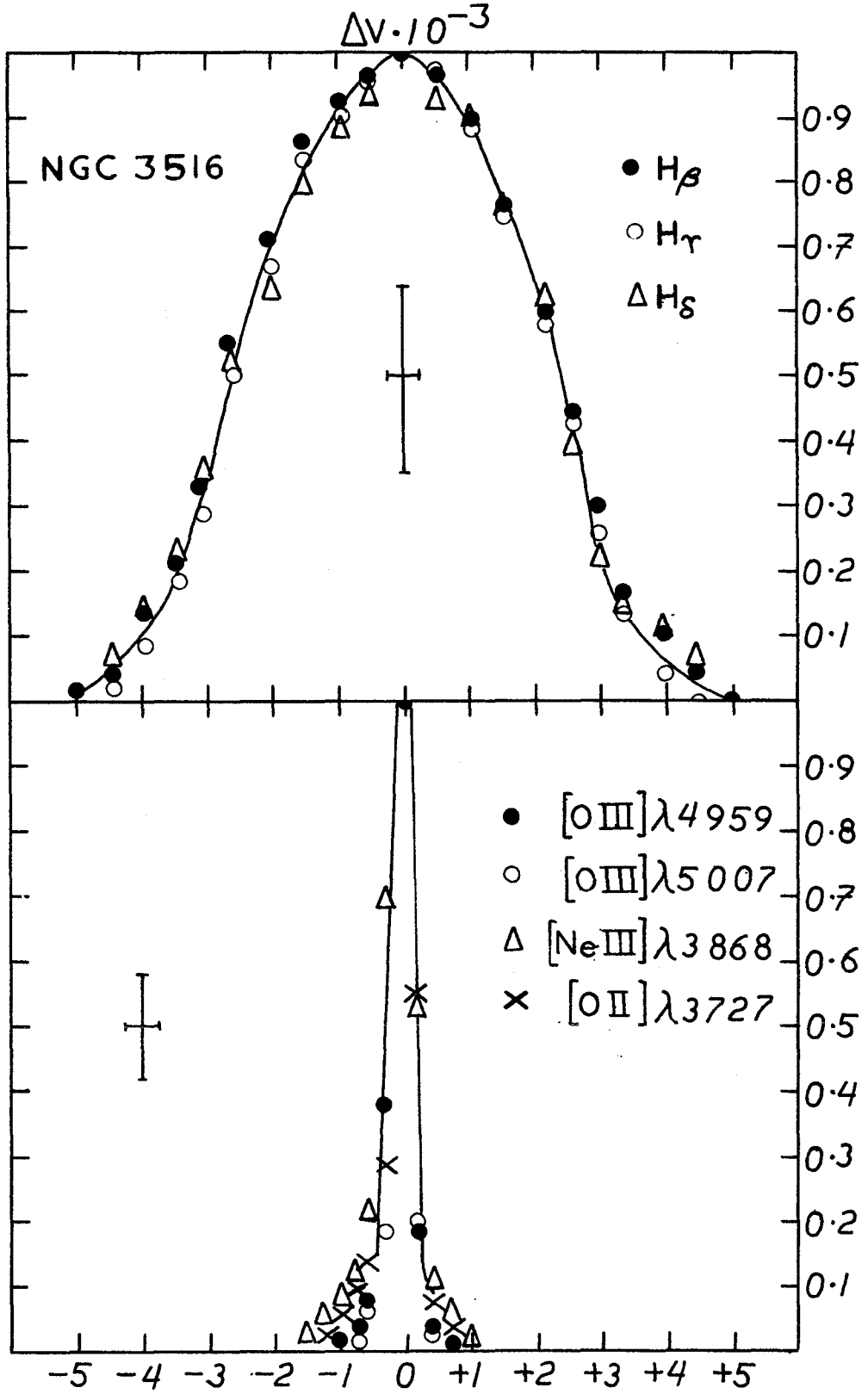

Figure 4d: Relative Doppler profiles of the emission lines in NGC 3516. The horizontal scale is in units of 1000 km/sec.

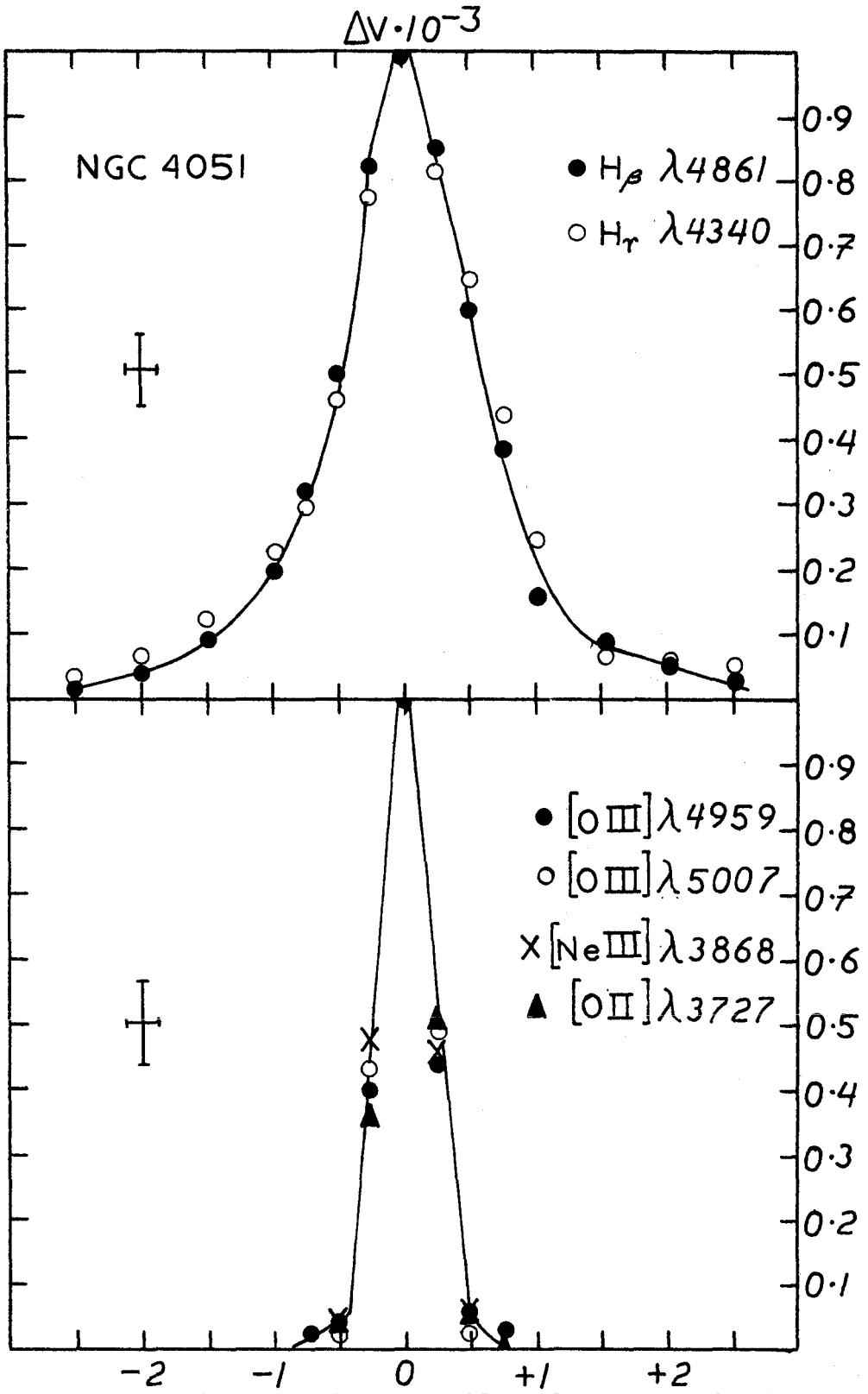

Figure 4e: Relative Doppler profiles for the emission lines in NGC 4051. The horizontal scale is in units of 1000 km/sec.

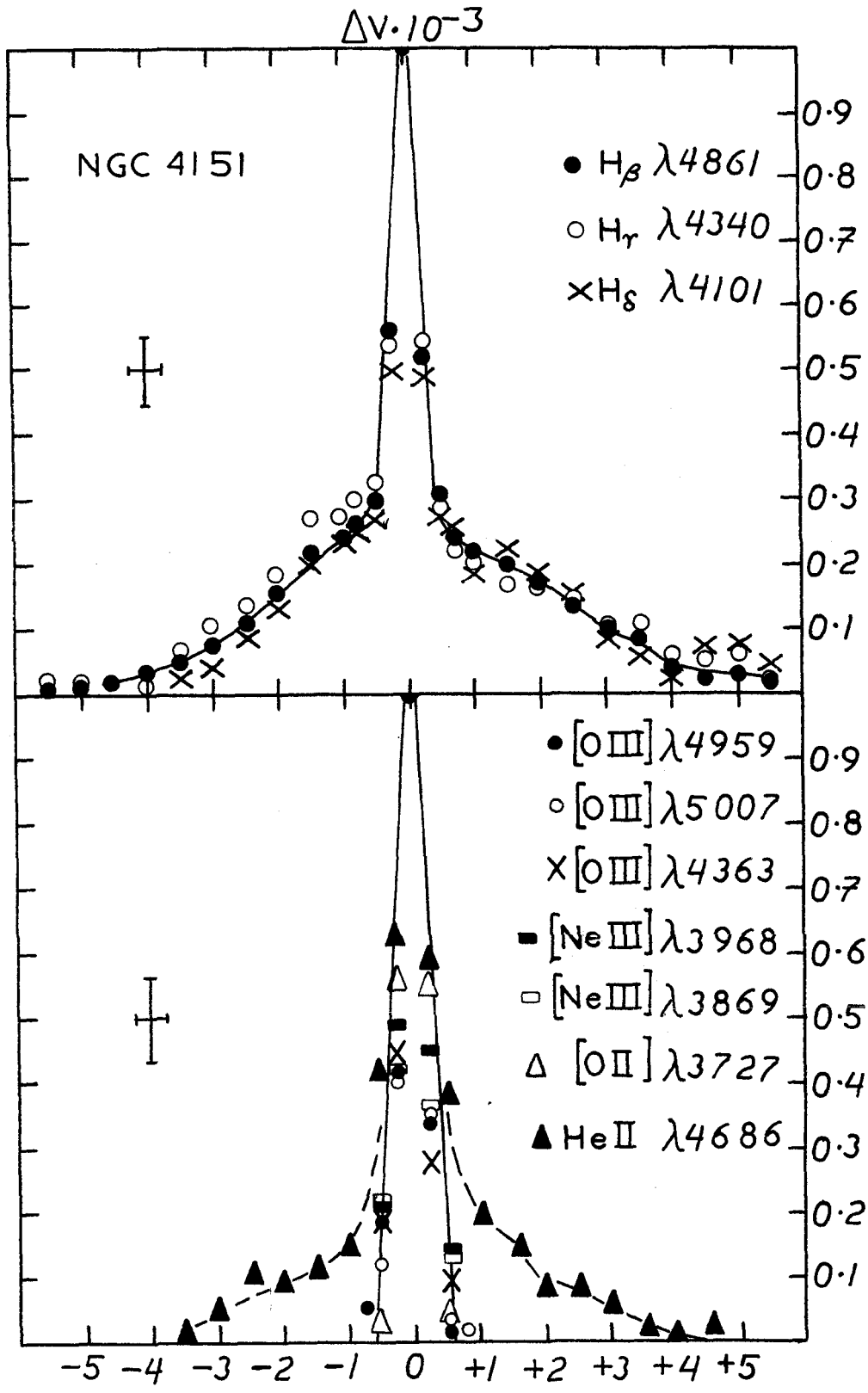

Figure 4f: Relative Doppler profiles for the emission lines in NGC 4151. The horizontal scale is in units of 1000 km/sec.

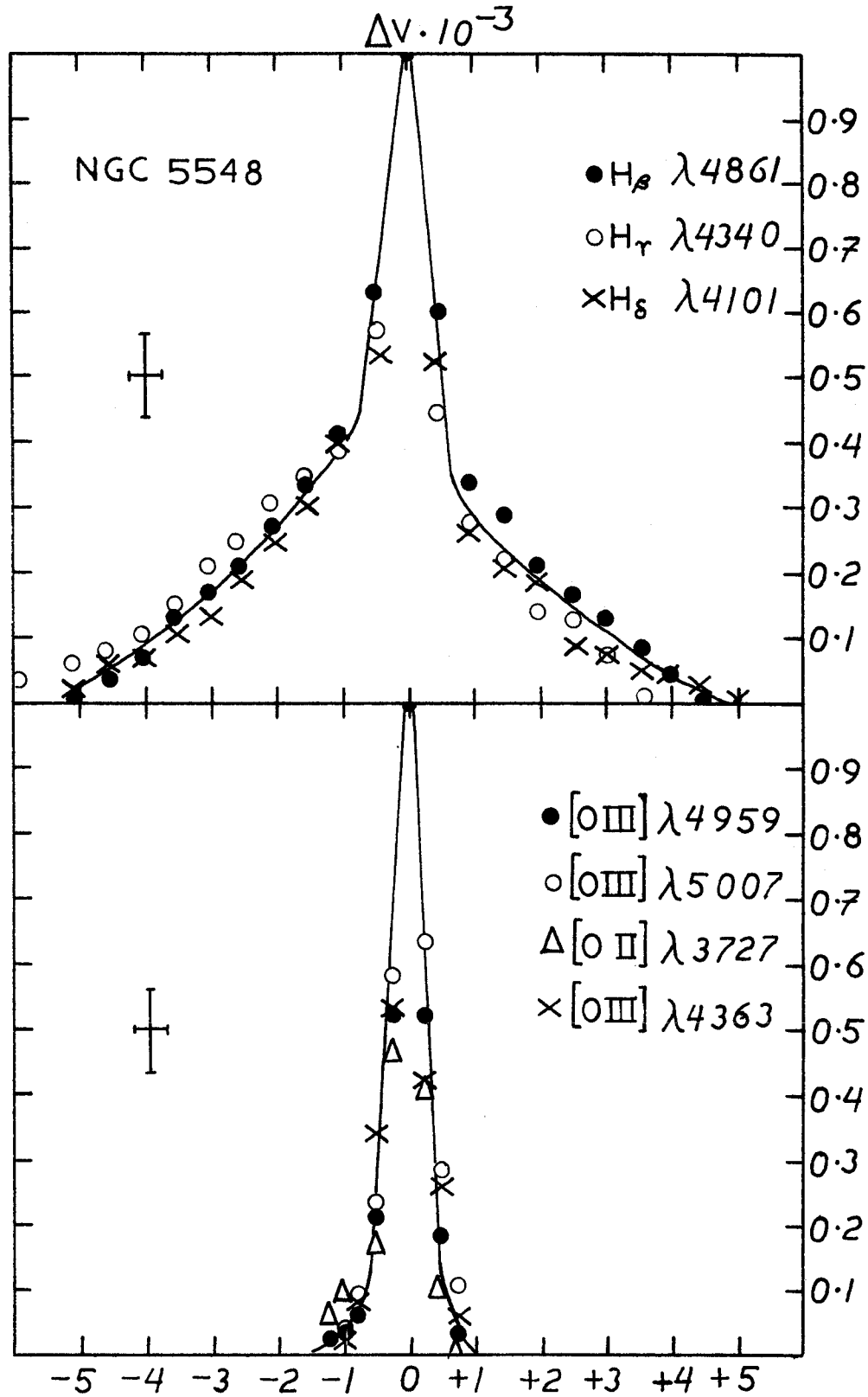

Figure 4g: Relative Doppler profiles for the emission lines in NGC 5548. The horizontal scale is in units of 1000 km/sec.

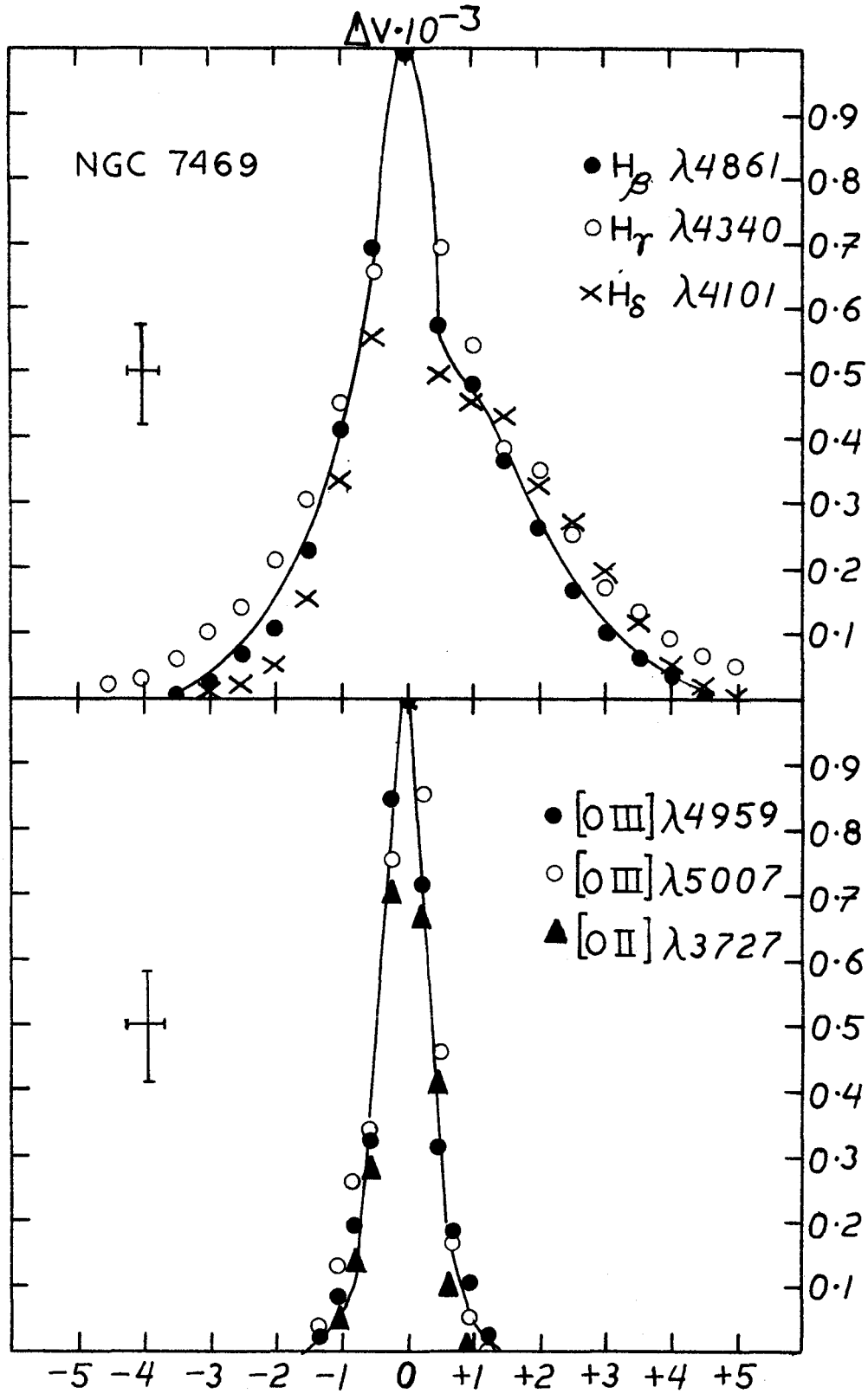

Figure 4h: Relative Doppler profiles for the emission lines in NGC 7469. The horizontal scale is in units of 1000 km/sec.

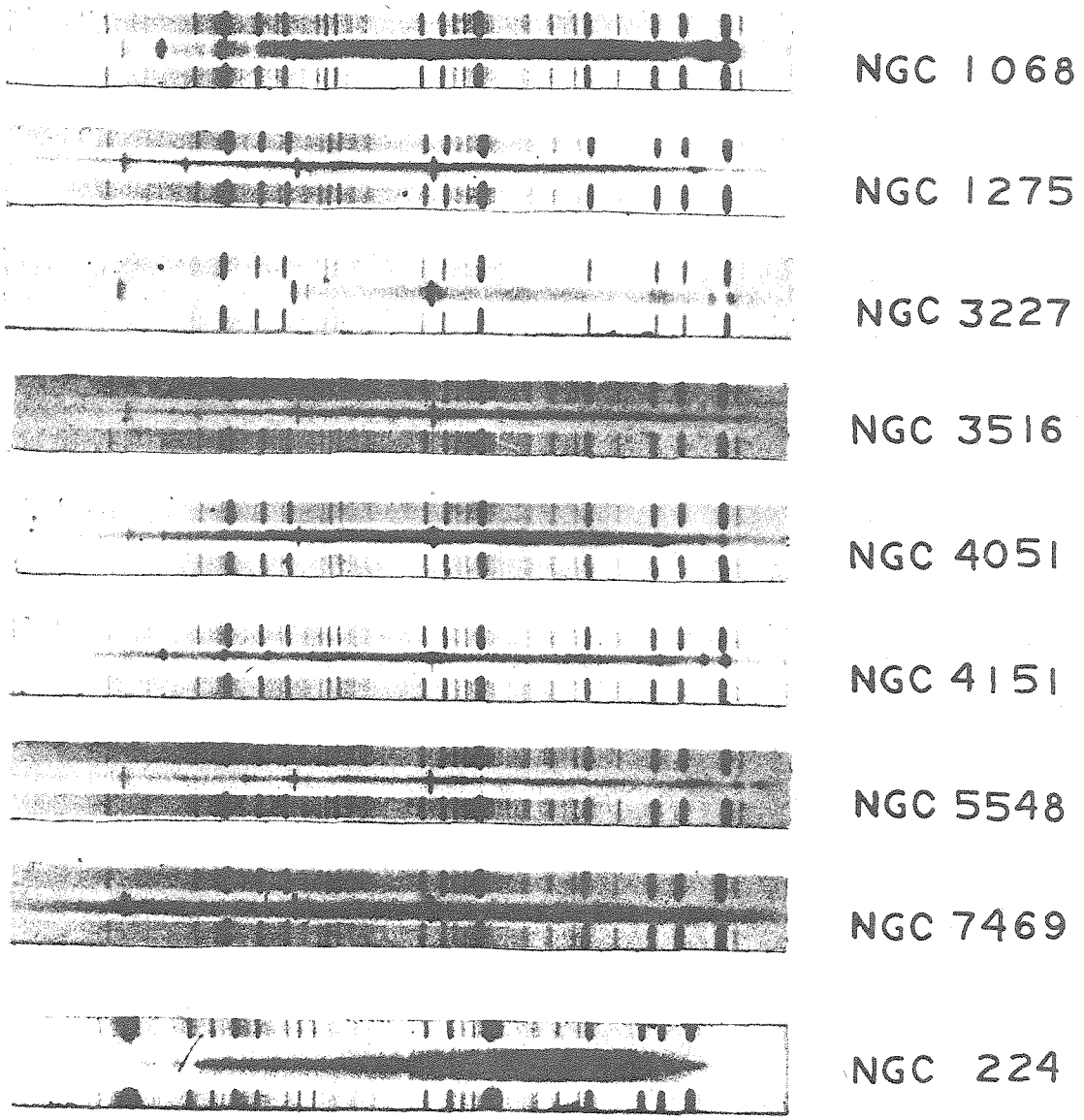

Figure 5: Spectra of the Seyfert nuclei from about λ3400 to λ5100. The original dispersion on IIa-O emulsion is approximately 180 Å/mm. For comparison purposes the nuclear spectrum of NGC 224 is also shown. The latter was obtained at somewhat lower dispersion.

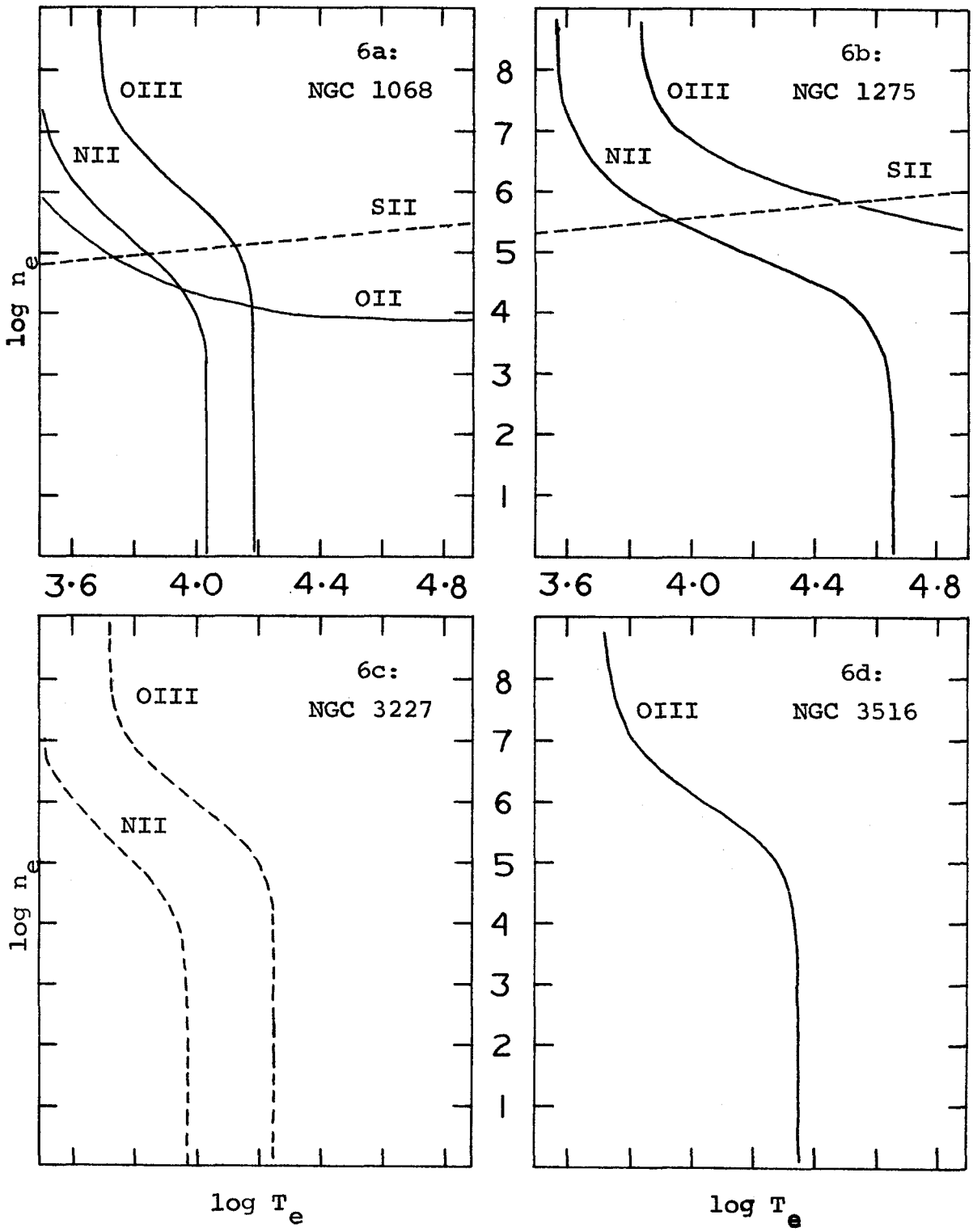

Figures 6a-6d: The $n_e(T_e)$ relations for: (a) NGC 1068, (b) NGC 1275, (c) NGC 3227, and (d) NGC 3516.

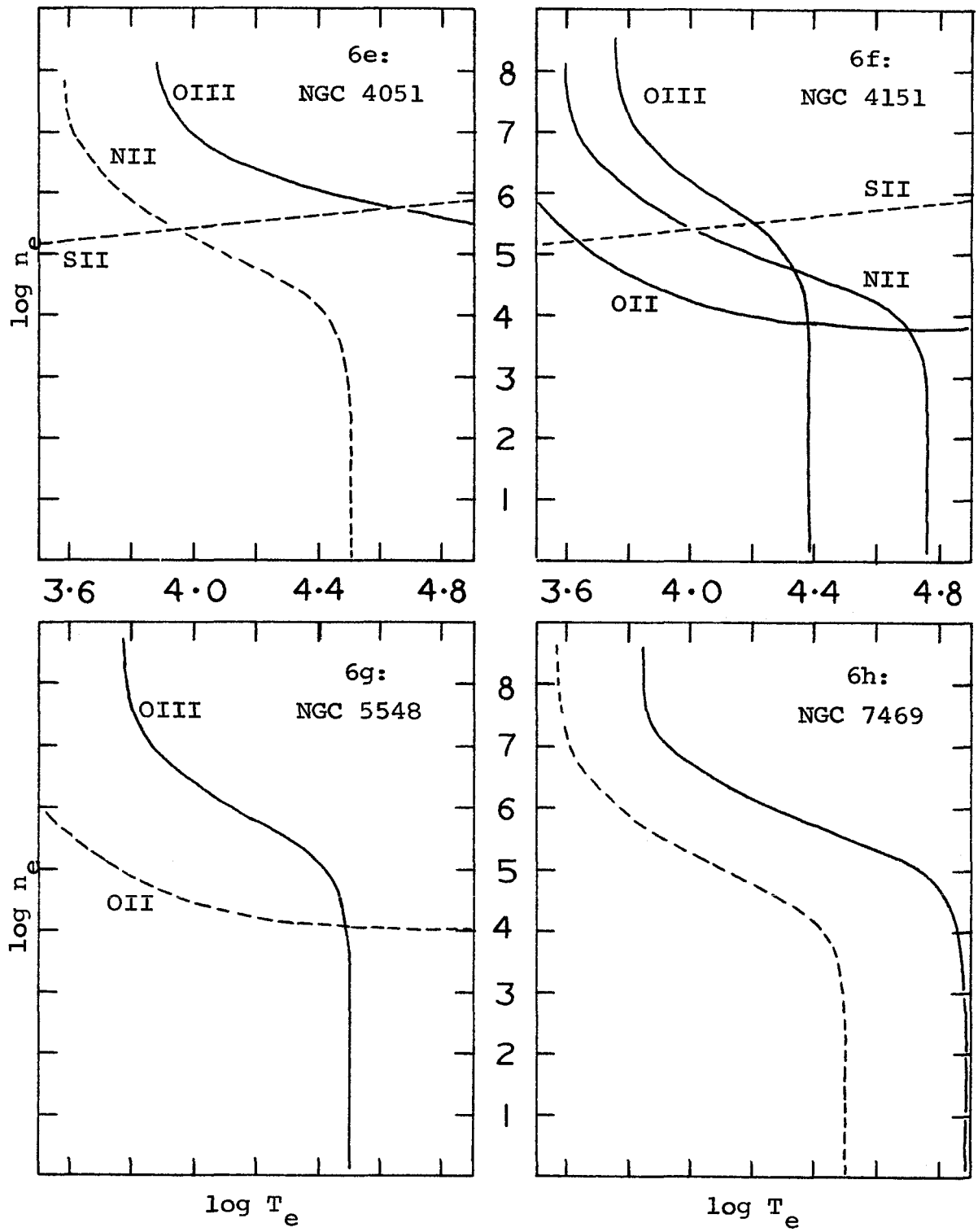

Figures 6e-6h: The $n_e(T_e)$ relations for: (e) NGC 4051, (f) NGC 4151, (g) NGC 5548, and (h) NGC 7469.

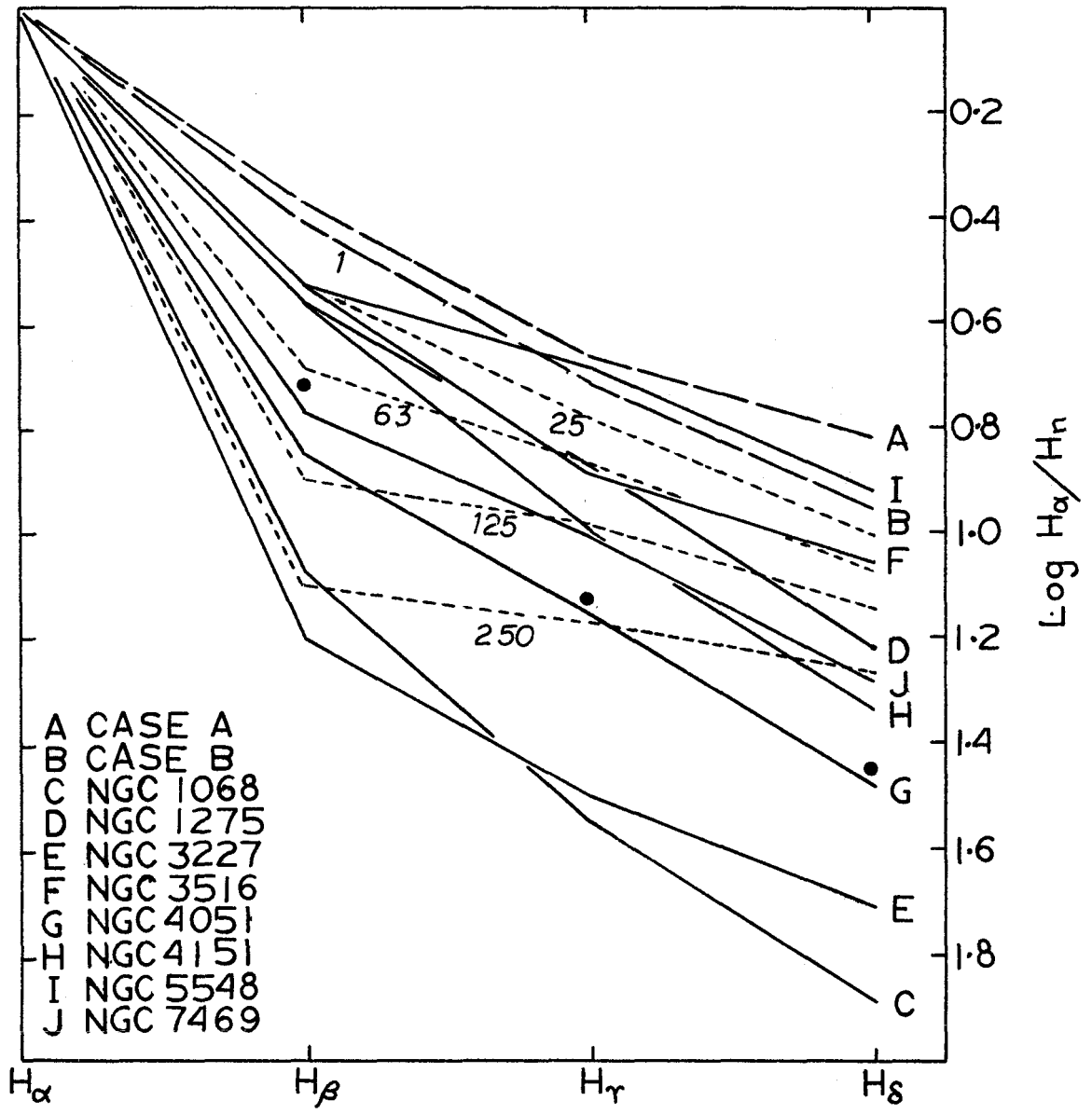

Figure 7: The reddening-corrected Balmer decrements for the Seyfert nuclei (solid lines). The dashed lines are the self-absorption decrements calculated by Capriotti (1964) for R = 0, T_e = 20,000 ^{o}K, and are paramaterized by τ_α. The filled circles are the T_e = 20,000 ^{o}K decrements calculated by Parker (1964). The self-absorption decrements for τ_α = 1 essentially coincide with the Case B values for the same temperature.

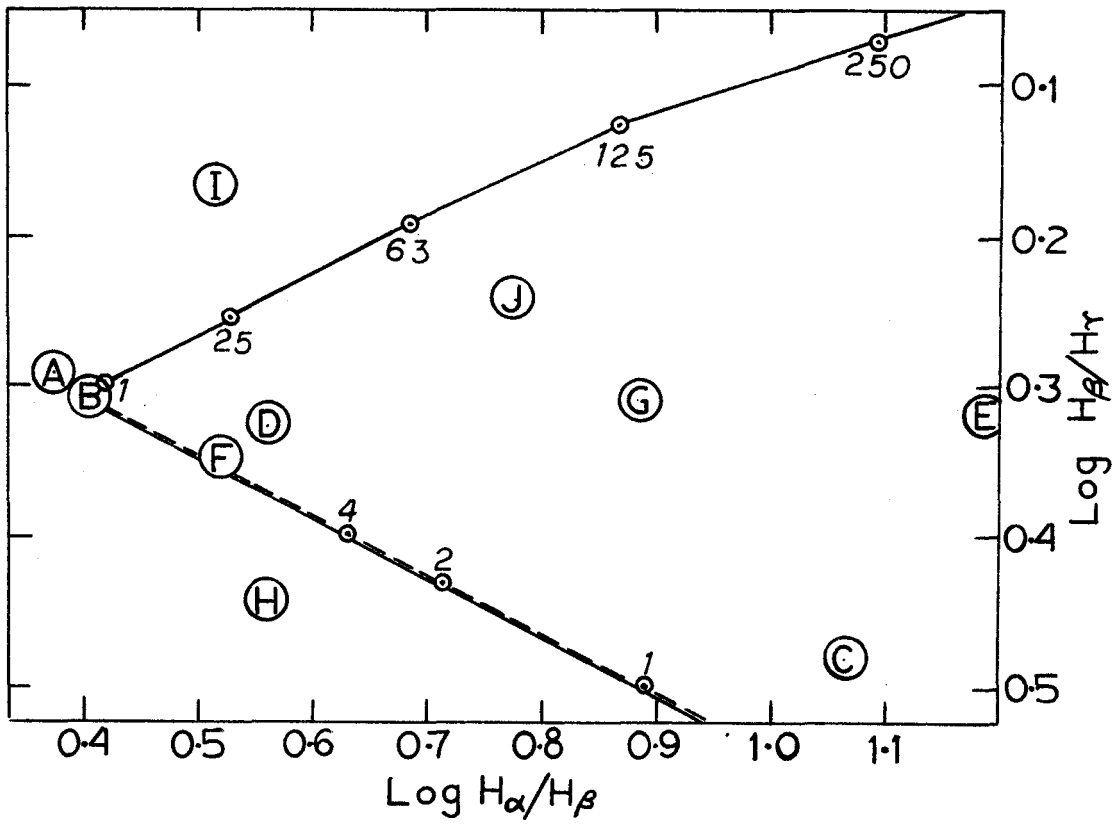

Figure 8: The H_β/H_γ - H_α/H_β relation for the Seyfert nuclei. The individual objects are identified as in figure 7. The upper (solid) curve is the self-absorption relation from figure 7 and is again parameterized by τ_α. The dashed curve represents the collisional values and is parameterized by $t = 10^{-4}T_e$. The reddening line is the solid curve parallelling the collisional curve.

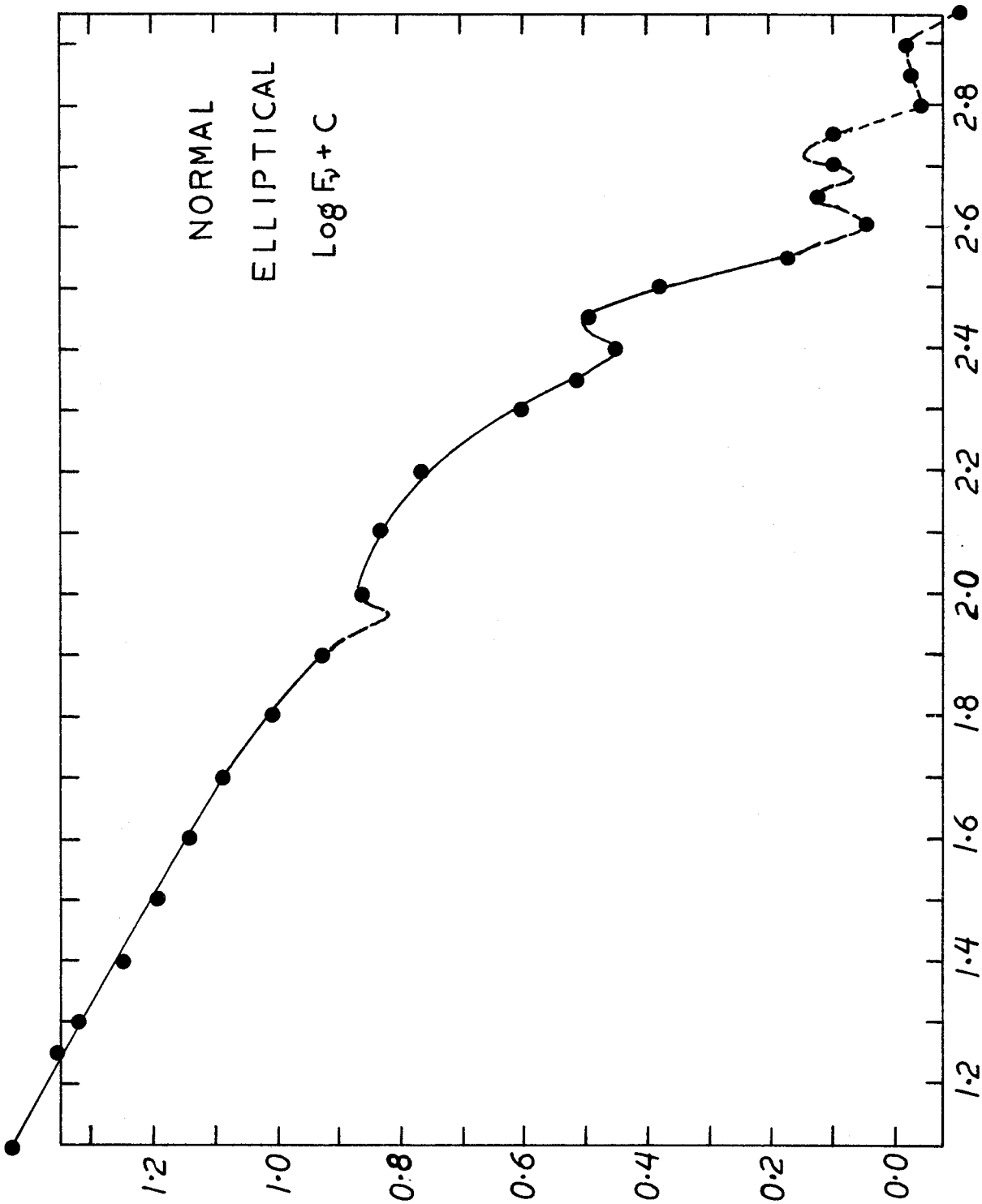

Figure 9: The reddening-corrected (csc b = 0) continuous energy distribution of the nucleus of a normal spiral. The zero-point of the log F_ν scale is arbitrary. (50Å bandpass)., cf. fig. 2.

Figures 10a-10h: The components of the continuous energy distributions of the Seyfert nuclei. The filled circles (●) are the observed fluxes corrected for reddening. The observed continuum is approximately represented by the upper solid curve and the lower solid curve is the result of subtracting the emission line and continuous recombination components. Crosses (X) define the upper limit for the contribution of the normal stellar distribution and the open circles (o) indicate the corresponding lower limit obtained for the non-thermal component. In most instances the continuous recombination flux distribution is not shown. In the figures for NGC 4151, NGC 5548, and NGC 7469, this contribution is shown as a dot-and-dash curve. In the notation of V-C :

● $f_o(\mu)$

----X $S(\mu)$

o $n(\mu)$

—·—·— $r(\mu)$

The units of the log F_ν scale are $erg/cm^2 sec$ (c/s).

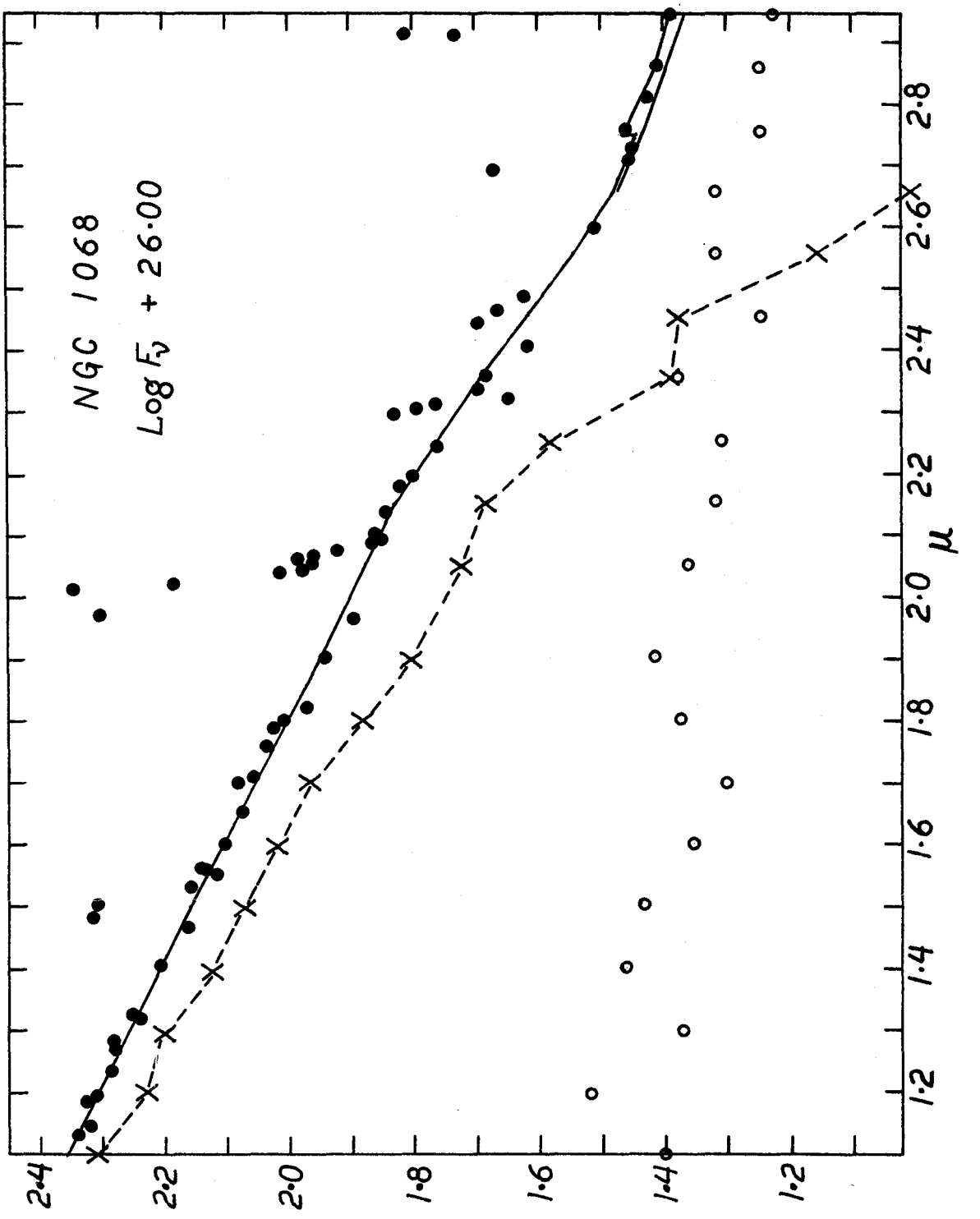

Table 10a: The components of the continuous energy distribution of NGC 1068.

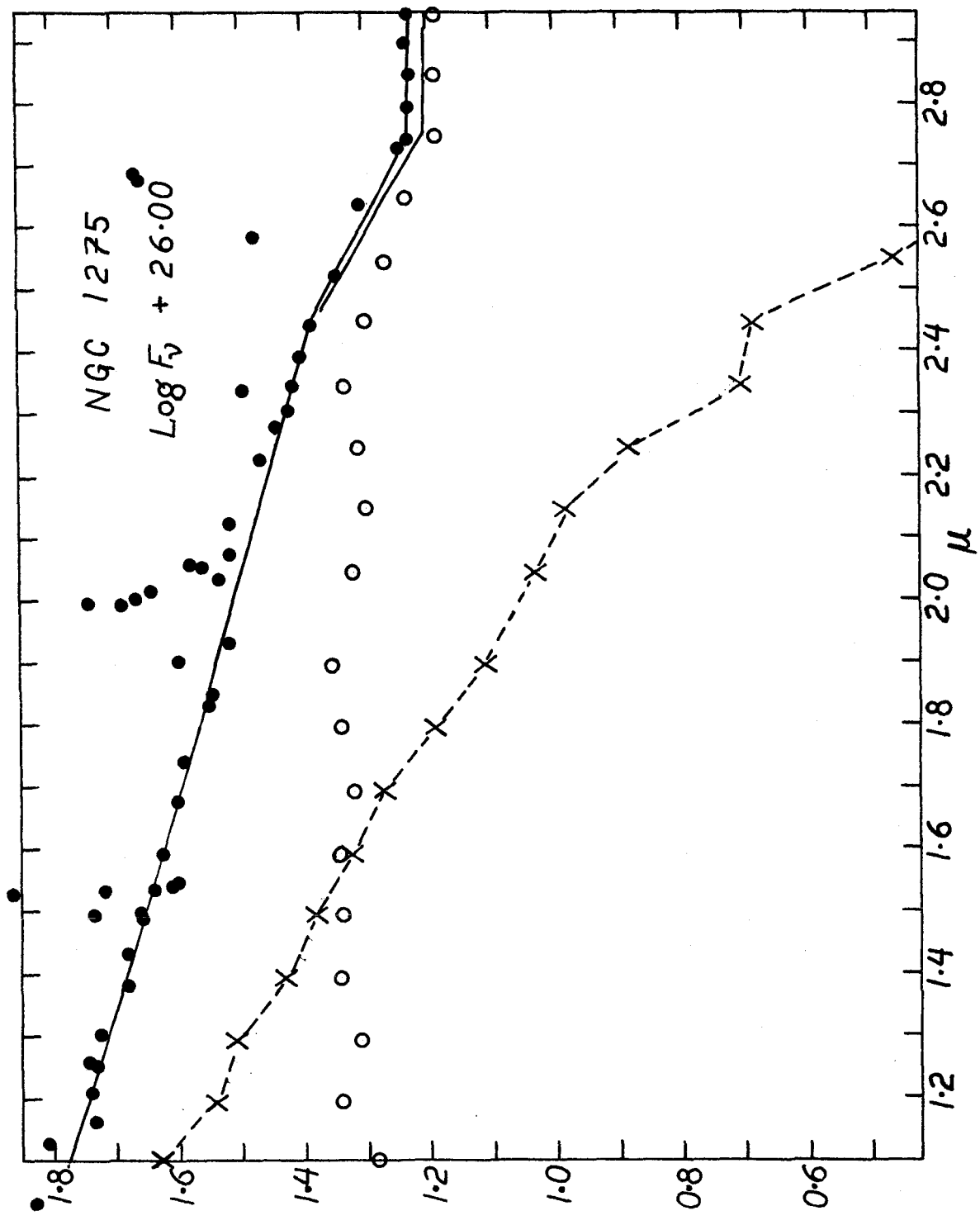

Table 10b: The components of the continuous energy distribution of NGC 1275.

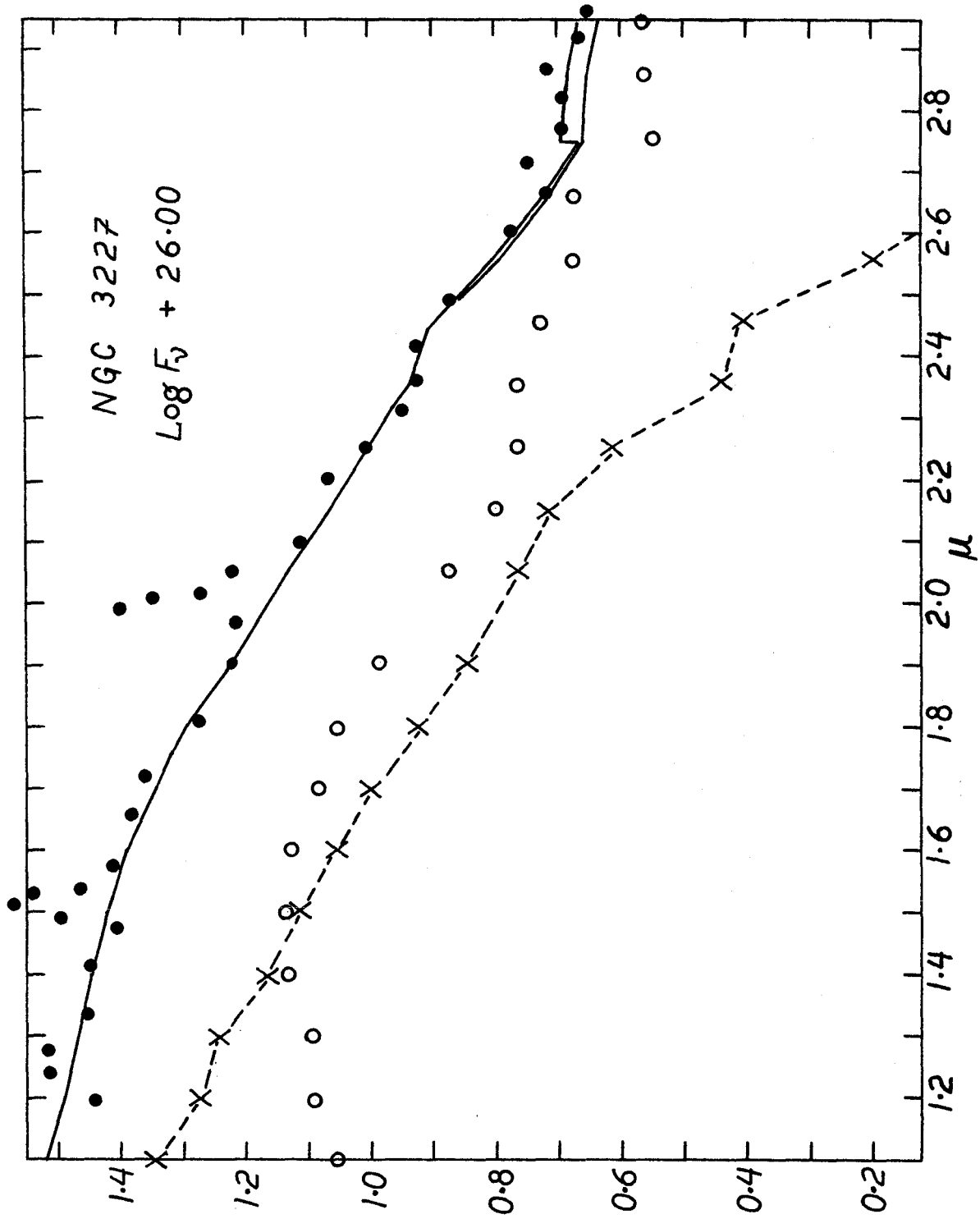

Table 10c: The components of the continuous energy distribution of NGC 3227.

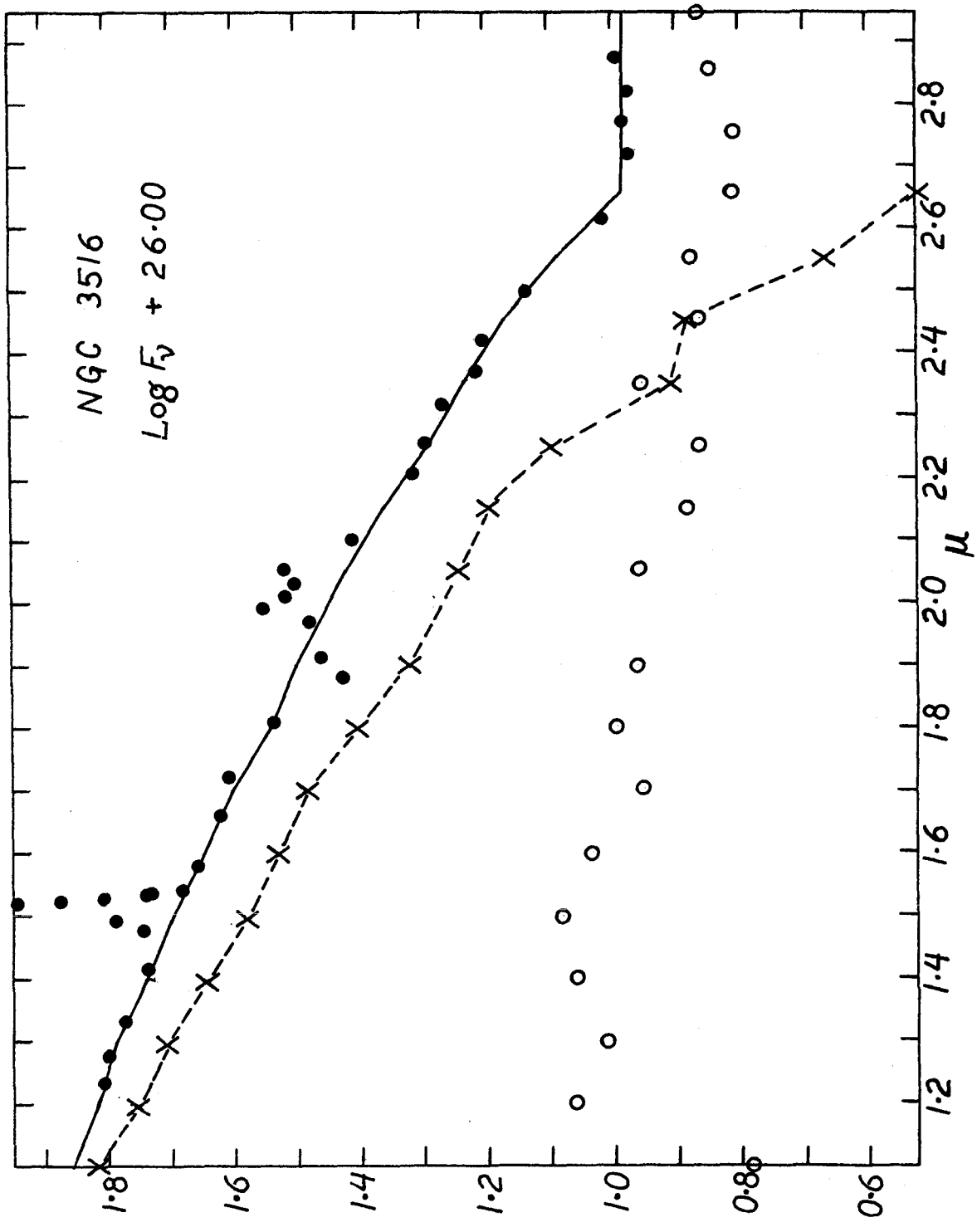

Table 10d: The components of the continuous energy distribution of NGC 3516.

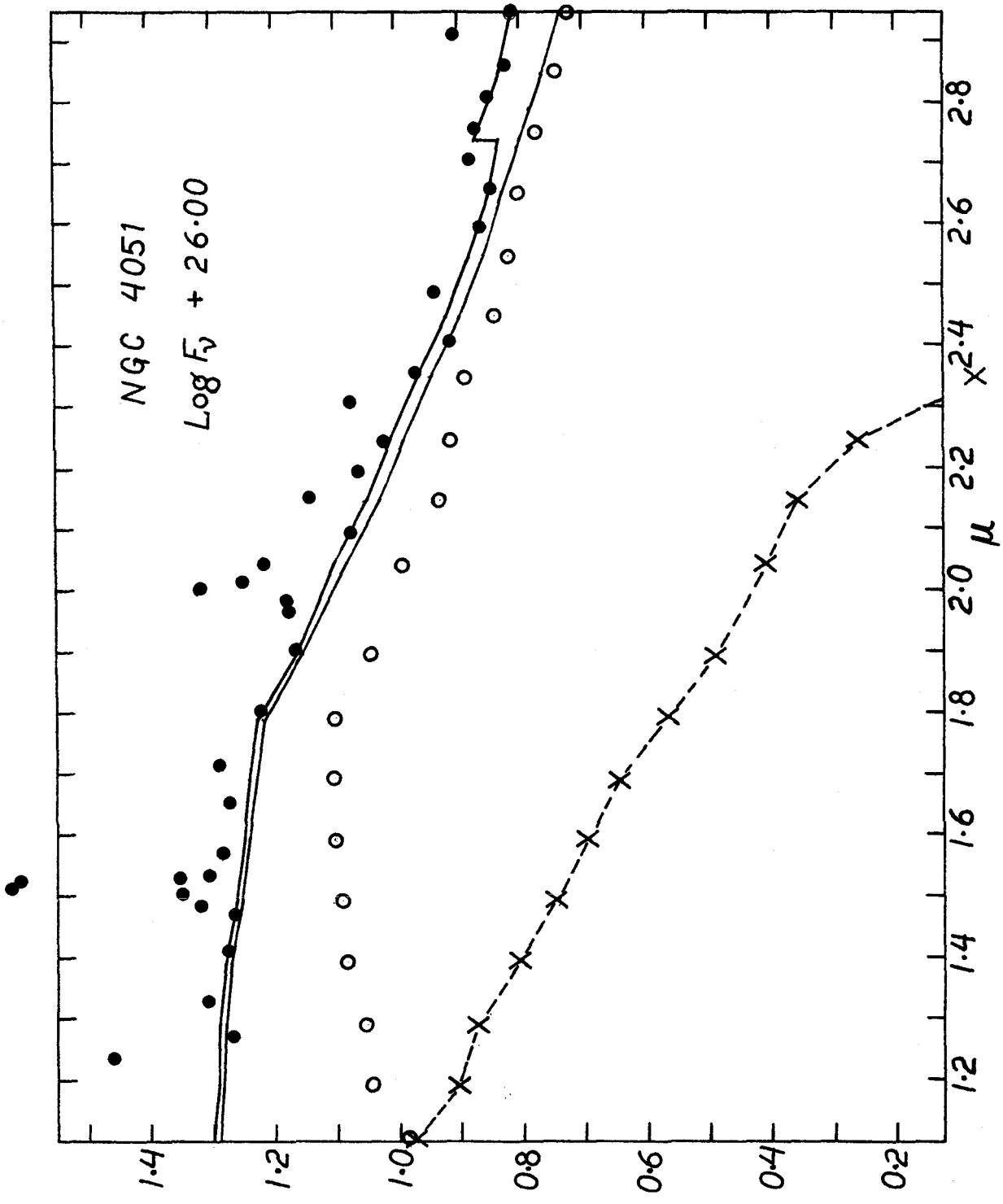

Table 10e: The components of the continuous energy distribution of NGC 4051.

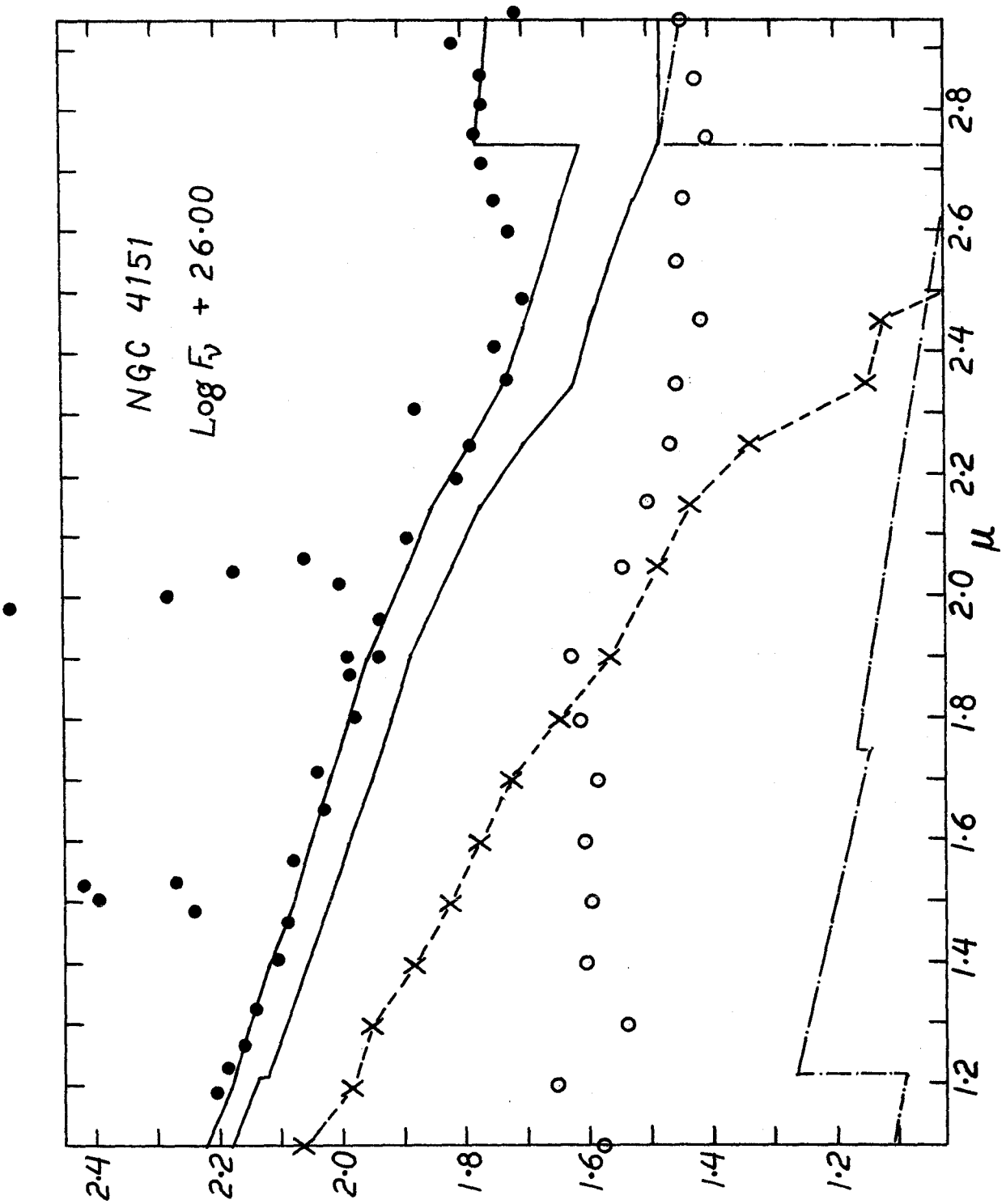

Table 10f: The components of the continuous energy distribution of NGC 4151.

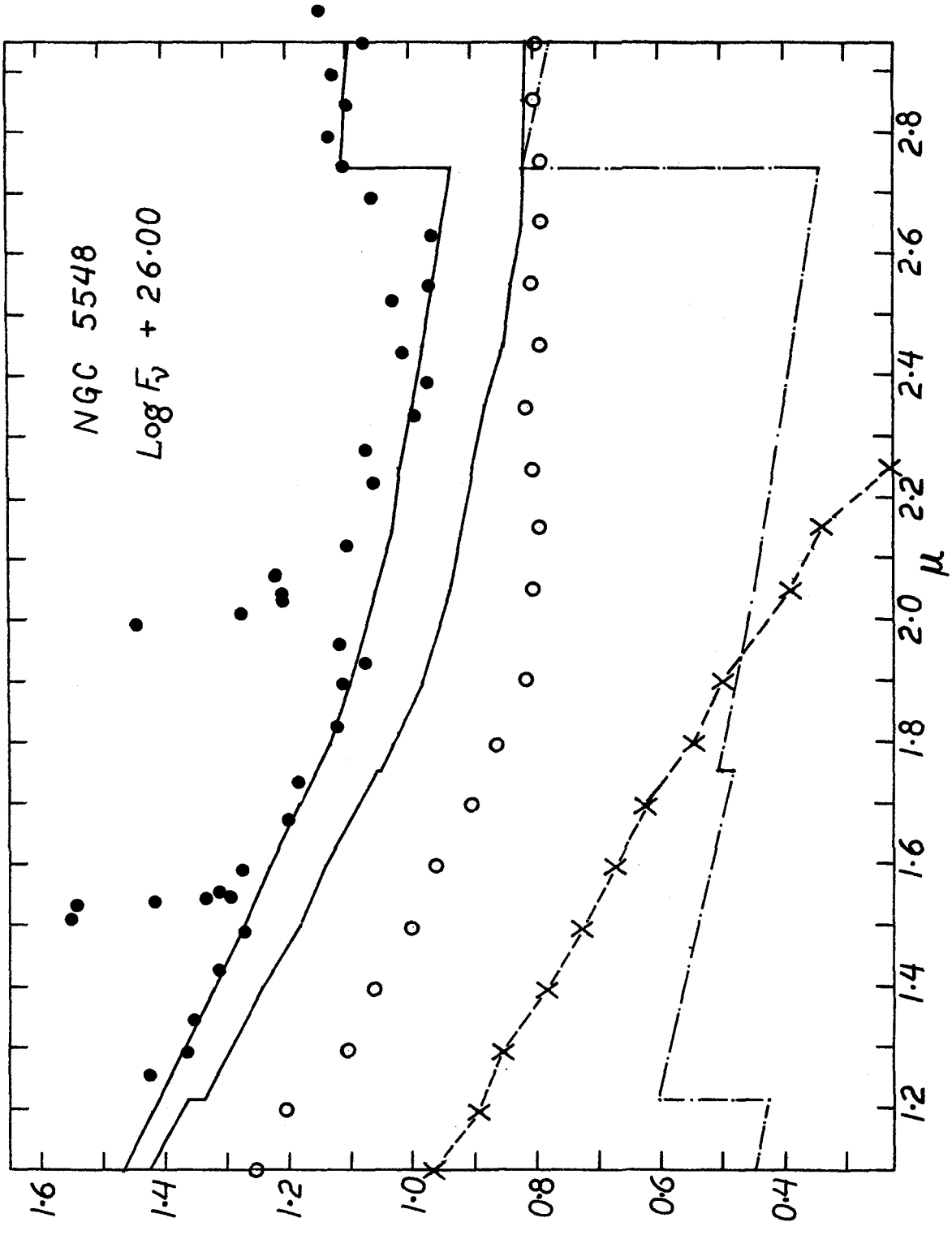

Table 10g: The components of the continuous energy distribution of NGC 5548.

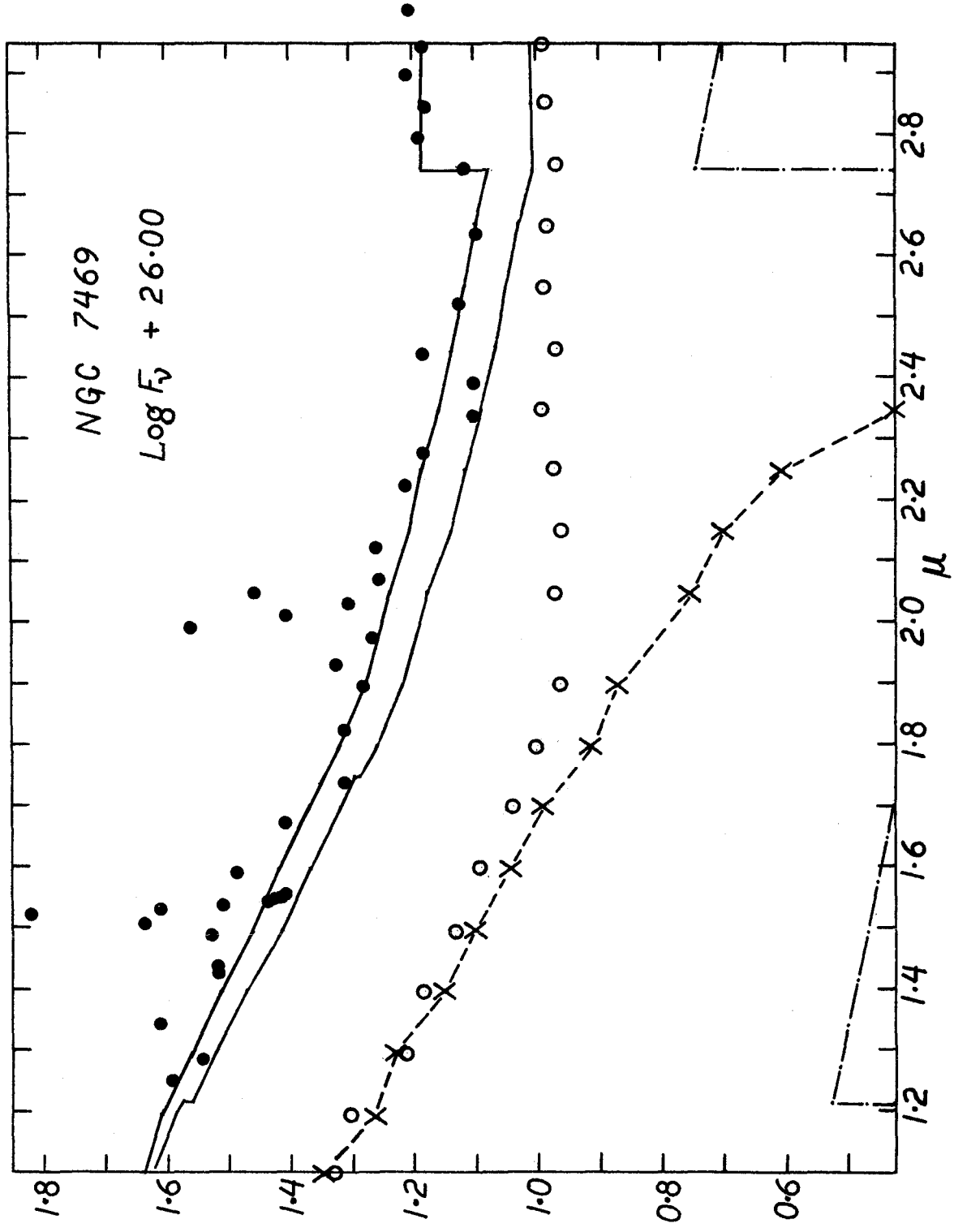

Table 10h: The components of the continuous energy distribution of NGC 7469.